

École doctorale n° 364 : Sciences Fondamentales et Appliquées

## Doctorat ParisTech

### THÈSE

pour obtenir le grade de docteur délivré par

**l'École Nationale Supérieure des Mines de Paris**

**Spécialité doctorale “Science et Génie des Matériaux”**

*présentée et soutenue publiquement par*

**Ali SAAD**

le 09 février 2016

## NUMERICAL MODELLING OF MACROSEGREGATION FORMED DURING SOLIDIFICATION WITH SHRINKAGE USING A LEVEL SET APPROACH

Co-directeur de thèse: **Charles-André GANDIN**

Co-directeur de thèse: **Michel BELLET**

### Jury

<b>Pr. Hervé COMBEAU,</b>	Professeur, Ecole des Mines de Nancy, France	
<b>Pr. Markus RETTENMAYR,</b>	Professeur, Université de Jena, Allemagne	
<b>Pr. Florian KARGL,</b>	Professeur, Agence Spatiale Allemande (DLR), Allemagne	
<b>Dr. Charles-André GANDIN,</b>	Directeur de recherche, CNRS, France	Examinateur
<b>Pr. Michel BELLET,</b>	Professeur MINES ParisTech, France	Examinateur
<b>Dr. Frédéric COSTES,</b>	Chef de service <i>THERCAST®</i> , TRANSVALOR S.A., France	Invité

T  
H  
E  
S  
S

MINES ParisTech

Centre de Mise en Forme des Matériaux (CEMEF)

UMR CNRS 7635, F-06904 Sophia Antipolis, France



---

## **Acknowledgement**

Dedicated to humanity ...



# Contents

<b>1 General Introduction</b>	<b>1</b>
1.1 Solidification notions . . . . .	2
1.1.1 Solute partitioning . . . . .	2
1.1.2 Dendritic growth . . . . .	4
1.1.3 Mush permeability . . . . .	6
1.2 Macrosegregation . . . . .	7
1.2.1 Liquid thermosolutal convection . . . . .	8
1.2.2 Solidification shrinkage . . . . .	9
1.2.3 Movement of equiaxed grains . . . . .	9
1.2.4 Solid deformation . . . . .	9
1.3 Other defects . . . . .	9
1.4 Industrial Worries . . . . .	11
1.5 Project context and objectives . . . . .	12
1.5.1 Context . . . . .	12
1.5.2 Objectives and outline . . . . .	14
<b>2 Modelling Review</b>	<b>19</b>
2.1 Modelling macrosegregation . . . . .	20
2.1.1 Macroscopic solidification model: monodomain . . . . .	22
2.2 Eulerian and Lagrangian motion description . . . . .	28
2.2.1 Overview . . . . .	28
2.2.2 Interface capturing . . . . .	30
2.3 Solidification models with level set . . . . .	30
2.4 The level set method . . . . .	31
2.4.1 Diffuse interface . . . . .	31
2.4.2 Mixing Laws . . . . .	34
2.5 Interface motion . . . . .	36
2.5.1 Level set transport . . . . .	36

## Contents

---

2.5.2	Level set regularisation . . . . .	38
2.6	Mesh adaptation . . . . .	42
2.6.1	Metrics and anisotropy . . . . .	42
2.6.2	<i>Remesh2</i> : Interface remeshing . . . . .	43
2.6.3	<i>Remesh4</i> : Multi-criteria remeshing . . . . .	44
<b>3</b>	<b>Energy balance with thermodynamic tabulations</b>	<b>47</b>
3.1	State of the art . . . . .	48
3.2	Thermodynamic considerations . . . . .	49
3.2.1	Volume averaging . . . . .	49
3.2.2	The temperature-enthalpy relationship . . . . .	50
3.2.3	Tabulation of properties . . . . .	50
3.3	Numerical method . . . . .	52
3.3.1	Enthalpy-based approach . . . . .	56
3.3.2	Temperature-based approach . . . . .	56
3.3.3	Convergence . . . . .	57
3.4	Validation . . . . .	58
3.5	Application: multicomponent alloy solidification . . . . .	61
3.5.1	Tabulations . . . . .	63
3.5.2	Discussion . . . . .	65
3.6	Limitations . . . . .	70
<b>4</b>	<b>Macrosegregation with liquid metal motion</b>	<b>73</b>
4.1	Introduction . . . . .	75
4.2	Formulation stability . . . . .	75
4.2.1	Stable mixed finite elements . . . . .	76
4.2.2	Variational multiscale (VMS) . . . . .	76
4.3	Navier-Stokes solver . . . . .	77
4.3.1	Strong and weak formulations . . . . .	78
4.3.2	Stabilisation parameters . . . . .	81
4.3.3	Implementation . . . . .	82
4.4	Application to multicomponent alloys . . . . .	83
4.4.1	<i>Tsolver</i> validation with fluid flow . . . . .	83
4.4.2	Results . . . . .	86
4.5	Macroscopic prediction of channel segregates . . . . .	92
4.5.1	Introduction . . . . .	92
4.5.2	Experimental work . . . . .	93
4.5.3	Macroscopic scale simulations . . . . .	93

4.6	Meso-Macro prediction of channel segregates . . . . .	103
4.6.1	Numerical method . . . . .	103
4.6.2	Configuration . . . . .	104
4.6.3	Effect of vertical temperature gradient . . . . .	108
4.6.4	Effect of cooling rate . . . . .	110
4.6.5	Effect of lateral temperature gradient . . . . .	112
4.6.6	Mono-grain freckles . . . . .	113
<b>5</b>	<b>Macrosegregation with solidification shrinkage</b>	<b>117</b>
5.1	Solidification shrinkage . . . . .	119
5.2	Choice of boundary tracking . . . . .	119
5.3	Multidomain formalism . . . . .	121
5.3.1	Assumptions . . . . .	122
5.3.2	Metal-Air boundary definition . . . . .	124
5.4	FE partitioned model . . . . .	125
5.4.1	In the metal . . . . .	126
5.4.2	In the air . . . . .	130
5.5	FE monolithic model . . . . .	131
5.5.1	Mass and momentum conservation . . . . .	131
5.5.2	Energy conservation . . . . .	134
5.5.3	Species conservation . . . . .	135
5.6	1D application: solidification with inverse segregation . . . . .	136
5.6.1	Geometry and boundary conditions . . . . .	136
5.6.2	Shrinkage without macrosegregation . . . . .	137
5.6.3	Shrinkage with macrosegregation . . . . .	145
5.7	2D application: controlled solidification benchmark . . . . .	157
5.7.1	Boundary condition effect . . . . .	157
5.7.2	Computational configuration . . . . .	159
5.7.3	Results . . . . .	160
5.8	3D application: reduced-gravity solidification . . . . .	165
5.8.1	Previous work . . . . .	165
5.8.2	Computational configuration . . . . .	168
5.8.3	Texus binary alloy . . . . .	175
5.8.4	Texus ternary and quaternary alloys . . . . .	181
<b>Conclusion and Perspectives</b>		<b>191</b>
<b>Bibliography</b>		<b>193</b>

## **Contents**

---

## List of Acronyms

Acronym	Standing for
ALE	Arbitrary Lagrangian-Eulerian
BTR	Brittle temperature range
CAFD	Cellular Automata Finite Difference
CAFE	Cellular Automata Finite Element
CBB	Circumventing Babuška-Brezzi
CCEMLCC	Chill Cooling for the Electro-Magnetic Levitator in relation with Continuous Casting of steel
CEMEF	Centre de Mise en Forme des Matériaux
CFL	Courant–Friedrichs–Lewy
C.FL.	Computing and FLuids
CSF	Continuum Surface Force
DLR	Deutsches Zentrum für Luft- und Raumfahrt
DSPG	Darcy-Stabilising/Petrov-Galerkin
EML	Electromagnetic levitation
ESA	European Space Agency
FEM	Finite Element Method
FVM	Finite Volume Method
GMAW	Gas Metal Arc Welding
ISS	International Space Station
IWT	Institut für Werkstofftechnik
LHS	Left-hand side
LSIC	Least squares on incompressibility constraint
LSM	Level set method
MAC	Marker-and-cell
PF	Phase field
PSPG	Pressure-Stabilising/Petrov-Galerkin
RHS	Right-hand side
RF	Radiofrequency
RUB	Ruhr Universität Bochum
RVE	Representative Elementary Volume
SBB	Satisfying Babuška-Brezzi
SUPG	Streamline-Upwind/Petrov-Galerkin
VMS	Variational MultiScale
VOF	Volume Of Fluid

## **Contents**

---

## **Contents**

---

# Chapter 5

## Macrosegregation with solidification shrinkage

### Contents

---

<b>5.1</b>	<b>Solidification shrinkage</b>	<b>119</b>
<b>5.2</b>	<b>Choice of boundary tracking</b>	<b>119</b>
<b>5.3</b>	<b>Multidomain formalism</b>	<b>121</b>
5.3.1	Assumptions	122
5.3.2	Metal-Air boundary definition	124
<b>5.4</b>	<b>FE partitioned model</b>	<b>125</b>
5.4.1	In the metal	126
5.4.2	In the air	130
<b>5.5</b>	<b>FE monolithic model</b>	<b>131</b>
5.5.1	Mass and momentum conservation	131
5.5.2	Energy conservation	134
5.5.3	Species conservation	135
<b>5.6</b>	<b>1D application: solidification with inverse segregation</b>	<b>136</b>
5.6.1	Geometry and boundary conditions	136
5.6.2	Shrinkage without macrosegregation	137
5.6.3	Shrinkage with macrosegregation	145
<b>5.7</b>	<b>2D application: controlled solidification benchmark</b>	<b>157</b>
5.7.1	Boundary condition effect	157
5.7.2	Computational configuration	159
5.7.3	Results	160
<b>5.8</b>	<b>3D application: reduced-gravity solidification</b>	<b>165</b>

## **Chapter 5. Macrosegregation with solidification shrinkage**

---

5.8.1	Previous work . . . . .	165
5.8.2	Computational configuration . . . . .	168
5.8.3	Texus binary alloy . . . . .	175
5.8.4	Texus ternary and quaternary alloys . . . . .	181

---

## 5.1 Solidification shrinkage

Solidification shrinkage is, by definition, the effect of relative density change between the liquid and solid phases. In general, it results in a progressive volume change during solidification, until the phase change has finished. The four stages in [figs. 5.1a](#) to [5.1d](#) depict the volume change with respect to solidification time. First, at the level of the first solid crust, near the local solidus temperature, the solid forms with a density greater than the liquid. The subsequent volume decrease forces the fluid to be sucked in the direction of the volume change (cf. [fig. 5.1b](#)). When this sucking becomes impossible due to a low permeability of the mush, voids may appear. As a direct result of the inward feeding flow, the ingot free surface with the air tends to gradually deform to follow the feeding direction, forming the so-called *shrinkage pipe*, shown in [fig. 5.2](#). Since the mass of the alloy and its chemical species is conserved, a density difference between the phases ( $\langle \rho \rangle^l < \langle \rho \rangle^s \implies \frac{\langle \rho \rangle^l}{\langle \rho \rangle^s} < 1$ ) eventually leads to a different overall volume ( $V^s < V^l$ ) once solidification is complete, as confirm the following mass conservation equations, from initial (LHS term) to final (RHS term) state:

$$\langle \rho \rangle^l V^l = \langle \rho \rangle^s V^s \quad (5.1a)$$

$$V^s = \frac{\langle \rho \rangle^l}{\langle \rho \rangle^s} V^l \quad (5.1b)$$

Solidification shrinkage is not the only factor responsible for volume decrease. Shrinkage due to temperature and composition variations in both solid and liquid phases, are also common causes in a casting process. Thermal shrinkage is very important to apprehend in steel casting, as the temperature decrease usually exceeds a 1000 °C between the solidus and ambient temperature. This causes substantial density variations.

## 5.2 Choice of boundary tracking

In chapter 2, several methods of boundary tracking/capturing methods were presented along with their similarities and differences. In the case of solidification shrinkage, the metal-air boundary can be tracked with any method from the previously mentioned. However, several reasons motivate us to settle on the level set method. First, the easiest solution is testing a method which already exists in the *CimLib* library. The level set method was implemented as a framework for monolithic resolution. Since this work, the method has been extensively used and improved in several projects

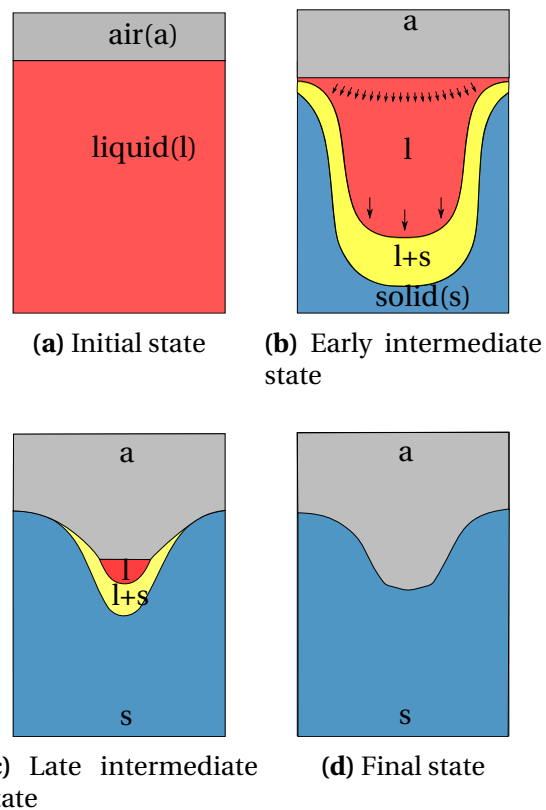


**Fig. 5.1** – Schematic of the main cooling stages of an ingot against side and bottom mould walls (not shown)

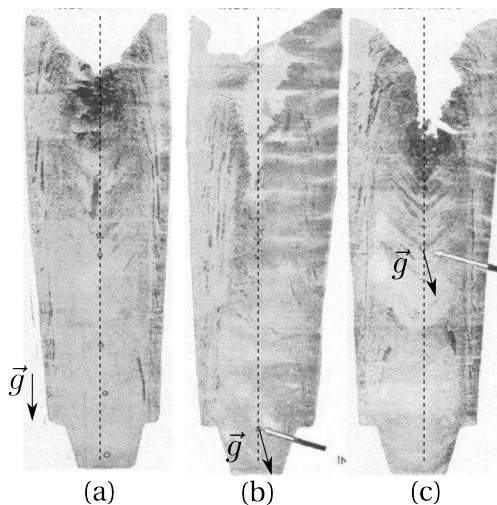


**Fig. 5.2** – Sulphur prints of three low-carbon steel ingots showing pipe formation at the top as a result of solidification shrinkage, marked with dark areas corresponding to higher sulphur content, while varying ingot inclination during casting. Ingot orientation changes from (a) vertical position to (b)  $25^\circ$ -inclination after 34 minutes of vertical (dashed line) casting and finally (c)  $25^\circ$ -inclination after 3 hours of vertical casting. The white arrow indicates the inclination onset [Onodera and Arakida 1959]. The black arrow indicates the gravity direction.

mainly for multiphase flows, which is the main competence of the Computing and FLuids (C.FL.) group at CEMEF. Another motivation is the compatibility between *Cim-Lib* and *THERCAST*<sup>®</sup>, where the latter is the final destination of the code developed during this Ph.D. thesis. In its recent versions, *THERCAST*<sup>®</sup> handles laminar and turbulent ingot filling where the level set method is used to capture the free surface of the molten metal. Aside from the practical motivations, some technical aspects of the level set method make it very attractive to address macroscopic surface tracking (in contrast to microscopic interface tracking, for instance the solid-liquid interface), such as topological properties that are readily available (e.g. curvature) and accurate position compared to volume-based methods like VOF [Sethian 1999].

## 5.3 Multidomain formalism

In the previous chapters, we considered in our simulations the metallic alloy as a saturated mixture of solid and liquid during solidification. It means that no gas phase was supposed to appear during the process. Additionally, we ignored shrinkage and expansion effects. These considerations resulted in a fixed interface between the free surface of the liquid metal and the surrounding air. As a consequence, air was not considered in the model. The reason is that we chose to describe our model in Eulerian description, for which we have considered a fixed grid to discretise the averaged conservation equations governing the phase change between the liquid and solid phases. With the introduction of shrinkage, an increase in global density of the metallic alloy means that a gas phase should enter the domain to replace the shrunk volume.

At this point, several interfaces may be distinguished: liquid-solid (*l-s*), liquid-air (*l-a*) and solid-air (*s-a*), where we defined 2 phases (*l* and *s*) belonging to the "Metal" domain denoted *M*, while the "Air" domain, denoted *A*, is made up of a unique gas phase, (*a*), with the same name. As a standard for this formalism, we consider that upper case letters are used for domains, while lower case letters are used for phases.

The main idea behind the multidomain formalism is to go from the classic conservations equations introduced by volume averaging in chapter 2 in the context of a solidifying two-phase system to generalise it by taking into account a third gas phase, such as:

$$V^l + V^s + V^a = V_E \quad (5.2)$$

$$g^l + g^s + g^a = 1 \quad (5.3)$$

where  $g^\phi$  is the volume fraction of each phase  $\phi = [l, s, a]$ . Then, one is free to choose a suitable numerical method to define and track the physical interfaces between the several phases. In our macroscale applications, we are particularly interested in keeping an indirect representation of the  $l-s$  interface (dotted line in fig. 5.3) using the volume averaging theory, while employing a different method to track the metal-air ( $M-A$ ) boundary ( $l-a$  and  $s-a$  interfaces, represented by dashed lines in fig. 5.3) with the level set method. This allows switching to the latter method in a physically representative manner.

In this context, each domain can be seen as a material having a physical interface with the other domains. As a consequence of our interpretation, the gas phase should not exist in the metal, which may naturally occur if the thermodynamic conditions are in favour of nucleating and growing a new phase, or in the case of a gas that was trapped inside mould grooves.

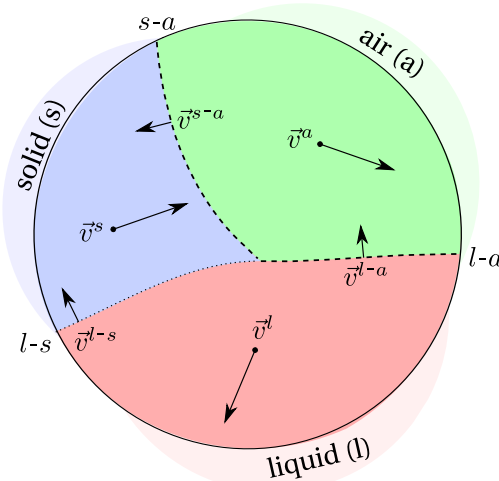


**Fig. 5.3** – Schematic of a representative volume element containing 3 phases with distinct velocities, separated by 3 interfaces. The dotted line is the indirectly tracked solid-liquid interface while the other dashed lines, air-liquid and air-solid interfaces, are directly tracked.

### 5.3.1 Assumptions

Each phase in the system has its own velocity,  $v^l$ ,  $v^s$  and  $v^a$ , while the respective interfaces  $l-s$ ,  $l-a$  and  $s-a$  have different and independent velocities, represented by  $v^{l-s}$ ,  $v^{l-a}$  and  $v^{s-a}$ . Note that the solid-liquid interface velocity was denoted  $v^*$  in the previous chapters as no more than two phases were considered.

The first major assumption is that the solid phase, once formed from the liquid, is fixed and rigid, hence  $v^s = 0$ . It means that no subsequent deformation or contraction/expansion of the solid phase ( $\langle \rho \rangle^s = \text{constant}$ ) may occur and therefore  $v^{s-a}$

reduces to vector zero. Moreover, we use the already introduced volume averaging principles to write locally for any quantity  $\psi$ :

$$\langle \psi \rangle = \left\langle \psi^l \right\rangle \langle \psi^s \rangle + \langle \psi^a \rangle \quad (5.4a)$$

$$= g^l \psi^l + g^s \psi^s + g^a \psi^a \quad (5.4b)$$

where volume fractions,  $g^\phi$ , for each phase  $\phi$  were used. Rappaz et al. [2003] define the volume fraction by writing a general expression inside the representative volume  $V_E$ :

$$g^\phi = \frac{1}{V_E} \int_{V_E} \chi^\phi(x, t) d\Omega = \left\langle \chi^\phi \right\rangle \quad (5.5)$$

where the integrated quantity is an indicator (or presence) function relative to phase  $\phi$ , which defines the volume of this phase in the system,  $\Omega^\phi$ , as follows:

$$\chi^\phi(x, t) = \begin{cases} 1 & \text{if } x \in \Omega^\phi \\ 0 & \text{otherwise} \end{cases} \quad (5.6)$$

Any phenomenon that may displace an interface, whether by phase change or a phase motion, is mathematically translated by variations of the presence function, such that its total derivative for each phase satisfies the following:

$$\frac{d\chi^\phi}{dt} = \frac{\partial \chi^\phi}{\partial t} + \mathbf{v}^* \cdot \nabla \chi^\phi = 0 \quad (5.7)$$

If we consider the liquid phase for instance, the variations of any quantity  $\psi$  are given by:

$$\left\langle \frac{\partial \psi^l}{\partial t} \right\rangle = \frac{\partial \langle \psi^l \rangle}{\partial t} - \frac{1}{V_E} \int_{\Gamma_{l-a}} \psi^l \mathbf{v}^{l-a} \cdot \mathbf{n}^{l-a} dA - \frac{1}{V_E} \int_{\Gamma_{l-s}} \psi^l \mathbf{v}^{l-s} \cdot \mathbf{n}^{l-s} dA \quad (5.8)$$

$$\left\langle \nabla \psi^l \right\rangle = \nabla \left\langle \psi^l \right\rangle + \frac{1}{V_E} \int_{\Gamma_{l-a}} \psi^l \mathbf{n}^{l-a} dA + \frac{1}{V_E} \int_{\Gamma_{l-s}} \psi^l \mathbf{n}^{l-s} dA \quad (5.9)$$

$$\left\langle \nabla \cdot \psi^l \right\rangle = \nabla \cdot \left\langle \psi^l \right\rangle + \frac{1}{V_E} \int_{\Gamma_{l-a}} \psi^l \cdot \mathbf{n}^{l-a} dA + \frac{1}{V_E} \int_{\Gamma_{l-s}} \psi^l \cdot \mathbf{n}^{l-s} dA \quad (5.10)$$

So far, we know that eq. (5.7) allows transporting an interface between 2 phases, or a more generally a boundary between multiphase domains. We also know that eqs. (5.8) to (5.10) allow computing temporal and spatial variations of any physical quantity related to a phase or more generally a multiphase domain. To avoid ambiguity, we still have to establish a definition for the boundary between the metal and the air, i.e. which interfaces should be accounted for when considering the transport of the

metal-air boundary.

### 5.3.2 Metal-Air boundary definition

In reality, between the metal and the air, two boundaries exist, as explained by Niane [2004]. The liquid-air interface exists at early stages of solidification where only the free surface of the liquid is in contact with the air, as shows stage 1 in [fig. 5.4](#).

In later stages (transition from stage 2 to stage 3 in [fig. 5.4](#)), the mushy zone delimited by dendrite tips, reaches the free liquid surface, creating hence two distinct boundaries: a first boundary separating interdendritic liquid from the air, and a second boundary that separates the dendrite tips from the air. In other words, a porous medium made up of solid+air settles between the mushy zone (solid+liquid) and the air domain. The lower part of the this porous medium is defined by the *l-a* interface and is driven by solidification shrinkage. Therefore, its real microscopic velocity is equal to the interdendritic liquid velocity,  $v^l$ . According to Dantzig and Rappaz [2009], this velocity is constant when the solidification shrinkage and the isotherms velocity  $v_T$  are constant, as states the equation:

$$v^l = -\beta_{SS} v_T \quad (5.11)$$

As for the upper part of porous medium, delimited by the *s-a* interface, its motion could be induced by a mechanical deformation of the solid phase either due to thermal shrinkage/expansion or external mechanical stresses. The first factor is ubiquitous in any solidification process, while the second factor is process-dependent.

In the present work, we remind that the solid phase is assumed fixed and rigid, therefore we consider dendrites to be undeformable during their growth. Unfortunately, this assumption is contradictory with our current situation where the metal keeps shrinking, until an overlap of the transition zone (intersection of both domains, identified by  $H^{tr}$ ) and the mushy zone takes place, as shown in [fig. 5.4](#) (second row, stage 3). At this point, both interfaces define the *M-A* boundary. Although it is necessary to track the *s-a* boundary also, the present work limited to considering the *l-a* interface as fully defining the metal-air boundary. Tracking the *s-a* interface adds complexity as an additional tracking method has to be used like a new level set with distinct numerical properties. This assumption will have some influence regarding the overall simulation performance, as some errors are induced, as the porous medium is not properly accounted for. Further discussions about the outcomes of our definition of the metal-air boundary are given in the 1D application section. With the previous definitions, [eq. \(5.7\)](#) can be recast with the level set method by using the smoothed

Heaviside function in the metal:

$$\frac{dH^M}{dt} = \frac{\partial H^M}{\partial t} + \mathbf{v}^{M-A} \cdot \nabla H^M = 0 \quad (5.12a)$$

$$\frac{dH^M}{dt} = \frac{\partial H^M}{\partial t} + \mathbf{v}^{l-a} \cdot \nabla H^M = 0 \quad (5.12b)$$

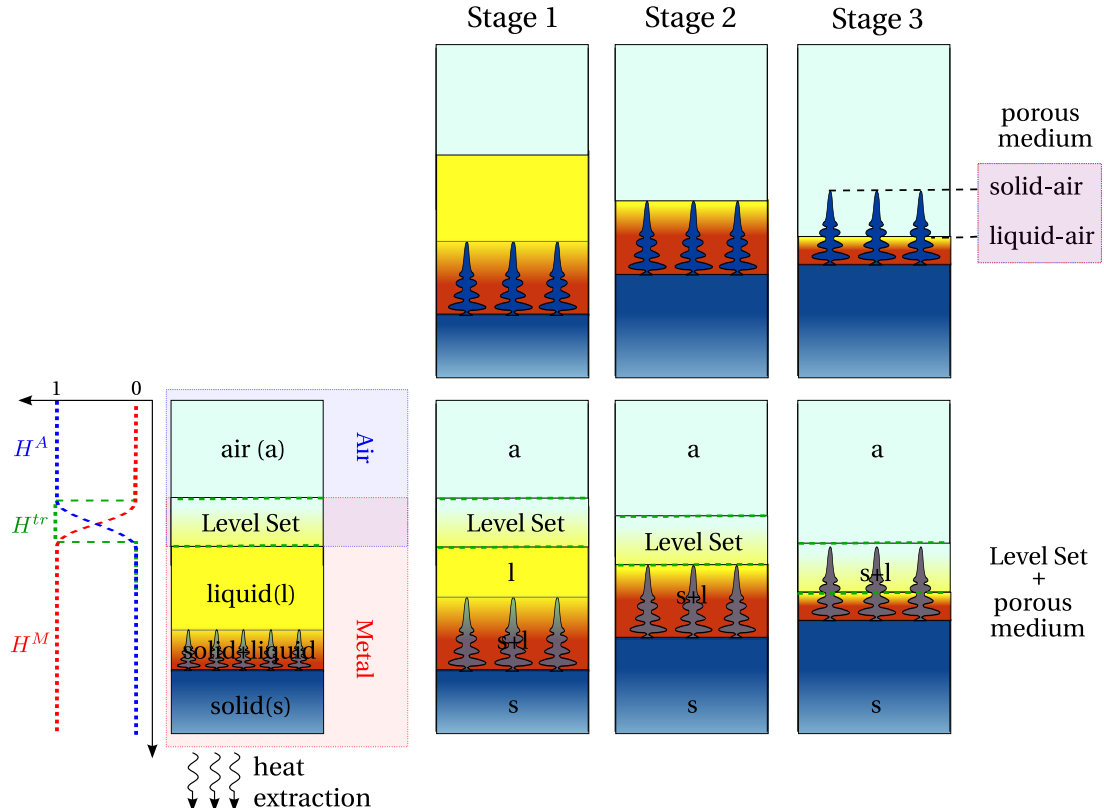


**Fig. 5.4** – Schematic describing (first row) the physical solidification process and (second row) its numerical treatment of moving the boundary between air and metal domains, at three intermediate stages of solidification.  $H^M$ ,  $H^A$  and  $H^{tr}$  are respectively the Heaviside functions for the metal, the air and the transition zone between both domains.

## 5.4 FE partitioned model

In this section, we start from the monodomain finite element model presented in [section 2.1.1](#) that was relevant to the metal only, referred to by the superscript  $M$ , then present the essential assumptions and formulations that allow predicting solidification shrinkage in a Eulerian context that introduces another domain, the air, referred to by the superscript  $A$ .

### 5.4.1 In the metal

#### Mass and momentum conservation

By assuming a fixed solid phase ( $v^s = 0$ ), i.e. a constant density for the solid phase without any transport of this phase, the average velocity in the metal reduces only to liquid's average velocity.

Therefore, we can write:

$$\langle \mathbf{v} \rangle^M = \langle \mathbf{v}^l \rangle + \langle \mathbf{v}^s \rangle = g^l \mathbf{v}^l + \cancel{g^s \mathbf{v}^s} \quad (5.13)$$

With [eq. \(5.13\)](#), the mass balance in the metal writes:

$$\frac{\partial \langle \rho \rangle^M}{\partial t} + \nabla \cdot (\rho \mathbf{v})^M = 0 \quad (5.14a)$$

$$\frac{\partial \langle \rho \rangle^M}{\partial t} + \nabla \cdot (g^l \langle \rho \rangle^l \mathbf{v}^l) = 0 \quad (5.14b)$$

$$\frac{\partial \langle \rho \rangle^M}{\partial t} + \langle \rho \rangle^l \nabla \cdot (g^l \mathbf{v}^l) + g^l \mathbf{v}^l \cdot \nabla \langle \rho \rangle^l = 0 \quad (5.14c)$$

$$\nabla \cdot \langle \mathbf{v}^l \rangle = -\frac{1}{\langle \rho \rangle^l} \left( \frac{\partial \langle \rho \rangle^M}{\partial t} + \langle \mathbf{v}^l \rangle \cdot \nabla \langle \rho \rangle^l \right) \quad (5.14d)$$

[Equation \(5.14d\)](#) explains the flow due to shrinkage. A negative divergence term means that a liquid feeding is necessary to compensate for a density increase upon solidification, where  $\langle \rho \rangle^s > \langle \rho \rangle^l$  in the transient term, hence acting as a flow driving force in the melt. The second RHS term accounts for the volume change due to heat and species variations in the liquid.

When the metal's density was considered constant during solidification, the assumption of an incompressible system made it possible to use the Boussinesq approximation. However, in the case of solidification shrinkage, the average density  $\langle \rho \rangle^M$  varies, as it depends on the solidification path as well as on  $\langle \rho \rangle^s$  and  $\langle \rho \rangle^l$  which are not equal nor constant.

Therefore, the incompressibility condition is no more applicable. In such case, the earlier given system [eq. \(2.44\)](#) is reformulated without any reference value for density

and assuming a fixed solid phase:

$$\left\{ \begin{array}{l} \langle \rho \rangle^l \left( \frac{\partial \langle \mathbf{v}^l \rangle}{\partial t} + \frac{1}{g^l} \nabla \cdot (\langle \mathbf{v}^l \rangle \times \langle \mathbf{v}^l \rangle) \right) = \\ - g^l \nabla p^l - 2\mu^l \nabla \cdot (\bar{\nabla} \langle \mathbf{v}^l \rangle + \bar{\nabla}^\top \langle \mathbf{v}^l \rangle) - g^l \mu^l \mathbb{K}^{-1} \langle \mathbf{v}^l \rangle + g^l \langle \rho \rangle^l \mathbf{g} \\ \nabla \cdot \langle \mathbf{v}^l \rangle = - \frac{1}{\langle \rho \rangle^l} \left( \frac{\partial \langle \rho \rangle^M}{\partial t} + \langle \mathbf{v}^l \rangle \cdot \nabla \langle \rho \rangle^l \right) \end{array} \right. \quad (5.15)$$

### Energy conservation

In the energy equation, a volumetric source term accounts for the heat dissipation caused by the shrinking metal volume. Before writing the new equation, we make the following assumptions:

- consequence of the static solid phase:  $\langle \rho h \mathbf{v} \rangle^M = g^l \langle \rho \rangle^l \langle h \rangle^l \mathbf{v}^l + \cancel{g^s \langle \rho \rangle^s \langle h \rangle^s \mathbf{v}^s}$ ,
- the heat generated by mechanical deformation,  $\mathbb{S} : \dot{\varepsilon}$ , is neglected.

The unknowns in the energy conservation are the average volumetric enthalpy  $\langle \rho h \rangle^M$  and temperature  $T$ . The energy conservation equation writes:

$$\frac{\partial \langle \rho h \rangle^M}{\partial t} + \nabla \cdot \langle \rho h \mathbf{v} \rangle^M = \nabla \cdot (\langle \kappa \rangle^M \nabla T) \quad (5.16a)$$

$$\frac{\partial \langle \rho h \rangle^M}{\partial t} + \nabla \cdot (g^l \langle \rho \rangle^l \langle h \rangle^l \mathbf{v}^l) = \nabla \cdot (\langle \kappa \rangle^M \nabla T) \quad (5.16b)$$

$$\frac{\partial \langle \rho h \rangle^M}{\partial t} + \langle \mathbf{v}^l \rangle \cdot \nabla (\langle \rho \rangle^l \langle h \rangle^l) = \nabla \cdot (\langle \kappa \rangle^M \nabla T) - \langle \rho \rangle^l \langle h \rangle^l \nabla \cdot \langle \mathbf{v}^l \rangle \quad (5.16c)$$

$$\frac{\partial \langle \rho h \rangle^M}{\partial t} + \langle \mathbf{v}^l \rangle \cdot \nabla (\langle \rho \rangle^l \langle h \rangle^l) = \nabla \cdot (\langle \kappa \rangle^M \nabla T) + \langle h \rangle^l \left( \frac{\partial \langle \rho \rangle^M}{\partial t} + \langle \mathbf{v}^l \rangle \cdot \nabla \langle \rho \rangle^l \right) \quad (5.16d)$$

The second term in the RHS of eq. (5.16d) is a heat power (of unit  $W m^{-3}$ ) that adds to the system in the liquid phase (if  $\langle \rho \rangle^l$  is not constant) as well as in the mushy zone (if  $\langle \rho \rangle^l$  and  $\langle \rho \rangle^s$  are not equal). This term is proportional to the solidification rate and expresses the heat generated in regions where the average density is changing and/or a gradient of liquid density is being advected.

### Species conservation

The last conservation principle is applied to the chemical species or solutes. This principle allows predicting macrosegregation when applied to a solidification system, along with the mass, momentum and energy balances. However, the conservation equation should be reformulated in the case of a melt flow driven by shrinkage. Considered assumptions are:

- the solidification path is tabulated using thermodynamic data at equilibrium,
- the macroscopic solute diffusion coefficient  $D^s$  in the solid phase is neglected in the mass diffusive flux term,
- consequence of the static solid phase:  $\langle \rho w v \rangle^M = g^l \langle \rho \rangle^l \langle w \rangle^l v^l + \cancel{g^s \langle \rho \rangle^s \langle w \rangle^s v^s}$ .

The species conservation presents similarities with the energy conservation formulated in the previous section. The main difference is the breakup of the volumetric variable  $\langle \rho w \rangle^M$  into a product of density  $\langle \rho \rangle^M$  and the mass composition  $\langle w \rangle^M$  in the transient term.

For a binary alloy, we write:

$$\frac{\partial \langle \rho w \rangle^M}{\partial t} + \nabla \cdot \langle \rho w v \rangle^M - \nabla \cdot \left( \langle \langle D \rangle^l \rangle \nabla \left( \langle \rho \rangle^l \langle w \rangle^l \right) \right) = 0 \quad (5.17a)$$

$$\langle \rho \rangle^M \frac{\partial \langle w \rangle^M}{\partial t} + \langle w \rangle^M \frac{\partial \langle \rho \rangle^M}{\partial t} + \nabla \cdot \left( g^l \langle \rho \rangle^l \langle w \rangle^l v^l \right) - \nabla \cdot \left( g^l \langle D \rangle^l \nabla \left( \langle \rho \rangle^l \langle w \rangle^l \right) \right) = 0 \quad (5.17b)$$

$$\begin{aligned} & \langle \rho \rangle^M \frac{\partial \langle w \rangle^M}{\partial t} + \langle w \rangle^M \frac{\partial \langle \rho \rangle^M}{\partial t} + \left( \langle \rho \rangle^l \langle w \rangle^l \right) \nabla \cdot \langle v^l \rangle + \langle v^l \rangle \cdot \nabla \left( \langle \rho \rangle^l \langle w \rangle^l \right) \\ & - \nabla \cdot \left( g^l \langle D \rangle^l \nabla \left( \langle \rho \rangle^l \langle w \rangle^l \right) \right) = 0 \end{aligned} \quad (5.17c)$$

The mass balance, eq. (5.14d), gives the following relation when the liquid density is constant:

$$\nabla \cdot \langle v^l \rangle = - \frac{1}{\langle \rho \rangle^l} \left( \frac{\partial \langle \rho \rangle^M}{\partial t} \right) \quad (5.18)$$

If we use the result of eq. (5.18) in eq. (5.17c), then we get the following equation:

$$\langle \rho \rangle^M \frac{\partial \langle w \rangle^M}{\partial t} + \langle w \rangle^M \frac{\partial \langle \rho \rangle^M}{\partial t} = \langle w \rangle^l \frac{\partial \langle \rho \rangle^M}{\partial t} - \langle v^l \rangle \cdot \nabla \left( \langle \rho \rangle^l \langle w \rangle^l \right) + \nabla \cdot \left( g^l \langle D \rangle^l \nabla \left( \langle \rho \rangle^l \langle w \rangle^l \right) \right) \quad (5.19)$$

Applying Voller-Prakash [Voller et al. 1989] variable splitting, the system ends up with only one variable,  $\langle w \rangle^M$ . The splitting is done as follows:

$$\langle w \rangle^l = (\langle w \rangle^l)^t + \langle w \rangle^M - (\langle w \rangle^M)^t \quad (5.20)$$

where the superscript  $t$  refers to the previous time step, and the absence of this superscript corresponds to the unknown variable at the next time step. The chemical species conservation writes, still assuming a constant liquid density:

$$\begin{aligned} & \cancel{\langle \rho \rangle^M \frac{\partial \langle w \rangle^M}{\partial t}} + \cancel{\langle w \rangle^M \frac{\partial \langle \rho \rangle^M}{\partial t}} = \\ & \cancel{\langle w \rangle^M \frac{\partial \langle \rho \rangle^M}{\partial t}} - \langle \rho \rangle^l \langle \mathbf{v}^l \rangle \cdot \nabla \langle w \rangle^M + \nabla \cdot (g^l \langle \rho \rangle^l \langle D \rangle^l \nabla \langle w \rangle^M) \\ & + \frac{\partial \langle \rho \rangle^M}{\partial t} \left[ (\langle w \rangle^l)^t - (\langle w \rangle^M)^t \right] - \langle \rho \rangle^l \langle \mathbf{v}^l \rangle \cdot \nabla \left( (\langle w \rangle^l)^t - (\langle w \rangle^M)^t \right) \\ & - \nabla \cdot \left[ g^l \langle \rho \rangle^l \langle D \rangle^l \nabla \left( (\langle w \rangle^M)^t - (\langle w \rangle^l)^t \right) \right] \end{aligned} \quad (5.21)$$

$$\begin{aligned} & \langle \rho \rangle^M \frac{\partial \langle w \rangle^M}{\partial t} + \langle \rho \rangle^l \langle \mathbf{v}^l \rangle \cdot \nabla \langle w \rangle^M - \nabla \cdot (g^l \langle \rho \rangle^l \langle D \rangle^l \nabla \langle w \rangle^M) = \\ & - \frac{\partial \langle \rho \rangle^M}{\partial t} \left[ (\langle w \rangle^M)^t - (\langle w \rangle^l)^t \right] \\ & + \langle \rho \rangle^l \langle \mathbf{v}^l \rangle \cdot \nabla \left( (\langle w \rangle^M)^t - (\langle w \rangle^l)^t \right) - \nabla \cdot \left[ g^l \langle \rho \rangle^l \langle D \rangle^l \nabla \left( (\langle w \rangle^M)^t - (\langle w \rangle^l)^t \right) \right] \end{aligned} \quad (5.22)$$

It is noted that eq. (5.22) is valid only if both densities  $\langle \rho \rangle^l$  and  $\langle \rho \rangle^s$  are constant but have different values. Since density changes are incorporated in this equation, inverse segregation following solidification shrinkage could be predicted. For the case where macrosegregation is solely due to fluid flow generated by natural or forced convection, i.e. no shrinkage occurs whether due to thermal-solutal contraction or phase change, the overall volume remains constant, hence density is constant.

In this situation,  $\langle \rho \rangle^s = \langle \rho \rangle^l = \langle \rho \rangle^M = \langle \rho \rangle$  and the term  $\partial \langle \rho \rangle / \partial t$  therefore vanishes. After dividing both sides by  $\langle \rho \rangle^M = \langle \rho \rangle^l$ , eq. (5.22) reduces to:

$$\begin{aligned} & \frac{\partial \langle w \rangle^M}{\partial t} + \langle \mathbf{v}^l \rangle \cdot \nabla \langle w \rangle^M - \nabla \cdot (g^l \langle D \rangle^l \nabla \langle w \rangle^M) \\ & = \langle \mathbf{v}^l \rangle \cdot \nabla \left( (\langle w \rangle^M)^t - (\langle w \rangle^l)^t \right) - \nabla \cdot \left[ g^l \langle D \rangle^l \nabla \left( (\langle w \rangle^M)^t - (\langle w \rangle^l)^t \right) \right] \end{aligned} \quad (5.23)$$

### 5.4.2 In the air

The presence of an air domain in our approach is important to follow the free surface of the solidifying metal. For this particular reason, some assumptions are introduced and explained in this section in order to limit unnecessary treatment within the air, since it does not undergo phase change. It should be reminded that we consider air as a single-phase system, hence superscripts  $A$  and  $a$  are interchangeably used.

#### Mass and momentum conservation

To simplify fluid flow resolution in the air, we consider it as incompressible. Therefore, the free metal surface is not disturbed by air flow in its vicinity, but only by shrinkage flow in the liquid metal. With the incompressibility of air, we are saying that any deformation of the free surface is solely due to an air mass increase, coming from the system boundaries. The mass balance hence writes:

$$\nabla \cdot \langle v \rangle^A = \nabla \cdot v^a = 0 \quad (5.24)$$

The air flow is governed by time-dependent incompressible Navier-Stokes equations, as previously done for the metal:

$$\left\{ \begin{array}{l} \langle \rho \rangle^a \left( \frac{\partial v^a}{\partial t} + \nabla \cdot (v^a \times v^a) \right) = \\ - \nabla p^a - 2\mu^a \nabla \cdot \left( \overline{\nabla} v^a + \overline{\nabla}^t v^a \right) + \langle \rho \rangle^a g \\ \nabla \cdot v^a = 0 \end{array} \right. \quad (5.25)$$

The air density  $\langle \rho \rangle^a$  is considered constant along the casting process, therefore thermal gradients in the air that arise due to the low thermal conductivity, do not generate any flow, i.e. no Boussinesq approximation is made on the term  $\langle \rho \rangle^a g$  in eq. (5.25).

#### Energy conservation

It was mentioned in the introduction of the current section that air is a single-phase system that cannot undergo any phase change. Therefore, heat transfer in this domain simplifies to thermal convection and thermal conduction with a low thermal conductivity coefficient,  $\langle \kappa \rangle^a$ , for a single gas phase. The energy balance governs the

air enthalpy  $\langle \rho h \rangle^A$  (which is equal to  $\langle \rho \rangle^a \langle h \rangle^a$  in the current context) as follows:

$$\frac{\partial \langle \rho h \rangle^A}{\partial t} + \nabla \cdot (\rho h \mathbf{v})^A = \nabla \cdot ((\kappa)^A \nabla T) \quad (5.26a)$$

$$\frac{\partial \langle \rho h \rangle^A}{\partial t} + \nabla \cdot ((\rho)^a \langle h \rangle^a \mathbf{v}^a) = \nabla \cdot ((\kappa)^a \nabla T) \quad (5.26b)$$

$$\frac{\partial \langle \rho h \rangle^A}{\partial t} + \mathbf{v}^a \cdot \nabla ((\rho)^a \langle h \rangle^a) = \nabla \cdot ((\kappa)^a \nabla T) \quad (5.26c)$$

### Species conservation

The composition of alloying elements is a crucial quantity to predict in this work. Nevertheless, such prediction is only relevant with metallic species, even if the air is also made up of other chemical species (e.g. nitrogen, oxygen ...). While the other conservation equations (energy, mass and momentum) are important to be solved in the air, the species conservation equation brings no added value to the model when solved in this domain. It may even cause the composition values (i.e. the equation solution) to be unstable near the *M-A* boundary, where mixed properties may lead to unwanted solute transport in both directions across the boundary, hence causing cumulative errors. Therefore, we leave the species resolution in the air to be included in the final monolithic model.

## 5.5 FE monolithic model

The monolithic model combines all conservation equations derived for metal and air in a unique set of equations, to be solved on a Eulerian mesh. This is done by multiplying each conservation equation relative to a domain, obtained in the previous section, by the corresponding Heaviside function then summing all terms, finally using the mixed properties to simplify notations. For each conservation equation, these mixed properties will be properly defined before writing the final monolithic equation.

### 5.5.1 Mass and momentum conservation

We define the Metal+Air system velocity,  $\langle \mathbf{v}^F \rangle$ , as an arithmetic mixing between each domain's relative average fluid velocity, i.e. the domain's own relative fluid phase velocity with respect to solid phases. In the present context, the metal domain consists of a single fluid phase (liquid) and solid phases that form in fixed and rigid structures (assuming that solidification results in undeformable columnar structures, without

## Chapter 5. Macrosegregation with solidification shrinkage

---

any free-to-move equiaxed structure). The air domain entirely consists of a fluid phase. With this notation, we express the monolithic mass balance as:

$$\nabla \cdot \langle \mathbf{v}^F \rangle = \nabla \cdot \left( H^M \langle \mathbf{v} \rangle^M + H^A \langle \mathbf{v} \rangle^A \right) \quad (5.27)$$

$$\nabla \cdot \langle \mathbf{v}^F \rangle = H^M \nabla \cdot \langle \mathbf{v} \rangle^M + H^A \cancel{\nabla \cdot \langle \mathbf{v} \rangle^A} + \cancel{\nabla H^M \cdot \left( \langle \mathbf{v} \rangle^M - \langle \mathbf{v} \rangle^A \right)} \quad (5.28)$$

$$\nabla \cdot \langle \mathbf{v}^F \rangle = H^M \nabla \cdot \langle \mathbf{v}^l \rangle \quad (5.29)$$

where we used the relation [eq. \(5.13\)](#) in the case of a fixed rigid solid to obtain [eq. \(5.29\)](#). As for the second term in [eq. \(5.28\)](#), we have made the assumption that air is incompressible, hence  $\nabla \cdot \langle \mathbf{v} \rangle^A = 0$ . Therefore any volume variation of the metal domain, will trigger an air inflow or suction effect through the surface boundaries of the air domain. The third and last term in the same equation expresses a velocity jump at the interface. In our case, we neglect this contribution by assuming that both velocities tend to be equal when the interface thickness tends to zero.

Finally, using the monolithic mass balance [eq. \(5.14d\)](#), we get:

$$\nabla \cdot \langle \mathbf{v}^F \rangle = H^M \left( -\frac{1}{\langle \rho \rangle^l} \left( \frac{\partial \langle \rho \rangle^M}{\partial t} + \langle \mathbf{v}^l \rangle \cdot \nabla \langle \rho \rangle^l \right) \right) \quad (5.30)$$

In order to derive the monolithic momentum balance, we first define a fluid fraction,  $g^F$ , as an arithmetic mixing between liquid and air fractions across the interface:

$$g^F = H^M g^l + H^A g^a = H^M g^l + H^A \quad (5.31)$$

This quantity will be essential for the monolithic Darcy term. We have seen in the previous chapter that adding the Darcy term for the metallic alloy momentum equation modifies the shape of the latter, dividing all terms by the liquid fraction,  $g^l$ . The presence of this dissipation term in one domain, obliges us to keep it in both domains but "deactivate" it where it is useless, i.e. in the air. This is done by computing a fictitious permeability in the air as function of the air fraction using the Carman-Kozeny model, as used previously for the metal in [eq. \(1.3\)](#). We may speak of level set mixing for the Darcy term. It has a double advantage:

1. the consistency in shape is kept between both domains equations, thus easily deriving the monolithic system;
2. since the monolithic system retains the shape of the monodomain equation, the VMS solver does not require further implementation updates and subsequent validation.

The first point implies that the Darcy term should also be added in the air's momentum balance, but remains inactive by imposing a high permeability in the air, while having realistic values where needed, namely in the metal domain. The modified permeability,  $\tilde{K}$ , depends on the fluid fraction (eq. (5.31)) as follows:

$$\tilde{K} = \frac{\lambda_2^2 g^{F^3}}{180 (1 - g^F)^2} \quad (5.32)$$

Depending on the values of this quantity, the extent to which the Darcy becomes imposing in Navier-Stokes varies as follows:

- $\tilde{K}^{-1} \rightarrow 0$  (completely permeable), then Darcy's term is negligible in Navier-Stokes resolution,
- $\tilde{K}^{-1} > 0$  (slightly permeable), then fluid flow is greatly dissipated due to a decreasing permeability,
- $\tilde{K}^{-1} \rightarrow \infty$  (non permeable), then no fluid flow may exist.

These 3 cases are graphically represented in fig. 5.5, showing the different values along with the transitions with respect to phases and domains distribution.

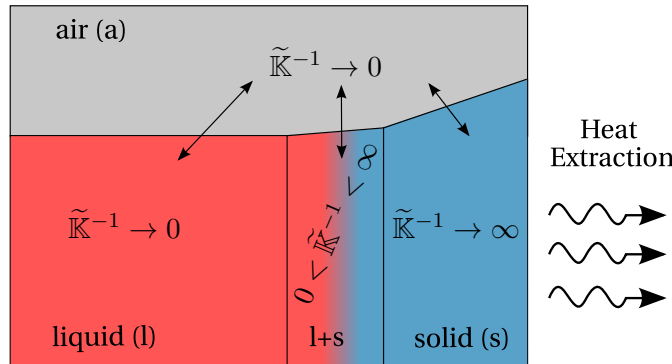


**Fig. 5.5** – Schematic representation of an ingot undergoing solidification while shrinking. The inverse of the modified permeability,  $\tilde{K}^{-1}$ , falls to zero in the air and liquid phases, indicating that the Darcy term is only activated in the solid and liquid+solid regions. The arrows indicate three different transitions of the Darcy term between the air and metal domains.

As for the weight force in both domains, it is taken into account via eq. (5.35). The phase densities may vary as functions of other parameters such as temperature or phase composition ( $\langle \rho \rangle^l$  depends on both), creating buoyancy forces of convection inside the fluid.

In our approach, since we are only interested in liquid's flow, we keep the air phase density  $\langle \rho \rangle^a$  constant, so as to prevent a mixture of forces around the level set, which

helps stabilise the fluid flow resolution. The mechanical properties are mixed as follows:

$$\text{Density} : \hat{\rho} = H^M \langle \rho \rangle^l + H^A \langle \rho \rangle^a \quad (5.33)$$

$$\text{Dynamic viscosity} : \hat{\mu} = H^M \mu^l + H^A \mu^a \quad (5.34)$$

$$\text{Weight force} : \hat{\rho} \bar{g} \mathbf{g} = H^M g^l \langle \rho \rangle^l \mathbf{g} + H^A g^a \langle \rho \rangle^a \mathbf{g} = H^M g^l \langle \rho \rangle^l \mathbf{g} + H^A \langle \rho \rangle^a \mathbf{g} \quad (5.35)$$

The momentum balance can now be obtained from  $H^M \times \text{eq. (5.15)} + H^A \times \text{eq. (5.25)}$ , after adapting [eq. \(5.25\)](#) to account for a fictitious Darcy term :

$$\left\{ \begin{array}{l} \hat{\rho} \left( \frac{\partial \langle \mathbf{v}^F \rangle}{\partial t} + \frac{1}{g^F} \nabla \cdot (\langle \mathbf{v}^F \rangle \times \langle \mathbf{v}^F \rangle) \right) = \\ - g^F \nabla p - 2\hat{\mu} \nabla \cdot \left( \overline{\nabla} \langle \mathbf{v}^F \rangle + \overline{\nabla^t} \langle \mathbf{v}^F \rangle \right) - g^F \hat{\mu} \tilde{\mathbb{K}}^{-1} \langle \mathbf{v}^F \rangle + \hat{\rho} \bar{g} \mathbf{g} \\ \nabla \cdot \langle \mathbf{v}^F \rangle = H^M \left( -\frac{1}{\langle \rho \rangle^l} \left( \frac{\partial \langle \rho \rangle^M}{\partial t} + \langle \mathbf{v}^l \rangle \cdot \nabla \langle \rho \rangle^l \right) \right) \end{array} \right. \quad (5.36)$$

### 5.5.2 Energy conservation

To write the monolithic energy conservation equation, we are interested in [eqs. \(5.16d\)](#) and [\(5.26c\)](#). Mixed quantities from these equations are defined by:

$$\text{Total enthalpy} : \widehat{\langle \rho h \rangle} = H^M \langle \rho h \rangle^M + H^A \langle \rho h \rangle^A \quad (5.37)$$

$$\text{Fluid phases enthalpy} : \widehat{(\rho h)^F} = H^M \langle \rho \rangle^l \langle h \rangle^l + H^A \langle \rho \rangle^a \langle h \rangle^a \quad (5.38)$$

$$\text{Average thermal conductivity} : \widehat{\langle \kappa \rangle} = H^M \langle \kappa \rangle^M + H^A \langle \kappa \rangle^A \quad (5.39)$$

$$\text{Average heat change} : \widehat{\Phi} = H^M \langle \rho \rangle^l \langle h \rangle^l \nabla \cdot \langle \mathbf{v}^l \rangle \quad (5.40)$$

where [eq. \(5.37\)](#) will be used to predict the transient change in the system's global enthalpy, [eq. \(5.38\)](#) for the fluid-transported enthalpy in both domains while [eq. \(5.39\)](#) expresses the global energy conduction in the system. The last equation, [eq. \(5.40\)](#), is only present in the domain whose volume is changing, that is the metal in our case. Using the mixed thermophysical properties, [eqs. \(5.16d\)](#) and [\(5.26c\)](#) can now be mixed to obtain:

$$\frac{\partial \widehat{\langle \rho h \rangle}}{\partial t} + \langle \mathbf{v}^F \rangle \cdot \nabla \widehat{(\rho h)^F} = \nabla \cdot \left( \widehat{\langle \kappa \rangle} \nabla T \right) + \widehat{\Phi} \quad (5.41)$$

The solution of eq. (5.41) is  $\widehat{\langle \rho h \rangle}$ , a mixed field between both domains average volumetric enthalpies.

Using the current approach for the energy, any motion of the  $M$ - $A$  boundary is energetically translated into a phase change between the air phase on one side and the metallic phases on the other side. Chen [2014] tackled this problem by reformulating the energy equation with the smoothed Heaviside functions in order to prevent this purely numerical phenomenon. However in the current work, we prefer avoiding this numerical artefact by using the same tabulated phase enthalpy properties (or specific heat if the tabulation approach is not used) for the air and the liquid phase. This assumption made on only for the  $l$ - $a$  is compatible with definition of the mobile  $M$ - $A$  boundary made in section 5.3.2.

### 5.5.3 Species conservation

Unlike monolithic energy conservation which applies to whole metal+air system, the monolithic species conservation equation is dedicated to the transport of *metallic* chemical species, meaning that the air does not contain any metallic species to be transported. This physical specificity leaves us with two main resolution strategies:

**Monolithic strategy:** we combine two species conservation equations into a single monolithic equation. We compute the conservation of chemical species in both the metal and the air, considering the latter as a *fictitious metal*. Then, we control solute transport between both domains by:

1. initial composition: the air average composition (which is equal to the composition of the air phase in our case) should normally be initialised to zero. However, this initialisation creates a composition gradient across the  $M$ - $A$  boundary, creating a driving force for diffusion. Another option would be initialising both domains to the same value,  $\langle w_0 \rangle^M = \langle w_0 \rangle^A$ . This has the advantage of keeping solutal gradients to the lowest during the boundary motion and delaying as much as possible the occurrence of artificial solute transport, until the  $s$ - $a$  interface forms gradually,
2. solute diffusion: a very low macroscopic solute diffusion coefficient is used, at most a thousand times less than its value in the melt,  $\langle D \rangle^a \ll \langle D \rangle^l$ . The low solute diffusion in the air may not completely ensure a zero solute flux at the  $M$ - $A$  boundary, but it helps maintaining a weak diffusive transport,

3. solute advection: the computed fluid velocity,  $\langle v^F \rangle$ , is postprocessed to be zero in the species equation for the air, thus suppressing the advective solute transport term influence which can be more important than the diffusive transport.

**Non-monolithic strategy:** this strategy aims to avoid the difficulty of dealing with a *fictitious* solute equation for the air. This is done by considering only the metal's species conservation equation, [eq. \(5.22\)](#). The solution of the latter is the metal's average composition,  $\langle w \rangle^M$ . From this solution, we determine the monolithic composition value,  $\widehat{\langle w \rangle}$ , :

$$\widehat{\langle w \rangle} = H^M \langle w \rangle^M + H^A \langle w_0 \rangle^M \quad (5.42)$$

where we directly initialise the composition in the air to the metal's nominal composition. This strategy has the advantage of being simpler, especially we do not have to deal with density terms (which can be seen for example in [eq. \(5.22\)](#)) as dictates the previous monolithic strategy, knowing that air density remains constant in this work. In the next section, we present a simple 1D solidification case with solidification shrinkage, in which we test the segregation results given by each strategy.

## 5.6 1D application: solidification with inverse segregation

### 5.6.1 Geometry and boundary conditions

A simple but very efficient way of analysing the model is to test it through a 1D flow configuration with energy and species conservation. For this purpose, we take an aluminium-silicon alloy with the properties shown in [table 5.1](#).

The rectangular 2D mesh having the dimensions  $0.14\text{ m} \times 0.001\text{ m}$ , consists of metal and air. Initially the air column's height is only  $0.04\text{ m}$  and the remainder of the length is the metal. [Figure 5.6](#) shows the geometry and boundary conditions used for the simulations in this section. In the same figure, the thermal and mechanical boundary conditions are shown. In the latter, velocity-slip conditions were imposed on the lateral boundaries while a no-slip was used at the bottom where heat is extracted, and a free-velocity condition is set at the top of the domain, to ensure a 1D air flow from the top air inlet.

In this case, imposing slip conditions on lateral sides is two-fold: on one hand, we need to ensure that the fluid flow solution remains one-dimensional, hence symmetry on the boundaries solves the issue, while on the other hand during solidification, the resulting feeding flow should be able to transport the interface intersecting with

boundary nodes. If boundary velocities are zero, then the interface transport will face problems at these boundary nodes. This is indeed an important and relevant point in the next 2D test case.

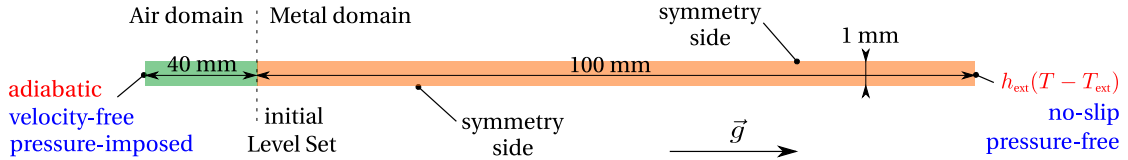


**Fig. 5.6** – Computational configuration for the 1D inverse segregation case showing the domain geometry with the applied boundary conditions to it as well as the gravity vector. The symmetry sides represent the following set of boundary conditions: adiabatic, zero normal velocity, free tangential velocity and pressure-free.

### 5.6.2 Shrinkage without macrosegregation

The first simulation is for solidification without any segregation, hence a unique solidification path is considered at  $w_0 = 7$  wt.%, shown in [fig. 5.8](#). This case is interesting as a reference case, where we can study volume shrinkage and level set behaviour in a simple segregation-free configuration. We first use a homogeneous isotropic mesh of constant size  $h = 200 \mu\text{m}$ . The liquid and solid phase densities are assumed constant and respectively equal to  $2600 \text{ kg m}^{-3}$  and  $2800 \text{ kg m}^{-3}$ . This density difference is equivalent to a ratio of  $\beta_{SS} = (\langle \rho \rangle^s - \langle \rho \rangle^l) / \langle \rho \rangle^s$ , also termed as *solidification shrinkage* by [Flemings and Nereo \[1967\]](#). In the current conditions,  $\beta_{SS}$  is constant and equal to 7.14 %. The domain is initially meshed before any resolution, as shown in [fig. 5.7](#), in a way to reduce interpolation errors that may cause coarse elements within the transition of fluids density and dynamic viscosity, reminding that these parameters are crucial for the stability of the velocity solution used later in the transport step. The chosen mixing laws are arithmetic for the density and logarithmic for the viscosity. The mesh properties are given in [table 5.2](#).

At a first glance, results show that the interface stability is compromised by a chosen time step for a given mesh size, and that the interface dynamics requires attention even before investigating the feeding flow created by solidification. As a demonstration, [fig. 5.9](#) shows the effect of different time steps with the same adaptive meshing parameters. For time steps greater than 0.01 s, Navier-Stokes computations did not converge resulting in a high artificial flow quickly destabilising the interface. It should be noted that the frame corresponding to 0.02 s was taken at an earlier time than the two other frames.

Although no solidification has yet started at 100 s, a two-dimensional flow is observed around the interface, while tends to  $10^{-8} \text{ m s}^{-1}$  elsewhere in the ingot. [Figure 5.9](#) con-

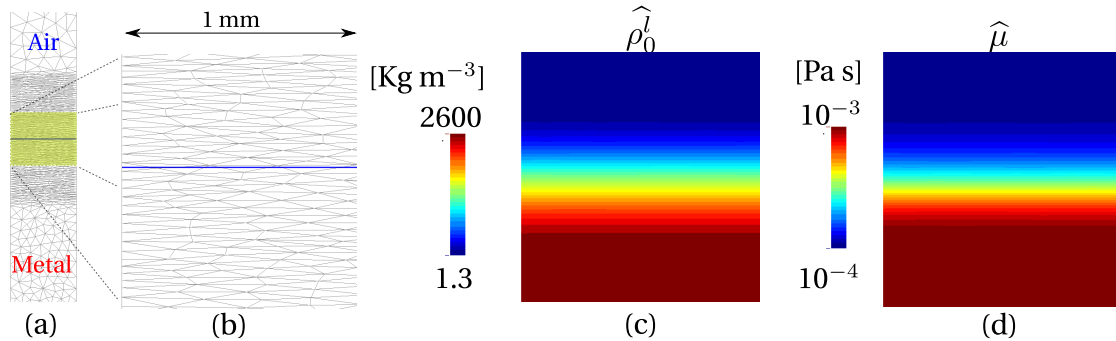


**Fig. 5.7** – Snapshots of (a,b) the initial adapted mesh around the interface with different mesh sizes in the air and the metal. The adapted region is stretched beyond the level set mixing thickness to ensure better interpolation around the interface, in case of emergence of diffusion instabilities. To the right, (c) the reference fluid density and (d) viscosity are plotted in the transition zone. The thick blue line represents the zero isovalue of the distance function.

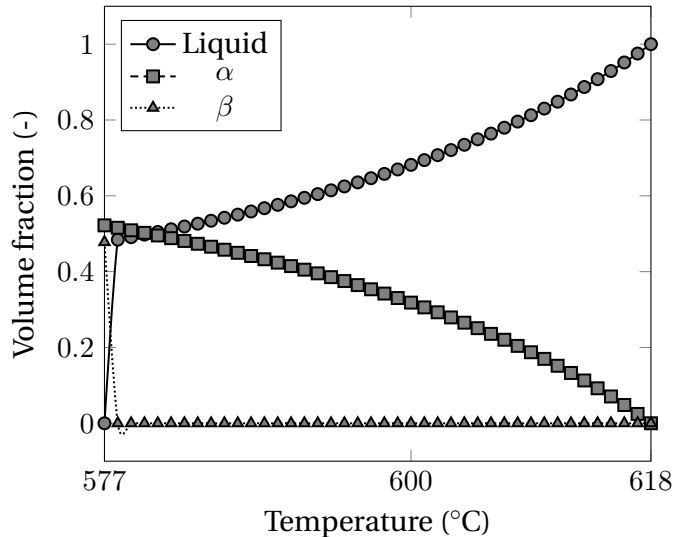


**Fig. 5.8** – Unique solidification path at nominal composition for the shrinkage case without macrosegregation in Al-7 wt.% Si, showing the liquid phase, aluminium-rich  $\alpha$  phase and the silicon-rich  $\beta$  phase, which partly forms the eutectic structure.

## 5.6. 1D application: solidification with inverse segregation

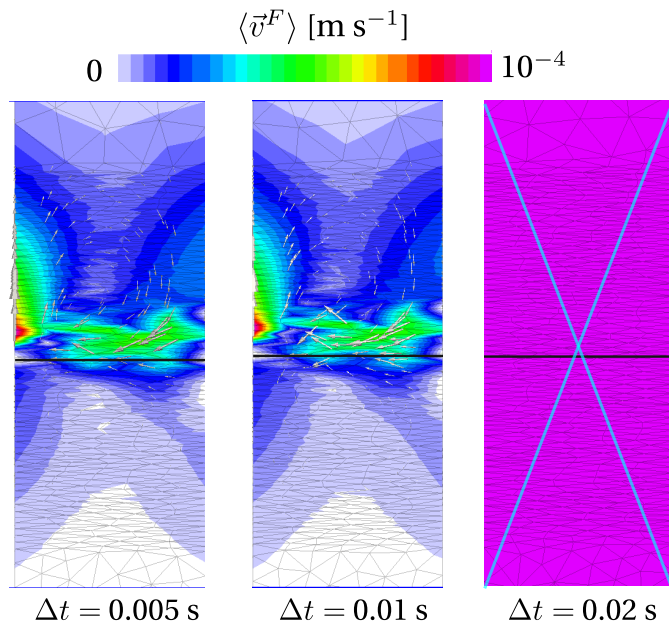


**Fig. 5.9** – Three average fluid velocity frames at different time steps: 0.005 s, 0.01 s and 0.02 s. The first and second frame are taken after 50 seconds of cooling while for the last frame, the frame was taken after only 1 second of cooling, thus it is crossed to show non-convergence. The thick black line represents the zero isovalue of the distance function. Properties are given in [tables 5.1](#) and [5.3](#) under case "R".

firms that this flow is still predicted at smaller time steps. This flow seems like a pure numerical response to the properties jump across the interface, namely density and dynamic viscosity. It is also noted that the interface position is not modified by the neighbouring currents, that reach a maximum magnitude of  $10^{-4} \text{ m s}^{-1}$ . Therefore, the optimal time step for this simulation is set to 0.01 s, and we refer to it as case R, which stands for "real" air.

The fact that properties transition is crucial in the solution stability, is investigated by 2 reference cases, having equal properties (density and dynamic viscosity) but with different time steps, 0.01 (case A1) and 0.1 s (case A2), where "A" stands for artificial. All simulation cases are grouped in [table 5.3](#).

When the air domain is given the metal's properties, it becomes denser and more viscous by several orders of magnitude. [Figure 5.10](#), in which cases A1 and A2 are compared, shows no noticeable sign of velocity instability near the interface before 200 s. It can be explained by the fact that the air behaves mechanically like a fluid metal given similar properties, therefore no steep transitions are computed at the interface. However, it is interesting to compare results of [fig. 5.10a](#) and [fig. 5.10b](#) at 600 s. For case A1, the interface is slightly skewed due to slower flow at the left side of the interface, while for case A2, the flow disturbs the interface deforming it until the end

## Chapter 5. Macrosegregation with solidification shrinkage

---

of solidification, as seen at 1000 s. This shows the importance of the chosen time step in the Navier-Stokes solver.

In contrast, [fig. 5.11b](#) shows more viable results as far as the level set transport is concerned. From 200 s to 800 s, the local flow instability (discussed earlier in [fig. 5.9](#)) is sustained, even until after solidification is complete. However, in regions of 100% metal and 100% air the computed velocity is nearly the same order of magnitude as predicted for all three simulations. Finally, in [fig. 5.11b](#), we notice a recirculating air flow in the vicinity of the interface as no metal shrinkage may further occur once solidification is complete, thus air flows freely in and out of the upper boundary with a very low magnitude ( $\approx 10^{-7} \text{ m s}^{-1}$ ), while impinging on the metal-air surface. Regarding the CPU times, cases A1 ran for 14 hours, case A2 took only 2 hours while case R ran for 23.3 hours. To summarise, we can see conclude from the previous results, the following points:

1. Greater differences in mechanical properties of fluids across the level set impose using smaller time steps,
2. When real properties are used, smaller time steps are needed to capture the variations across the moving level set, hence inducing longer simulation time,
3. In a situation where the flow dynamics in the non-metallic (gas) domain is not a primary objective, one can use artificial properties instead of the real values, hence gaining in computation time at the expense of the flow prediction accuracy.

### Mass conservation study

In order to get a better idea about the performance of our model, a mass conservation study is performed hereafter. We define the metal's mass as a function of the metal's average density and the Heaviside function relative to the metal domain, as follows:

$$m^M = \int_{\Omega} H^M \langle \rho \rangle^M \, d\Omega \quad (5.43)$$

Then, the mass conservation can be monitored by processing [eq. \(5.43\)](#) at each time step, and computing the relative mass change by writing:

$$m_{\%}^M = \frac{m^M - m_0^M}{m_0^M} \times 100 \quad (5.44)$$

The relative mass change gives us information on the level set transport. As the current case is 1D and phase densities are constant throughout the simulation, mass conserva-

## 5.6. 1D application: solidification with inverse segregation

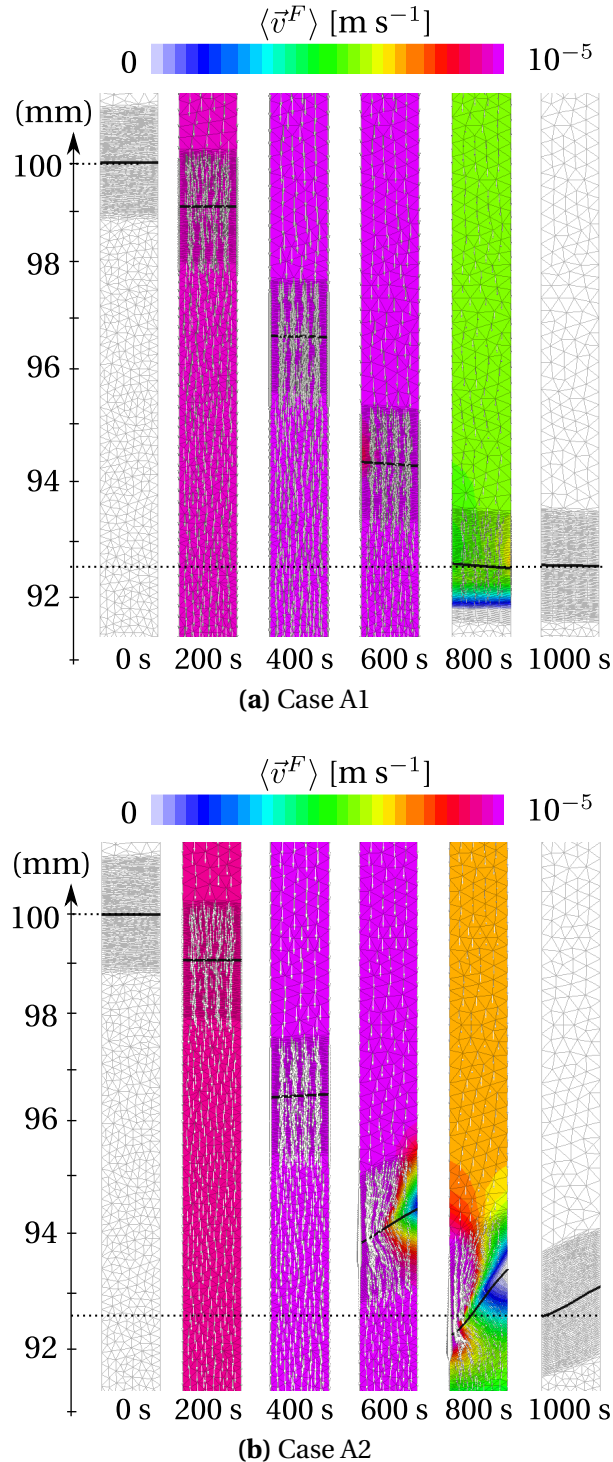


**Fig. 5.10** – Comparison of two simulations at several stages of solidification ending shortly after 800 s. The results shows the influence of density and viscosity properties across the level set interface. The plotted field is the average fluid velocity, on which the corresponding nodal vectors are superimposed, mainly pointing downwards, i.e. towards the solidification front. The thick black line represents the zero isovalue of the distance function. Properties are given in tables 5.1 to 5.3.

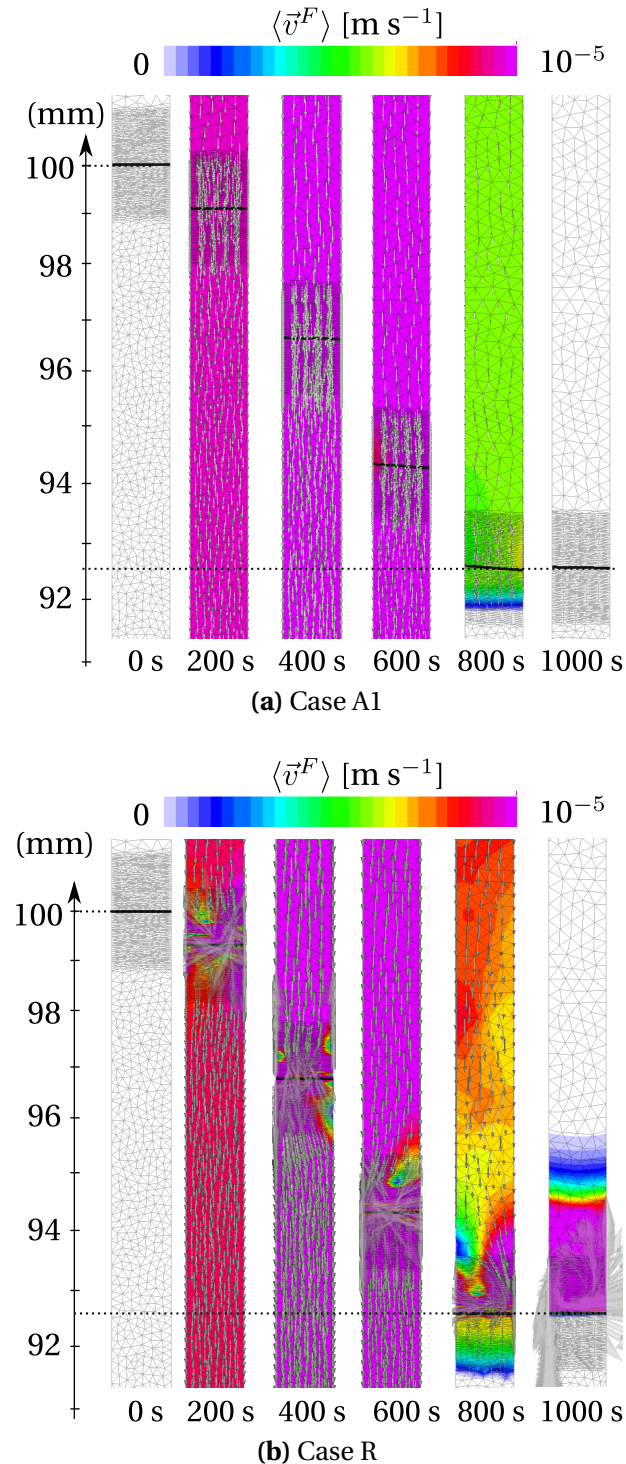


**Fig. 5.11** – Comparison of two simulations at several stages of solidification ending shortly after 800 s. The results shows the influence of density and viscosity properties across the level set interface. The plotted field is the average fluid velocity, on which the corresponding nodal vectors are superimposed, pointing towards the solidification front. Properties are given in tables 5.1 to 5.3.

tion can be checked in a much simpler approach than by checking eq. (5.44). Since we know the initial metal's column length,  $l_0^M$ , and the expected solidification shrinkage is 7.14 %, we should expect a final length of  $l_f^M = (1 - \beta_{SS}) l_0^M = 92.86$  mm.

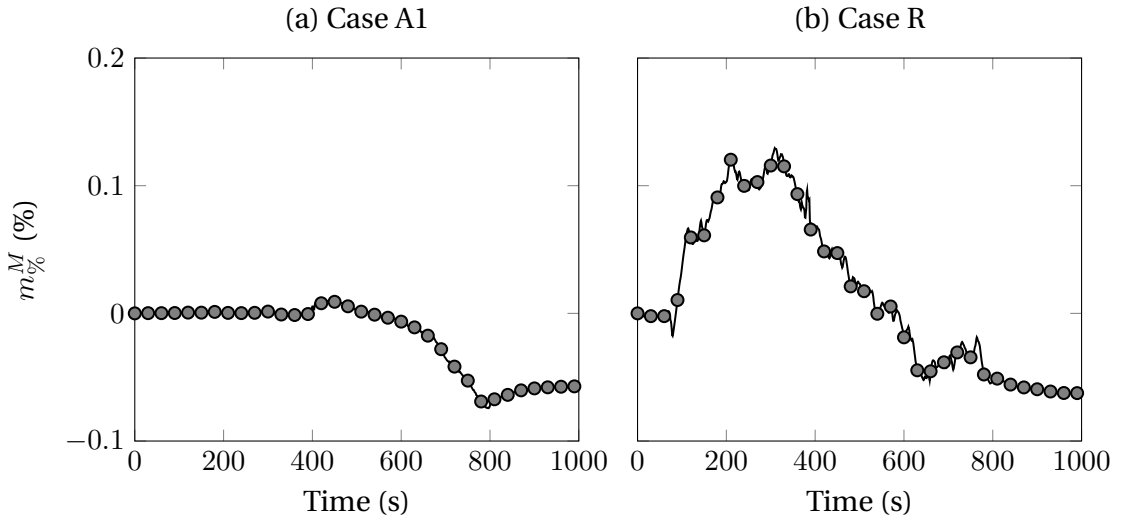


**Fig. 5.12** – Variation of the metal's mass versus solidification time in cases A1 and R.

In the previous section, we observed *M-A* boundary instability problems taking place around 400 s of cooling, where the flow begins slightly losing its one-dimensional shape. Although it was clearly seen in fig. 5.10b, it applies for both cases, whether air properties are equal (cases A1 and A2) or different (case R) than the liquid's properties across the interface. The mass variation plots in fig. 5.12 confirm these observations, since the metal's mass does not remain constant during simulations. Therefore, we can deduce that regardless of the time step and the level set mixing of properties, transport problems may occur.

The level set method is known to have poor mass conservation properties. However, the mass variation we see in the previous plots is more related to a physical problem: **at which velocity does the *M-A* boundary move?** In our simulations, we systematically considered the Navier-Stokes solution,  $\langle v^F \rangle$ , to transport the metal-air boundary. This solution is equal to  $\langle v^l \rangle = g^l v^l$  in the metal domain. Furthermore, we showed in the introduction of this chapter that the *M-A* boundary actually consists of several interfaces, and when the mushy zone overlaps with the level set mixing zone, we cannot track the boundary between the porous medium (described in fig. 5.4), which induces concept errors. In the light of these facts, we can try to limit as much as possible the motion of the porous medium boundaries, once the mushy zone has reached the level set mixing zone, and test the influence on mass conservation. To do so, we firstly advise to keep a very small thickness interface, in order to delay the

previously explained overlap. Moreover, we suggest computing the transport velocity, used in the level set transport equation (eq. (2.62)), at each node as follows:

$$v = \begin{cases} \langle v^l \rangle & \text{if } g^l > g_{BL}^l \\ 0 & \text{otherwise} \end{cases} \quad (5.45)$$

where  $g_{BL}^l$  is the threshold for the liquid fraction, below which we consider that the interface should not be transported. Figure 5.13 shows the mass variation for three blocking fractions: 0, 50, 75 and 99 percent. The first value corresponds the case where the Navier-Stokes solution is directly passed to the transport solver, corresponding to the previously presented result in fig. 5.12b. For the last value, we consider that as soon as a portion of the M-A boundary becomes in contact with the low solid fraction part, the liquid in the mushy zone becomes immobile. It is clearly seen that the consequence on the mass conservation is not good, as the mass increases up to 3% while the eutectic front is consuming the liquid within the mushy zone, and no further shrinkage is allowed. We conclude that this strategy adds metal mass in the system, unlike the initial strategy with  $g_{BL}^l = 0\%$  that removes mass.

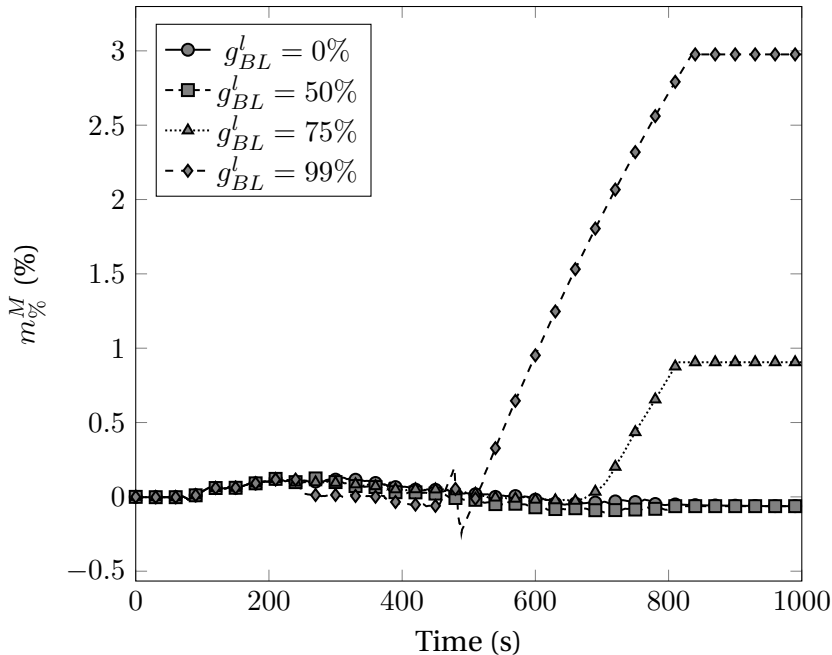


**Fig. 5.13** – Relative mass change versus time for different blocking fractions  $g_{BL}^l$  in the transport solver.

In fig. 5.14, we plot again the same curves as in fig. 5.13, but keeping the values of  $g_{BL}=0\%$  and  $g_{BL}^l=50\%$ . We notice that both values produce the same results until

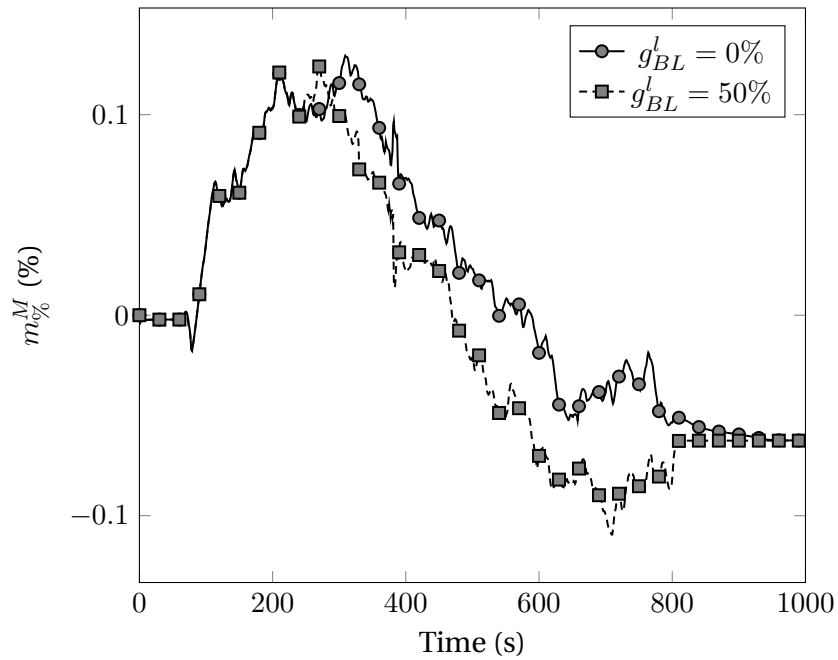


**Fig. 5.14** – Relative mass change versus time only for 0% and 50% blocking fractions.

about 300 s. Then, when the mushy zone reaches the interface region, differences appear as a consequence of the reduced transport for the higher blocking fraction. However, it should be pointed out that the differences between 300 s and 800 s are not important because the permeability predicted by the Carman-Kozeny model, falls to zero quickly for liquid fractions less than about 60%.

In the current application, it is not clear whether the idea of the blocking fraction is useful or not, since the feeding flow occurs in a single direction and solidification takes place far from the interface. Since the results obtained zero blocking fraction were better than with increasing values of  $g_{BL}^l$ , further simulations will adopt this strategy.

### 5.6.3 Shrinkage with macrosegregation

In this section, we consider species conservation equation, in addition to energy conservation and fluid momentum conservation equations, studied in the previous section to predict solidification shrinkage. The interesting point here is to study the formation of macrosegregation in a one-dimensional configuration and the effect of solidification shrinkage on it. As shown in chapter 2, our approach to solve the energy equation relies on tabulations of various solidification paths. In this case, we will generate a simple tabulation based on a phase diagram with linear liquidus and solidus

## Chapter 5. Macrosegregation with solidification shrinkage

---

lines, whose properties are reminded in [table 5.4](#).

Using the values from [table 5.4](#), a python program generates a *CimLib*-compatible tabulation assuming lever rule as microsegregation law, with a 0.1 wt.% step for average composition within an offset of 20% around the nominal value, i.e. 29 composition values within the interval [5.6,8.4]wt.%Si. For temperature, a range between  $T_E=577\text{ }^\circ\text{C}$  and  $630\text{ }^\circ\text{C}$  is considered with a step of  $1\text{ }^\circ\text{C}$ , corresponding to 54 values. It is noted that for this application, the phase enthalpies are deduced from constant specific heat of each phase as well as constant latent heat, given in [table 5.1](#).

In order to understand better the effect of shrinkage combined with macrosegregation, we plot in [fig. 5.15](#), the cooling curves from 4 different simulations:

- Grey curve - case G0: pure diffusion solidification with  $\langle\rho\rangle^l = \langle\rho\rangle^s$  (no level set) used previously in chapter 2 for validation; we use it as a reference case,
- Green curve - case G: convection-diffusion solidification with  $\langle\rho\rangle^l = \langle\rho\rangle^s$  (with level set) at a constant average composition
- Blue curve - case B: convection-diffusion solidification with  $\langle\rho\rangle^l \neq \langle\rho\rangle^s$  (with level set) at a constant average composition; this curve is plotted in [fig. 5.15a](#) and [fig. 5.15b](#),
- Red curve - case R (not to be confused with case R defined in the previous section): convection-diffusion solidification with  $\langle\rho\rangle^l \neq \langle\rho\rangle^s$  (with level set) and macrosegregation.

### Shrinkage effect on temperature

If we focus first on [fig. 5.15a](#), we first compare solidification cases G and G0, both with equal phase densities, hence no shrinkage. This first comparison shows that the introduction of the level set method, compared to a monodomain configuration, heats up the overall sample temperature by about  $4\text{ }^\circ\text{C}$  (difference between green and grey curves), causing solidification to finish a few seconds later than predicted in case G0. This is because we set a very high initial temperature in the air,  $800\text{ }^\circ\text{C}$ , to prevent a brutal diffusive flux that may lead to surface solidification in the metal. As the sample cools down, the air conductivity ( $10^{-2}\text{ W m}^{-1}\text{ K}^{-1}$ ) is not low enough to prevent a small diffusion flux in the metal's direction. However, since in both cases the cooling trend is predicted, we will keep the same thermal diffusion properties in the air, so as not to use unreal conductivity values, but we keep in mind that the current approach delays the solidification.

The second comparison is done between cases G and B, both using the level set approach but only case B considers solidification shrinkage. We notice that blue curve

## 5.6. 1D application: solidification with inverse segregation

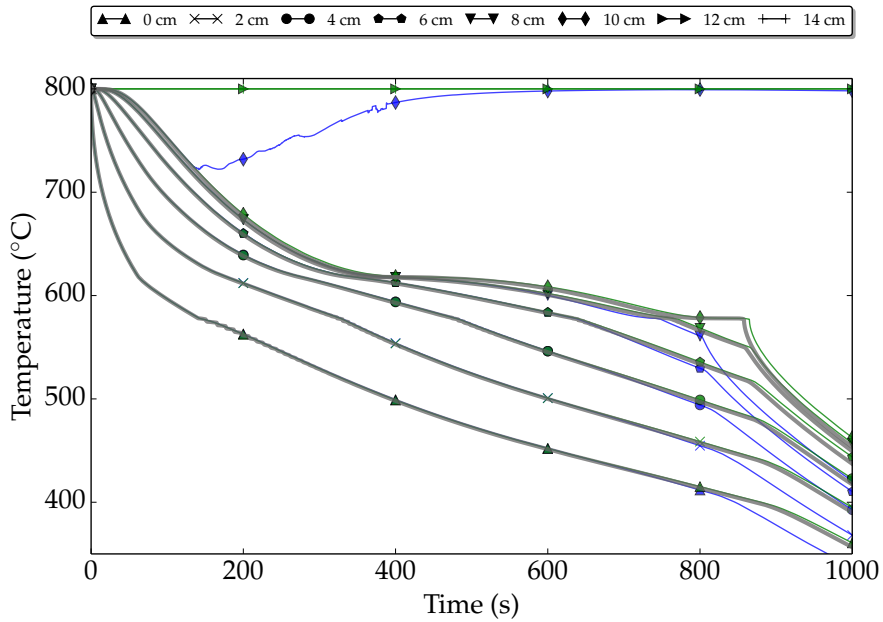
---

temperature of the sixth Eulerian sensor rises steadily from 180 s to 600 s reaching a constant temperature of 800 °C, the air's temperature. This rise confirms the metal has shrunk in length (volume in 3D), becoming less than 10 cm, hence replaced by air that entered through the open top boundary. The 6th sensor (at 100 mm) was initially on the metal-air boundary, then later relocated in the air after shrinkage. The sensors at 12 cm and 14 cm are not shown in this figure as the simulation done for the pure diffusion without level set, the air domain does not exist. Another interesting difference resulting from shrinkage is that solidification ends sooner by about 70 s, compared to the pure diffusion case. As mass is almost perfectly conserved in both cases, cooling flux is the only factor that may accelerate the cooling. The imposed cooling boundary condition is a Fourier-type with the same heat transfer coefficient  $h_{ext}$  in both cases. However, a shrinkage flow transports energy in its direction, i.e. towards the solidification front, and thus raising slightly the temperature in regions close to the cool wall. Therefore, the Fourier flux proportional to the local temperature increase and the sample solidifies earlier.

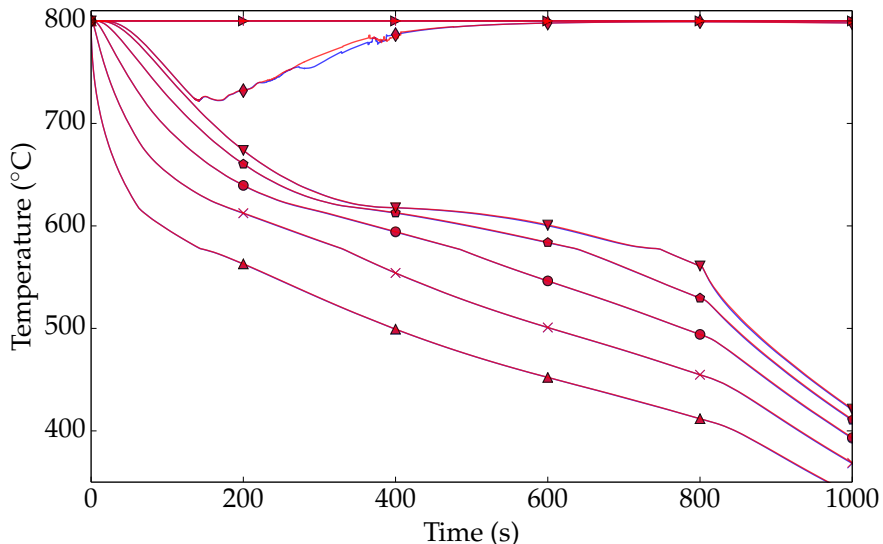
Finally, [fig. 5.15b](#) compares cases B and R, both with unequal phase densities but also predicting macrosegregation in the latter case. Differences are not striking, as temperatures along the metal sample are the same.

### Shrinkage effect on average composition

[Figure 5.16](#) shows snapshots at different times of the shrinkage flow caused by the density difference between liquid and solid phases. By solid phases, we mean the primary solid phase assumed as a dendritic structure, then the primary and secondary solid phases forming together the eutectic that we see starting at 150 s in [fig. 5.16](#). We can see that some solute segregation has already initiated in the mushy zone at 100 s. However, the average composition reaches a positive peak of  $\langle w \rangle = \text{Al-7.4 wt.\% Si}$  with the initiation and progression of the eutectic front. The sudden transformation of the remaining liquid in the mushy zone into eutectic solid, triggers a local velocity increase (real intrinsic velocity) as each node's density varies from  $\langle \rho \rangle^l$  to  $\langle \rho \rangle^s$  in a single time step, at eutectic temperature. The velocity increase, shown later in [fig. 5.18](#), causes species transport in the opposite direction of solidification, hence solute "freezes" in the eutectic structure leading to positive macrosegregation in the first solidified nodes. This phenomenon is better known as inverse segregation. As the transport continues in the same direction, solute is progressively depleted in the remaining liquid, causing negative macrosegregation at nodes located between 2 cm and 7 cm from the cold wall. [Figure 5.16](#) shows only the first 1.5 cm of the solidifying sample, therefore a complete segregation profile is plotted along the sample length in



**(a)** Solidification shrinkage effect: grey curves correspond to a pure diffusion in a metal monodomain case, green curves consider the latter case but with level set (metal and air domains) while blue curves correspond to a shrinkage-driven flow case. All cases are solved without macrosegregation.



**(b)** Macrosegregation effect: blue curves represent the same simulation corresponding to the shrinkage-driven flow without macrosegregation, while the red curves correspond to a simulation of shrinkage-driven flow with macrosegregation.

**Fig. 5.15** – Cooling curves at different fixed positions from 0 to 14 cm. where we show (a) the effect of solidification shrinkage on temperature history without any macrosegregation and show (b) the effect of macrosegregation on temperature in the presence of solidification shrinkage. Initial  $M-A$  boundary: 10 cm.

## 5.6. 1D application: solidification with inverse segregation

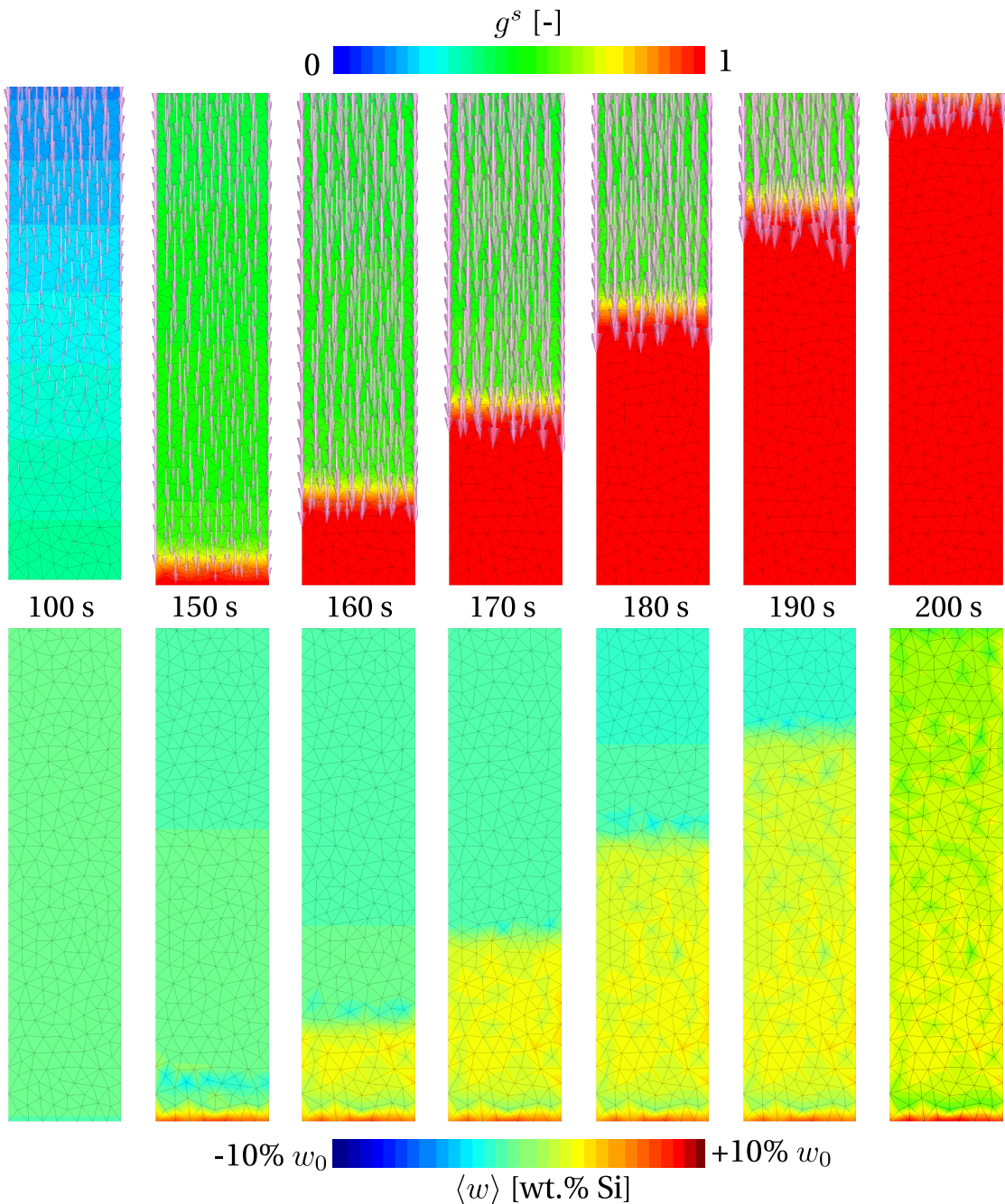


**Fig. 5.16** – Zoom on the lower part, approximately 1.5 cm of the alloy close to the cooling boundary condition. The upper row of figures show the evolution of volume solid fraction, when eutectic transformation takes place. The vectors represent the direction of the average velocity field, with a length proportional to the magnitude. The lower row of figures show for the same time increments, the solute redistribution, clearly changing behind the eutectic front.

[fig. 5.17a](#), showing thus the negative macrosegregation as previously explained. However, from 7 cm to the *M-A* boundary, the average composition rises as clearly shown in [fig. 5.17a](#). This looks more like a numerical instability than a physical rise in concentration. Bearing in mind that a reduced solute diffusion coefficient is imposed in the air domain  $1.5 \times 10^{-12} \text{ m}^2 \text{ s}^{-1}$  compared to  $1.5 \times 10^{-9} \text{ m}^2 \text{ s}^{-1}$  in the metal, we investigate into this instability by proposing two test cases: first, we try to limit the solute advection in the transition zone where flow instabilities may form as seen previously in the segregation-free sample but keeping equal solute diffusion coefficients in both domains to  $1.5 \times 10^{-9} \text{ m}^2 \text{ s}^{-1}$ , while for the second test case, we combine both low solute diffusion and low solute advection. The average composition results of these two test cases are respectively plotted in [fig. 5.17b](#) and [fig. 5.17c](#). These results (second plot in [fig. 5.17](#)) clearly show that just by reducing solute advection in the mixing zone reduce the amplitude of the composition instability. In contrast, changing solute diffusion properties for the air coupled with reduced solute advection (third plot in [fig. 5.17](#)) offers no further stability in the segregation profile, which should normally stay below the nominal value near the interface.

## 5.6. 1D application: solidification with inverse segregation

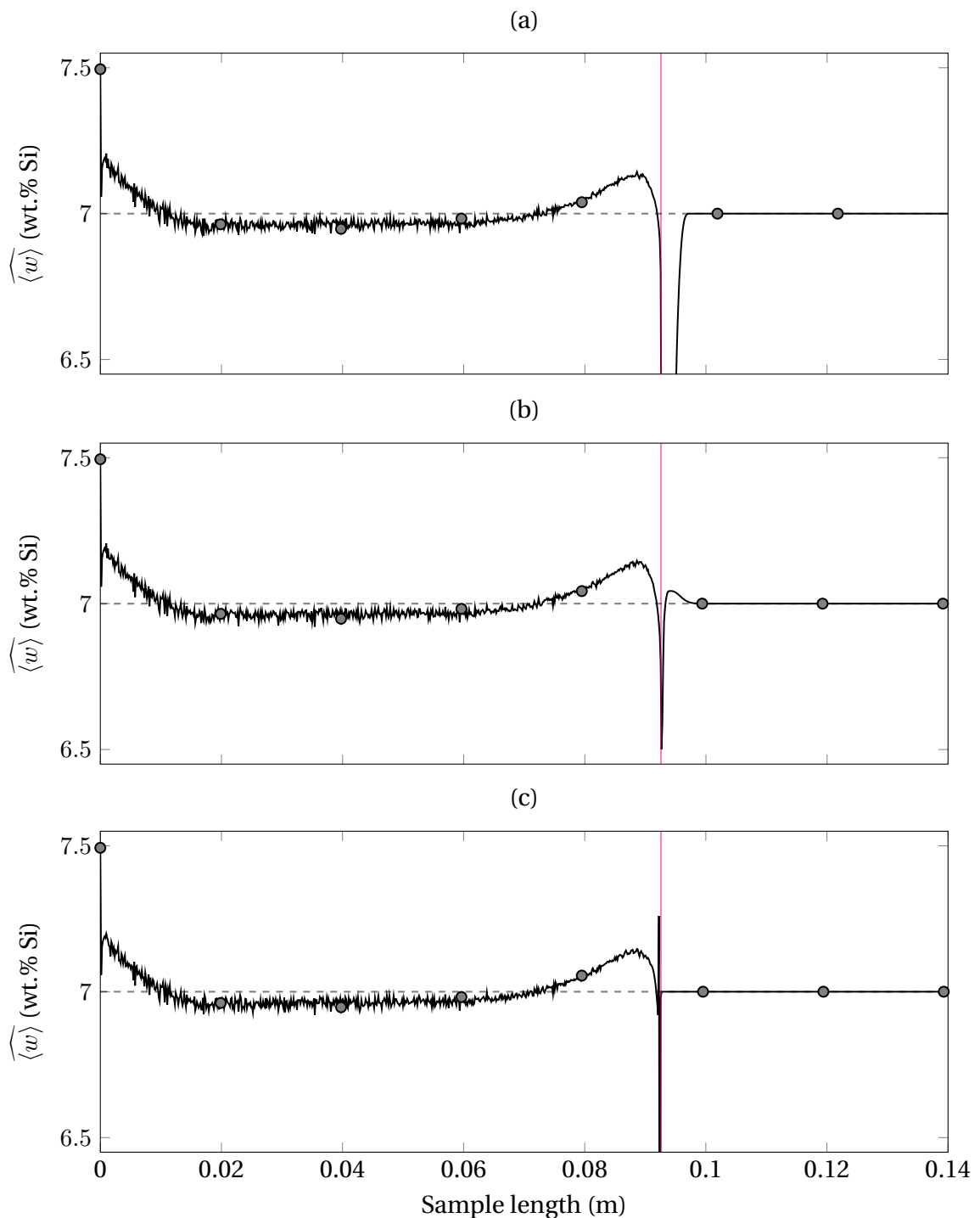


**Fig. 5.17** – Plot of the average composition as function of length, along a vertical line passing through the centre of the sample at 1000 s, with (a) low solute diffusion in the air but unmodified solute advection (minimum composition reaches 2.2 wt.% Si but not shown), (b) reduced solute advection in the level set transition zone or (c) a combination of the previous techniques. The solid magenta line shows the position of the interface after solidification while the black dashed line shows the nominal average composition of the alloy.

## Chapter 5. Macrosegregation with solidification shrinkage

---

**Table 5.1** – Parameters for the 1D inverse segregation test case with a binary Al-7 wt.% Si alloy.

Parameter	Symbol	Value	Unit
Nominal composition	$w_0$	7	wt.%
Liquid density	$\langle \rho \rangle^l$	2600	$\text{kg m}^{-3}$
Solid density	$\langle \rho \rangle^s$	2800	$\text{kg m}^{-3}$
Air density	$\langle \rho \rangle^a$	1.3	$\text{kg m}^{-3}$
Liquid viscosity	$\mu^l$	$10^{-3}$	$\text{Pa s}$
Solid viscosity	$\mu^s$	(Darcy)	$\text{Pa s}$
Air viscosity	$\mu^a$	$10^{-4}$	$\text{Pa s}$
Liquid heat capacity	$C_p^l$	1000	$\text{J kg}^{-1} \text{K}^{-1}$
Solid heat capacity	$C_p^s$	928.57	$\text{J kg}^{-1} \text{K}^{-1}$
Air heat capacity	$C_p^a$	1000	$\text{J kg}^{-1} \text{K}^{-1}$
Enthalpy of fusion	$L$	365 384	$\text{J kg}^{-1}$
Thermal conductivity	$\kappa$	70	$\text{W m}^{-1} \text{K}^{-1}$
Solute diffusion in the liquid	$\langle D \rangle^l$	$10^{-9}$	$\text{m}^2 \text{s}^{-1}$
Solute diffusion in the solid	$\langle D \rangle^s$	0	$\text{m}^2 \text{s}^{-1}$
Solute diffusion in the air	$\langle D \rangle^a$	$10^{-12}$	$\text{m}^2 \text{s}^{-1}$
Heat transfer coefficient	$h_{\text{ext}}$	500	$\text{W m}^{-2} \text{K}^{-1}$
External temperature	$T_{\text{ext}}$	100	$^{\circ}\text{C}$
Initial temperature	$T_0$	800	$^{\circ}\text{C}$
Ingot length		0.1	m
FE mesh size		$10^{-3}$	m
Time step	$\Delta t$	0.1	s
Convergence criterion (residual)	$\varepsilon_R$	$10^{-6}$	—
Convergence criterion (temperature)	$\varepsilon_T$	$10^{-2}$	K

## 5.6. 1D application: solidification with inverse segregation

---

**Table 5.2** – Summary of the mesh parameters used to generate an adaptive anisotropic mesh, along with the level set mixing thickness,  $\varepsilon$ . Refer to [section 2.6.2](#) for the definition of each mesh parameter.

Mesh parameter	Value
$\varepsilon$	$2.5 \times 10^{-4}$ m
$h_n$	$2.5 \times 10^{-5}$ m
$h_\tau$	$2 \times 10^{-4}$ m
$h_M$	$1.5 \times 10^{-4}$ m
$h_A$	$2.5 \times 10^{-4}$ m
Number of nodes	$\approx 7 \times 10^3$
Number of elements	$\approx 1 \times 10^4$

**Table 5.3** – Summary of the comparative shrinkage simulations without macrosegregation.

Case	Air viscosity [Pa s]	Air density [ $\text{kg m}^{-3}$ ]	Time step [s]
R	$10^{-4}$	1.3	0.01
A1	$10^{-3}$	2600	0.01
A2	$10^{-3}$	2600	0.1

**Table 5.4** – Main properties of the linearised phase diagram for Al-Si alloys.

Parameter	Symbol	Value	Unit
Nominal composition	$\langle w \rangle_0$	7	wt.%
Liquidus temperature	$T_l$	618	°C
Eutectic temperature	$T_E$	577	°C
Segregation coefficient	$k$	0.13	–
Liquidus slope	$m_l$	-6.5	K wt.% <sup>-1</sup>

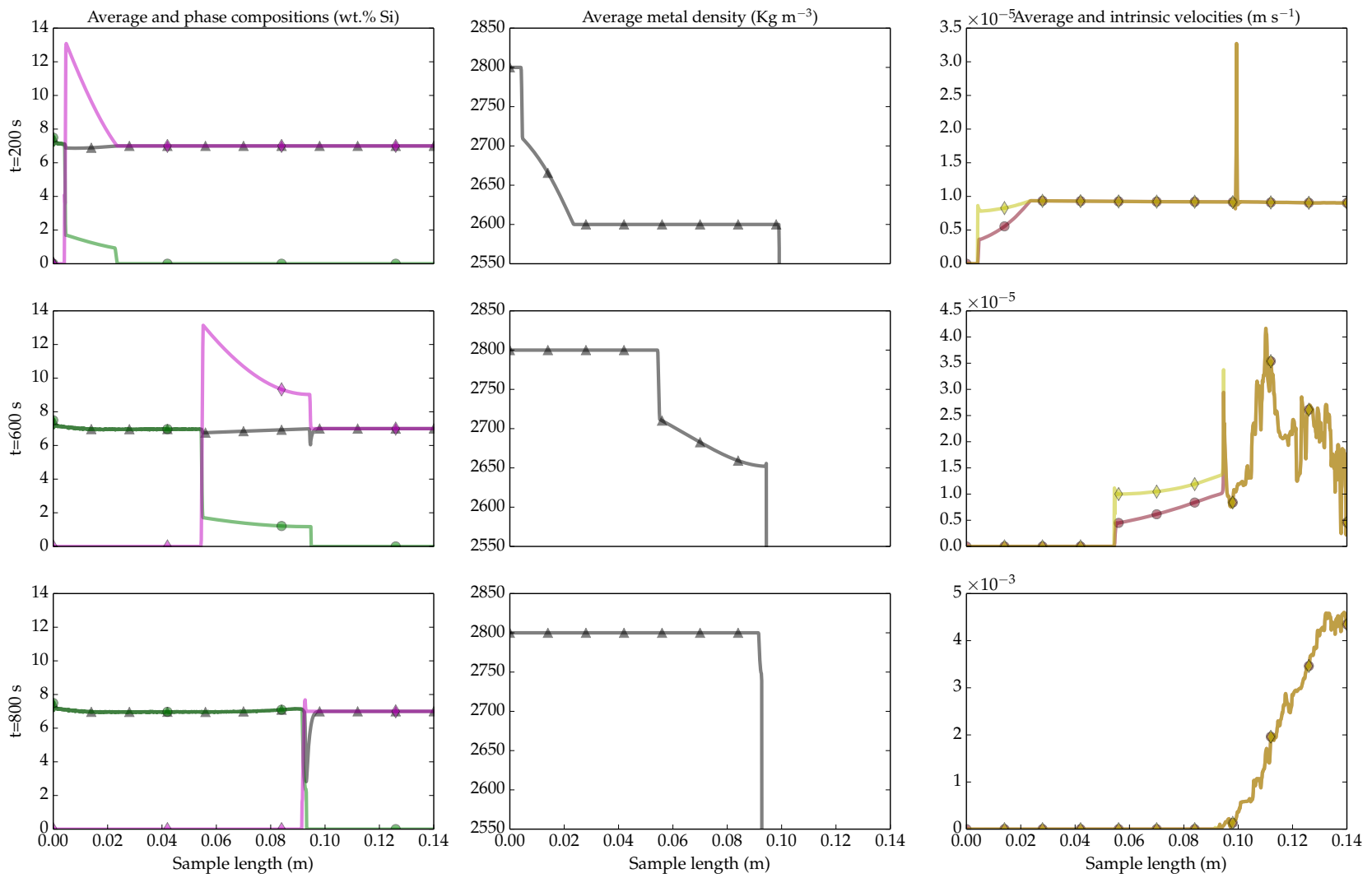


**Fig. 5.18** – Group of plots where each row is a given time increment ( $t=200\text{ s}$ ,  $t=600\text{ s}$  and  $t=800\text{ s}$ ) of the 1D solidification shrinkage simulation with macrosegregation, while each column one or more physical quantities are plotted along a vertical line passing through the centre of the sample. Plots are titled with the corresponding plotted quantities.

## **5.6. 1D application: solidification with inverse segregation**

---

The plots in [fig. 5.18](#) give important information on the segregation shown in [fig. 5.16](#).  
CONTINUE COMMENTING ON [fig. 5.18](#).

### **Solute mass conservation**

Show solute mass conservation with equal or low solute diffusion in air



## 5.7 2D application: controlled solidification benchmark

In this application, we aim at predicting macrosegregation produced by liquid convection, in the presence of solidification shrinkage. A molten alloy is put in a rectangular crucible with controlled cooling flux on one or two sides to the crucible. The importance of the experiment lies in the thermal convection forces arising from temperature gradients, but also solutal buoyancy forces arising from liquid concentration gradients. The final macrosegregation pattern strongly depends on density variations caused by each chemical species, but also on the experimental conditions like the lateral thermal gradients as well the cooling rate, as shown in [fig. 5.19](#). Hebditch and Hunt [1974] suggested one of the first experiments working on Sn-Zn and Sn-Pb alloys. More recently, an experimental benchmark was performed by Hachani et al. [2012] to obtain more accurate composition results with various Sn-Pb and Pb-Sn alloys. In the current section, we are interested in the latter experiment, especially in the prediction of the metal's shrunk surface together with the final macrosegregation.

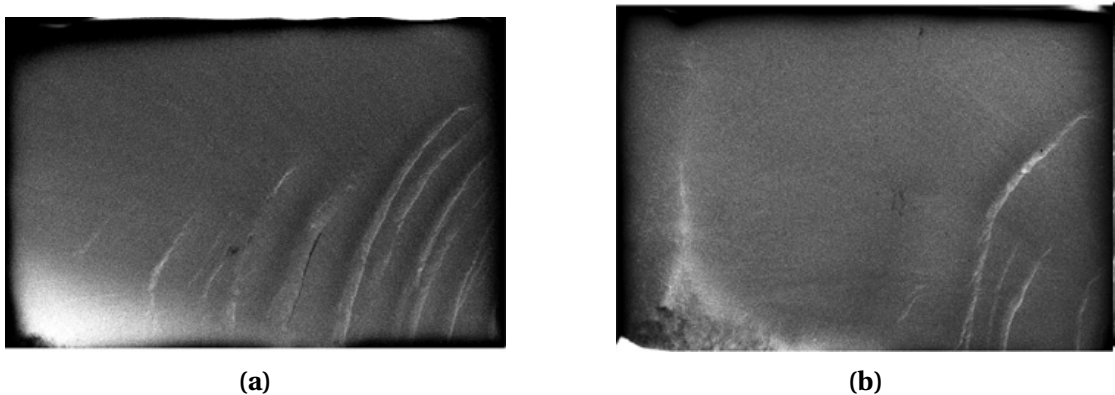


**Fig. 5.19** – Final macrosegregation patterns obtained by solidifying a Sn-3 wt.% Pb alloy at (a)  $0.02 \text{ K s}^{-1}$  and (b)  $0.04 \text{ K s}^{-1}$ . The different cooling rates result in different lead segregation patterns, with a greater number of channel segregates in the latter. The X-rays show also a visible sign of volume shrinkage at the top of each ingot [Hachani et al. 2012].

### 5.7.1 Boundary condition effect

First, we want to understand the consequence of removing the no-slip boundary condition at the *M-A* boundary and compare the effect on macrosegregation. For computations without level set, as previously done in chapter 4 for the *Tsolver*'s validation in convection-diffusion regimes, a no-slip condition was applied for all domain boundaries including the interface. However, this is not readily implemented with the level set method which considers the local interface velocity for its transport. In [figs. 5.20](#)

## Chapter 5. Macrosegregation with solidification shrinkage

---

and 5.21, we compare at 2800 s and 7000 s the differences between a no-slip condition on the top boundary and a free-slip tangential condition, assuming zero normal velocity.

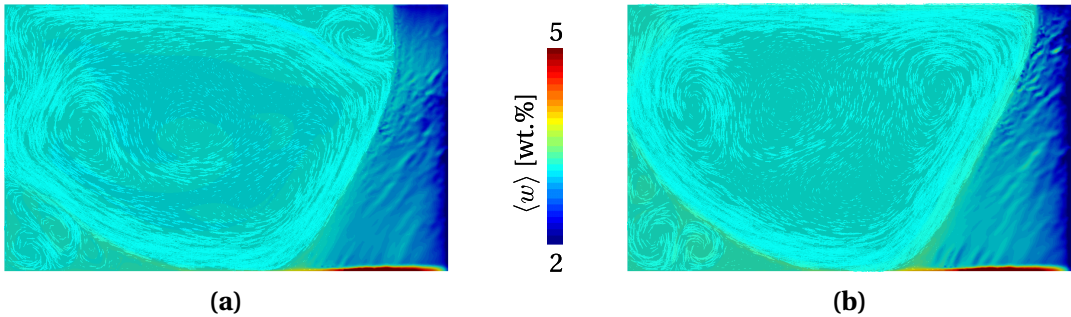


**Fig. 5.20** – Comparison of two solidification with macrosegregation cases assuming (a) a no-slip condition on the upper boundary or (b) a tangential free-slip condition. The snapshots are taken at 2800 s.

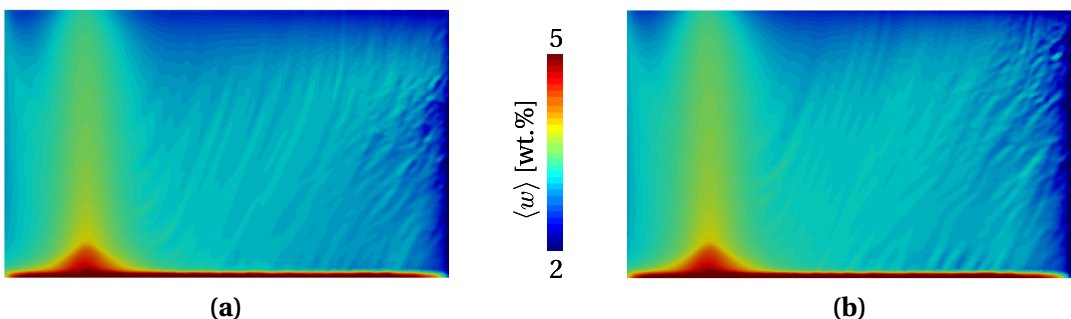


**Fig. 5.21** – Comparison of two solidification with macrosegregation cases assuming (a) a no-slip condition on the upper boundary or (b) a tangential free-slip condition. The snapshots are taken at 7000 s.

In fig. 5.20, solidification is still at an early stage, at 2800 s. The main difference between fig. 5.20a and fig. 5.20b is the flow pattern near the top interface. The no-slip wall acts a brake for the vicinity flow, deviating it downwards and allow a quicker solidification rate for the right upper part of the metal. The flow near the slip wall in fig. 5.20b is not damped and therefore delays solidification of the upper corner where it impinges. The different flow pattern creates a more pronounced negative segregation in the upper right corner of fig. 5.20a, compared to the same location in fig. 5.20b. Later when solidification is complete at 7000 s (fig. 5.21), the overall macrosegregation is more visible: expect for the previously mentioned difference in the corner segregation, no big differences are observed. This means that when using the level set method, allowing the velocity to have non-zero values near the interface should not drastically change the predicted flow pattern and the subsequent macrosegregation.

### 5.7.2 Computational configuration

#### Mesh and adaptive remeshing

The case considers a 2D geometry having equivalent dimensions to the 3D case performed earlier (sample of 10 cm in length and 6 cm in height). To accommodate the air domain, an extra 2 cm are added to sample's height, which finally reaches 8 cm, the interface is thus kept at an elevation of 6 cm. The initial mesh consists of three different mesh sizes: isotropic meshes in the air and the metal, having respectively a uniform size of 2 mm and 1 mm. Regarding the interface, an anisotropic mesh adapts to the *M-A* boundary with a mesh size of 0.1 mm in the normal direction to the interface. The thickness of the anisotropic mesh spans 0.5 mm from each side of the interface. To adapt the mesh, we use the *Remesh4* adaptive technique to maintain accurate predictions for velocity and interface transport. However as solidification proceeds, we also need to keep a relatively small mesh size in regions with noticeable composition gradients. Although this is possible with the *Remesh4* technique, it is more difficult to maintain a fine mesh size throughout the metal, especially in areas where solidification is almost complete and the velocity field has a low magnitude. The consequence is a loss of information when coarser elements are obtained by remeshing.

To avoid such unwanted effects, we use another uniform isotropic grid, named *grid B*, having a constant mesh size of 0.3 mm, that is three times smaller than the interface elements in the original mesh (named *grid A*). The strategy consists of scanning the liquid fraction of each node in *grid A*, if its value is located between 30% and 70%, then we consider that is a region of interest, since the flow velocity is still not zero and a relatively fine mesh is locally obtained. We consequently transport the average composition field exclusively for these nodes from *grid A* to *grid B*, keeping for all other nodes their respective average composition values. It should be noted that this transport is only one-way, hence no information feedback from *grid B* to *grid A*.

#### Initial and boundary conditions

The air initial temperature is the same as the initial liquid. This is only a hypothesis to prevent steep temperature gradients at the interface, which may lead to surface solidification. The initial and boundary thermal conditions used to cool down the metal are defined in chapter 4, given by the experimental data of Hachani et al. [2012]. For the mechanical properties, the top wall allows free inflow/outflow of the air in all directions at an imposed atmospheric pressure. This allows the air to follow any volume changes in the metal upon solidifying and shrinking.

The side walls adjacent to the heat exchangers are given a free tangential slip boundary

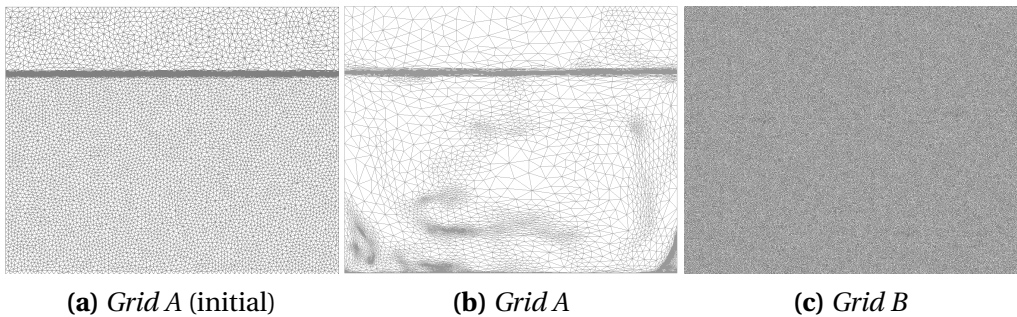


**Fig. 5.22** – Snapshots of (a) the initial adaptive anisotropic *grid A* then (b) the same grid but at a given time increment with (c) the corresponding fixed isotropic *grid B* at the same time increment.

condition but with a zero normal velocity, which lets the transported level set function move vertically without being attached to the sides. Finally, a no-slip condition applies to the bottom wall.

### 5.7.3 Results

The results are recorded at two intermediate solidification stages, at 3050 s and 3550 s, knowing that solidification onset is around 1920 s. First, we look to the results in [fig. 5.23](#). The original average composition field obtained by *grid A*, shown in [fig. 5.23a](#), is almost free of composition gradients except for one segregated channel rising from the bottom by the action of thermal convection. On the other hand, the average composition transport from the adaptive grid to the fixed one, allows recording macrosegregation onto the latter at nodes where the solid exceeds 0.7 in volume fraction, depicted by the yellow region in [fig. 5.23c](#). This is why we observe in [fig. 5.23b](#) a number of channel segregates which are slightly below nominal composition but still richer in lead species with respect to the surrounding solid. The solid fraction distribution is shown in [fig. 5.23d](#), along with the flow pattern. Local vortices are observed in the metal, probably due to considering only a 2D geometry instead of the complete 3D, and this alters the computation stability by ignoring the boundary layers in the sample thickness, obtained otherwise in 3D. Nevertheless, the overall flow is driven by a thermosolutal driving force, with a compatible flow in the air side. We can observe how the solid fraction is modified in the segregated channel, as a result of macrosegregation. At this stage of solidification, the interface movement is still difficult to see, but 500 s later it becomes more visible.

We are now at 3550 s, and the decreasing left heat exchanger temperature has just gone below the local liquidus, triggering solidification from the left side. The average composition field presents noticeable differences between the adaptive *grid A* and

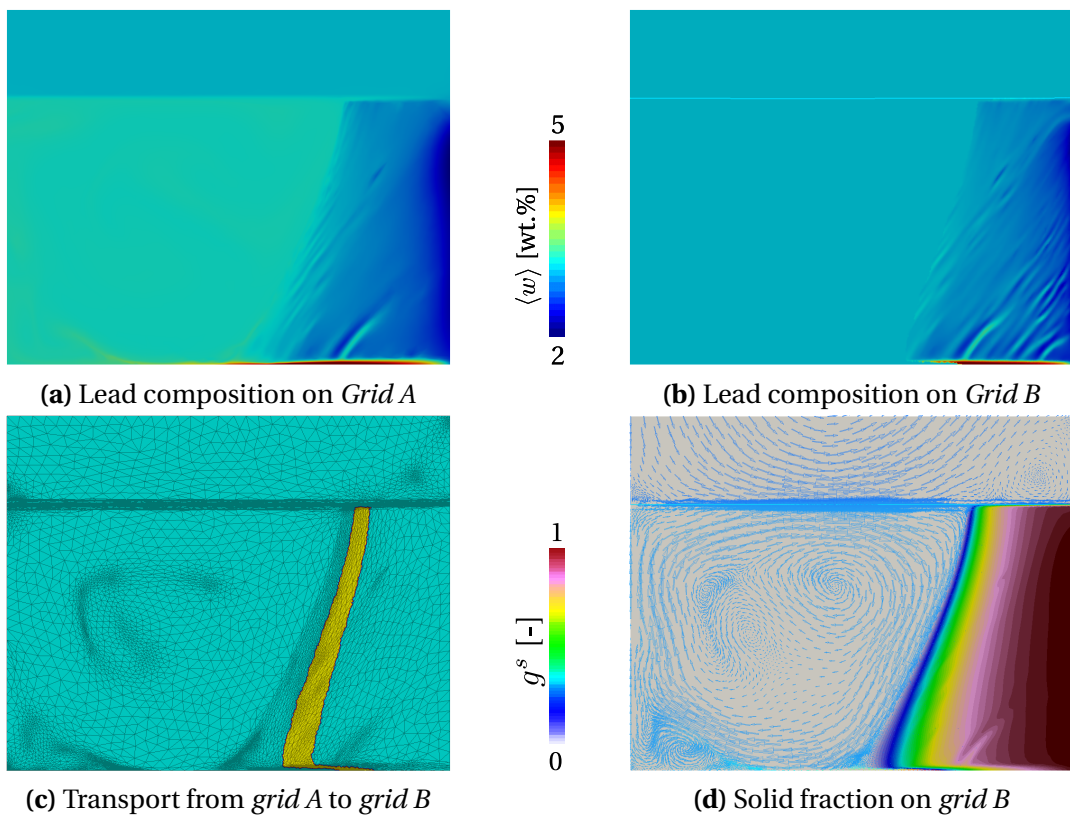


**Fig. 5.23** – Snapshots at 3050 s of the average composition field shown on (a) *grid A* where the mesh gets coarser in fully solidified regions near the right side while and then on (b) *grid B* where the uniform fine mesh predicts a smoother composition field (line indicates the current interface level). The increased number of segregated channels on the right side of the metal is obtained by the successive transport operations performed in (c) a restricted area (yellow color) based on the nodal values of (d) the solid fraction field.

the fixed *grid B*. The weak macrosegregation observed in [fig. 5.23a](#) are now lost in [fig. 5.24a](#), as the mesh got coarser on the metal's solidified right side. Fortunately, the macrosegregation distribution is stored in the fixed grid ([fig. 5.24b](#)) and shows more details with the advancement of solidification. The shrinkage due to phase density difference, is now clearly visible judging from interface shape, which still almost planar above the last liquid pool.

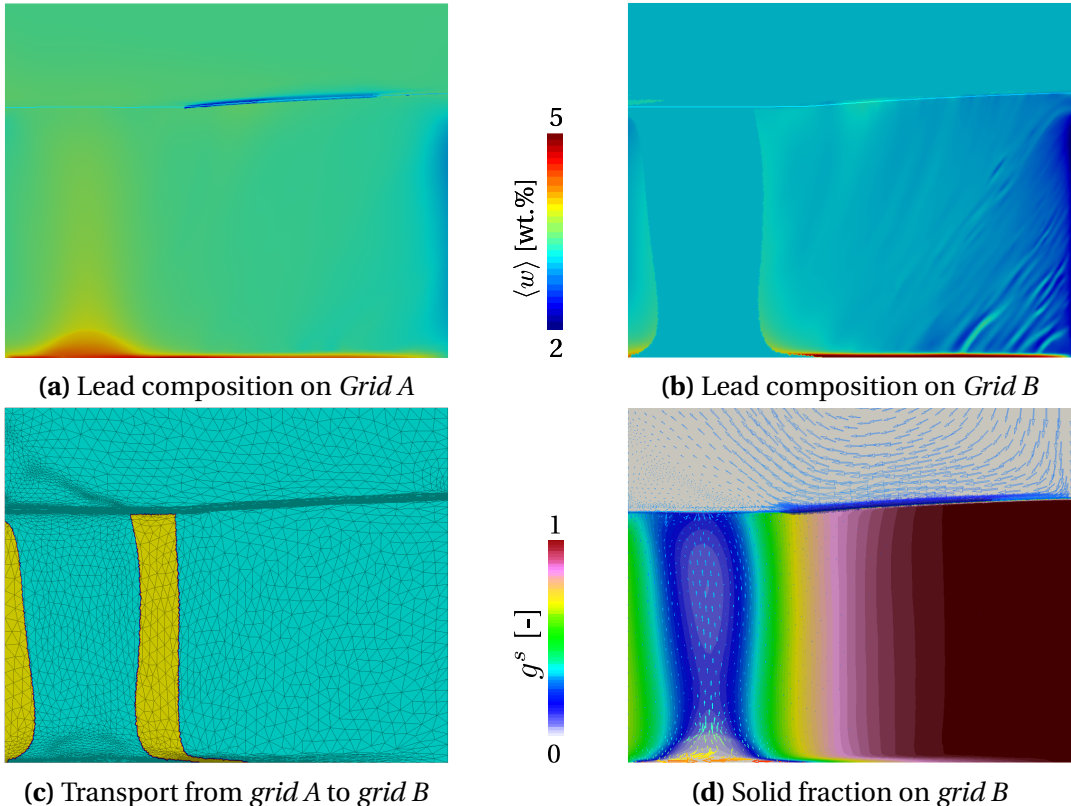


**Fig. 5.24** – Snapshots at 3550 s of (a) the average composition result obtained on *grid A*, compared to (b) the composition field obtained on *grid B*, (c) the after being transported in (c) a restricted area (yellow color) based on the nodal values of (d) the solid fraction field.

## **5.7. 2D application: controlled solidification benchmark**

---

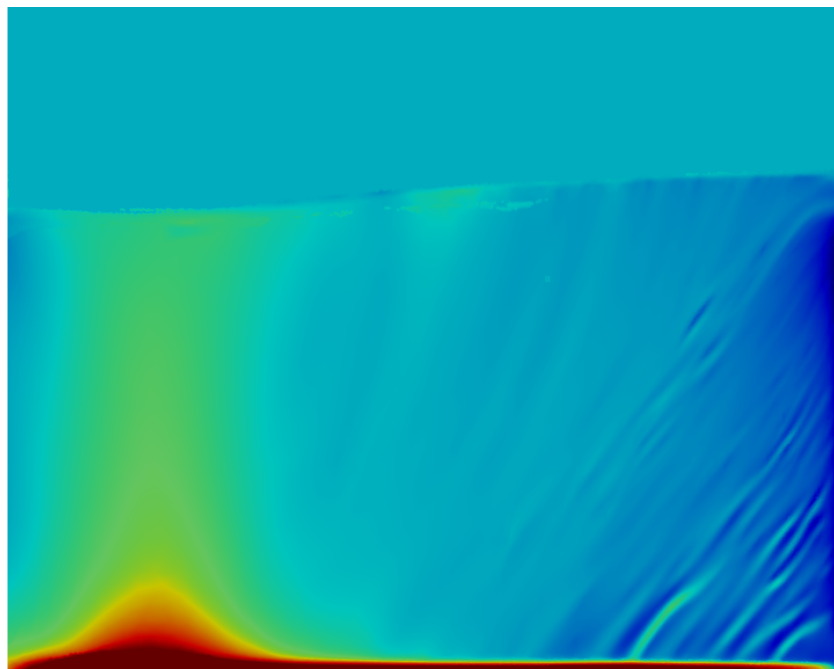


**Fig. 5.25 – blabl**



## 5.8 3D application: reduced-gravity solidification

As presented in the introductory chapter, the aim of the CCEMLCC project is to "reach a better understanding of surface defects formed during processing of steels from the liquid state" [Gandin 2014]. Among the several scientific topics being studied, the interaction between skin macrosegregation and thermomechanical deformation is investigated through chill cooling experiments. The idea is to have the molten steel in a containerless environment, which could be done by several ways: electromagnetic levitation, on-board parabolic flights or sounding rockets and finally in a real microgravity context as in the ISS. Heat is extracted from the sample by contact with a ceramic ( $\text{Si}_3\text{N}_4$ ) substrate at room temperature (hence the term "chill cooling"), that collides into the alloy at a controlled speed. This contact situation generating a high thermal gradient is comparable to casting processes between the molten alloy and the moulds. For ground-based experiments, EML was used to achieve chill cooling of samples without using moulds. However, levitation induces currents in the spherical sample, generated by means of electromagnetic stirring (Lorentz forces) but also by thermal and solutal convection on the other hand. In reduced-gravity conditions, the dynamics of the phenomena behind fluid motion are less significant. The current modelling is therefore compared to chill cooling experiments performed in parabolic flights and sounding rockets with reduced gravitational forces ( $\|g\| \in [10^{-5}; 10^{-1}] \text{ m s}^{-2}$ ).

### 5.8.1 Previous work

#### TEMPUS experiment for parabolic flight campaigns

The TEMPUS experiment came as a first alternative for EML experiments on ground during which accurate thermophysical and rheological characterisation were difficult to achieve. Each flight consists of several cycles of free fall, a reduced-gravity environment is hence created, allowing to use only a single radiofrequency (RF) coil to stabilise the position of the droplet, while the substrate comes into contact with the molten sample from above it. An axial pyrometer measures the sample temperature during the process. Also, a high-speed camera records the solidification process, producing frames as shown in [fig. 5.27](#). This is useful to measure the front growth speed. Each parabola cycle lasts for 50 s, offering an effective low gravity ( $\|g\| \approx 10^{-1} \text{ m s}^{-2}$ ) for about 20 s.

### TEXUS sounding rocket

TEXUS-46 is the name of the sounding rocket mission that carries the experimental setup, but for simplicity we will refer to the latter as being the TEXUS experiment. The setup is shown in [fig. 5.26](#). The main difference with respect to parabolic flight experiments, TEXUS features solidification in near-zero gravitational fields and for extended periods of time (3 minutes). We do not have an exact measurement of the gravitational field magnitude, but it is several orders less than Earth's gravity magnitude ( $\|g\| \in [10^{-5}; 10^{-8}] \text{ m s}^{-2}$ ). It should be mentioned that the experimental setup is comparable between parabolic flights and sounding rocket experiments. That is to say that the dimensions of the steel sample, the substrate and the container are almost the same. Nevertheless, different steel compositions were considered in each type of experiment.

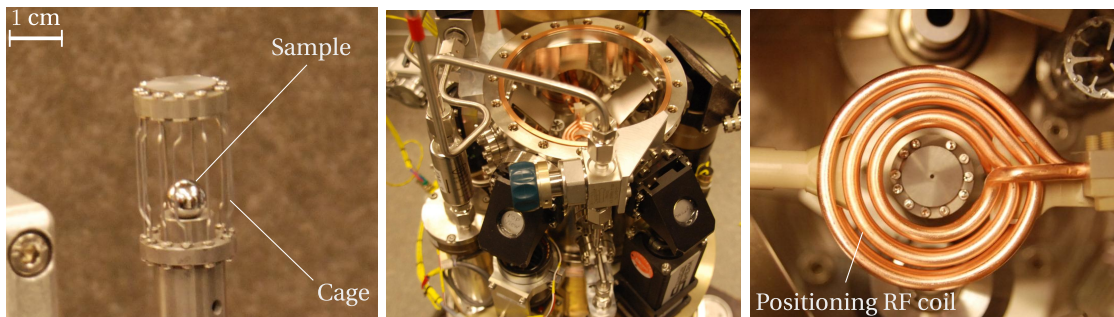


**Fig. 5.26** – Three frames describing the experimental setup used to achieve reduced-gravity solidification on-board a sounding rocket flight, showing the initial alloy sample, the cage and the positioning coil. The setup is similar to the one used for TEMPUS experiments.

### Numerical contribution

A former numerical contribution was done by [Rivaux \[2011\]](#) at CEMEF as mentioned in the first chapter. His model considered both the steel droplet and the ceramic chill in a Lagrangian formulation, i.e. each object is modelled using a separate mesh. Conservation equations of mass, energy, chemical species and momentum were solved in the metal domain, while the energy conservation was the sole equation solved on the chill mesh. The mechanical problem was divided into two parts: fluid mechanics and solid mechanics. For the first part, the momentum conservation in the liquid phase was solved using an incompressible P1/P1 SUPG-PSPG formulation of Navier-Stokes equations, i.e. without any contraction for the liquid phase neither solidification shrinkage at the solid-liquid interface. The second part, solid mechanics,

## 5.8. 3D application: reduced-gravity solidification

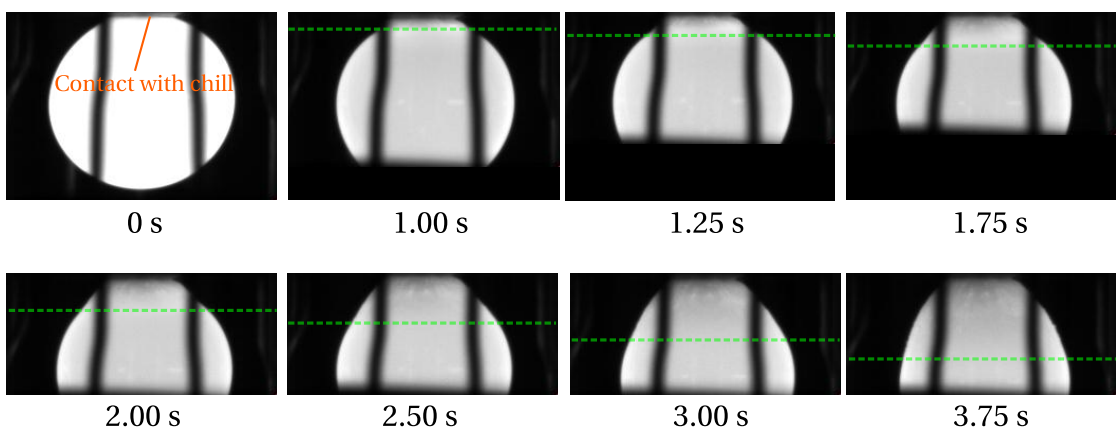


**Fig. 5.27** – Image sequence given by a high speed camera on-board a TEMPUS parabolic flight (parabola #14 Oct 2014), showing the solidification progress between 0 s (when contact with the chill is initiated) to 3.75 s in a Fe-0.9 wt.% C-0.2 wt.% Si steel droplet. The progress of the solidification front is marked by the green dashed line. In some frames, the droplet is partially hidden by the narrow opening of the sample holder facing the camera.

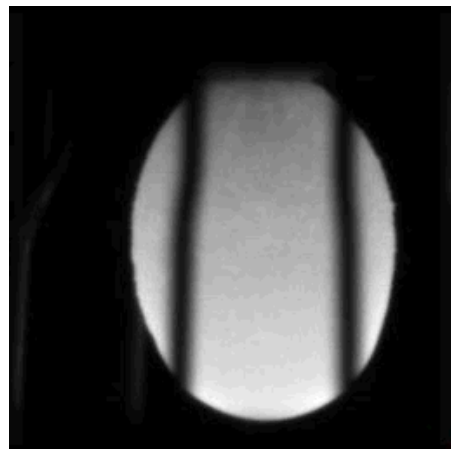


**Fig. 5.28** – Camera image from the TEMPUS 2014 experiment, showing the fully solidified droplet with a deformed shape after 10 s.

was solved using P1+/P1 formulation to predict solid deformation caused by the solid's thermal contraction as well as solidification shrinkage, using an elastic-viscoplastic behaviour.

The simulation results showed that the total droplet deformation that has been observed in the experiments is not primarily due to solid deformation. The density jump between the solid and liquid phases at the solidification front is actually predominant. High speed camera images shown in [figs. 5.27](#) and [5.28](#) endorse this observation, where the droplet underwent a continuous spherical-to-elliptic shape change while the solidification front travelled away from the contact point. Another interesting point to comment is the computation of solidification shrinkage in the solid resolution, although this type of shrinkage does not generate stresses in the solidifying alloy, compared to thermal contraction for instance.

Thermal contraction and strains in the solid phase were computed and coupled with fluid mechanics but hardly managed to retrieve the final shape of the droplet reported in the experiment, as revealed in [fig. 5.27](#).

### 5.8.2 Computational configuration

#### Geometry and mesh

The simulation considers only 1/4 of the droplet-gas system, given the axial symmetry of the problem. Furthermore, the substrate is implicitly taken into account via a boundary condition, as explained in the next section. This is sufficient in the current context, because we are only interested in the energy transfer from the droplet to the substrate.

The steel sample is not perfectly spherical initially as surface oscillations perturb the equilibrium shape. Such perturbations may be attributed to Lorentz forces created by the positioning coil. The droplet hence is compared to an ellipsoid having a vertical minor axis of 5.68 mm and a horizontal major axis of 6.6 mm [[Rivaux 2011](#)], as shown in [fig. 5.29](#). The top is a planar surface (diameter of 2 mm), where the contact is initiated. Also in [fig. 5.29](#), the alloy is immersed in a gas medium (argon), such that both domains form together 1/4 of a cylinder having 8 mm in radius and 8 mm in height.

The mesh is then automatically adapted to the moving interface using *Remesh2*. We adopt the same remeshing strategy applied for computations shown in [figs. 5.10b](#) and [5.11b](#), whereby a fixed mesh size,  $h_M$ , is imposed in the metal domain, another fixed size,  $h_A$ , for the argon domain, while the interface is remeshed using anisotropic elements. All remeshing parameters are found in [table 5.5](#). The corresponding parameters are given by [table 5.5](#). Remeshing is performed each second.

## 5.8. 3D application: reduced-gravity solidification

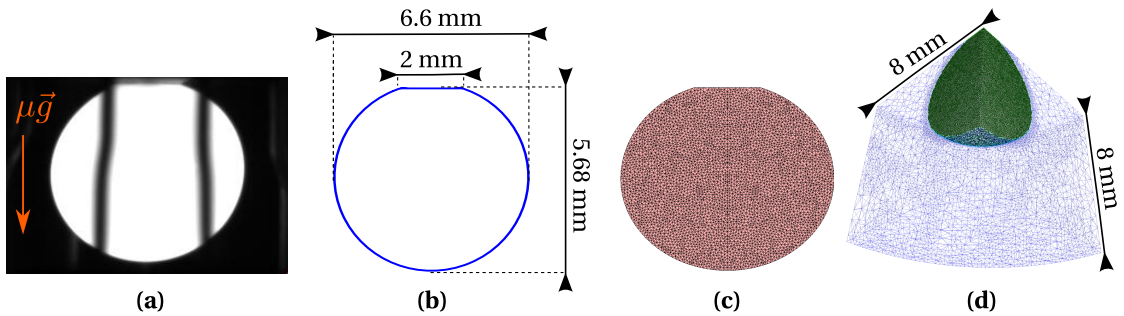


**Fig. 5.29** – (a) The camera frame before the onset of solidification gives the essential information to (b) rebuild the droplet geometry then (c) a standalone 2D mesh used to obtain (d) the final immersed 3D mesh corresponding to time 0 s in [fig. 5.27](#).

**Table 5.5** – Summary of the mesh parameters used to generate an adaptive mesh, along with the level mixing thickness,  $\varepsilon$ . Refer to [section 2.6.2](#) for the definition of each mesh parameter.

Mesh parameter	Value
$\varepsilon$	$1.5 \times 10^{-4}$ m
$h_n = h_\tau$	$2 \times 10^{-5}$ m
$h_M$	$1 \times 10^{-4}$ m
$h_A$	$6 \times 10^{-4}$ m
Remeshing frequency	1 s
Number of nodes	$\approx 1 \times 10^5$
Number of elements	$\approx 5 \times 10^5$

### Initial and boundary conditions

The thermal boundary conditions are set as follows: heat loss by radiation is experimentally avoided, therefore it is not considered in our model, hence all boundaries are considered adiabatic, except for the metal-substrate contact area, as previously mentioned. This surface is modelled by a Fourier condition with  $T_{\text{ext}}=25\text{ }^{\circ}\text{C}$  and an effective exchange coefficient  $h_{\text{ext}}$  of  $6 \times 10^4 \text{ W m}^{-2} \text{ K}^{-1}$ . The  $h_{\text{ext}}$  coefficient's value has been determined by running multiple simulations with different values in the aim of predicting a front speed as closer as possible to the experimental measurements plotted in [fig. 5.30](#), as explained in the coming sections.

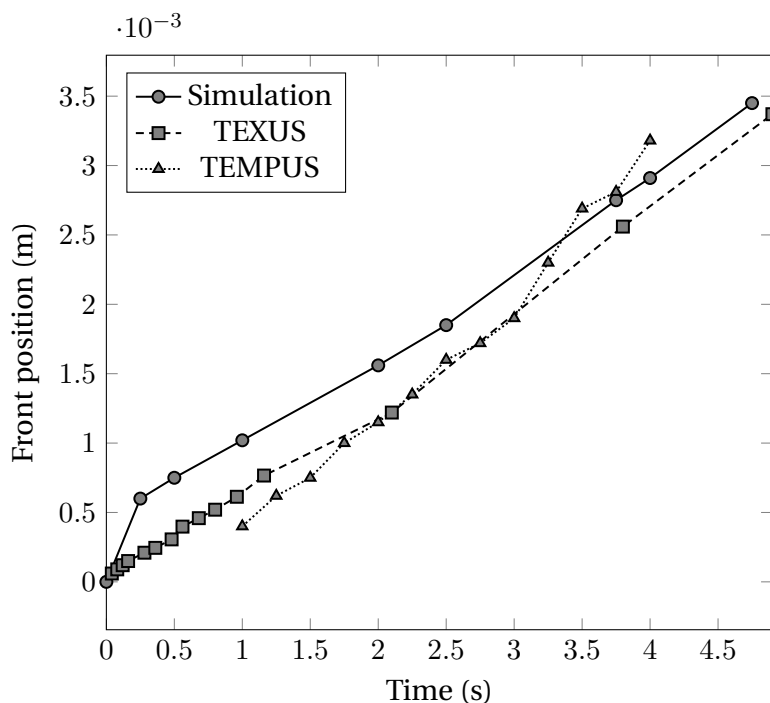


**Fig. 5.30** – Position of solidification front versus time for the binary alloy simulation compared to the experimental findings of the TEXUS-46 flight in 2009 and TEMPUS 2014 measurements [[Gandin 2014](#)].

For the velocity-pressure boundary conditions, [fig. 5.31](#) shows that a no-slip condition is imposed on the droplet-substrate surface, since this area solidifies first without further fluid motion, as shows [fig. 5.27](#). It is noted that the first solidified shell may experimentally deform under thermal contraction stresses, but we do not consider it hereafter, unlike what was done by [Rivaux \[2011\]](#). For the rest of the domain, we impose the normal velocity component to zero on both symmetry faces, while keeping free tangential components. The remaining boundaries, namely the top and the outer lateral surface of the argon gas, have free velocity components. However, such

condition may cause instability in the level set transport solver. This problem has been reported by [Basset 2006], showing a limitation in the imposed boundary conditions between Navier-Stokes solver and level set transport. Therefore, we limit these instabilities by imposing a no-slip condition, thus allowing the argon to flow in the computational domain through the outer lateral surface. The cylinder height was taken big enough to prevent any flow damping near the droplet's north pole, which may spuriously alter its final shape. The pressure condition for the argon gas is left free for all boundaries. The adopted time step is 0.01 s.

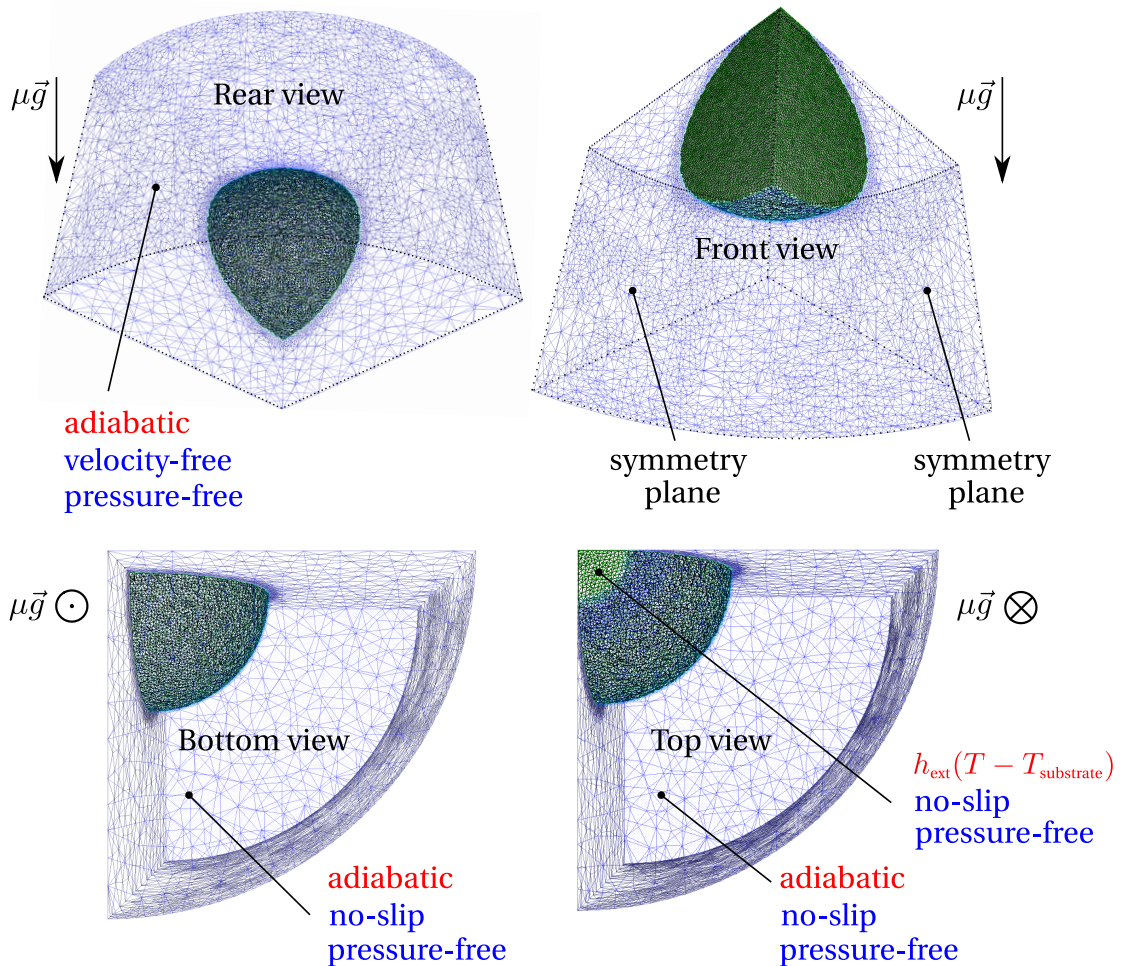


**Fig. 5.31** – 3D views showing the thermal (in red) and mechanical (in blue) boundary conditions used in reduced-gravity simulations. The symmetry planes represent the following set of boundary conditions: adiabatic, zero normal velocity, free tangential velocity and pressure-free.

## Chapter 5. Macrosegregation with solidification shrinkage

---

### Choice of alloy

Various steel grades were considered in the CCEMLCC project, depending on whether the considered alloy will be used for parabolic flights or sounding rocket missions. A medium-carbon steel, Fe-0.9 wt.% C-0.2 wt.% Si, was selected for TEMPUS parabolic flights. For TEXUS missions, the sample is a low-carbon steel and the grade is designated as "*b1*" alloy. Its nominal composition is given in [table 5.6](#).

As our approach relies on thermodynamic tabulations, we show in the next section that we can take into account the multicomponent alloy to predict segregation, by considering first only one species, hence a binary Fe-C alloy, referred to as *b1Bin* alloy. In a later step, we consider a ternary Fe-C-Si alloy, *b1Tern*. Finally, we consider a quaternary Fe-C-Mn-Si alloy, *b1Quat*.

By performing the same reduced-gravity simulation while varying the alloy from binary to quaternary, we can study how the varying solidification paths (as a consequence of macrosegregation) may affect the final droplet shape, as the shrinkage profile is directly related to the solid fraction and its evolution with time.

**Table 5.6** – Nominal composition (wt.%) of the experimental *b1* steel and its binary, ternary and quaternary alloys approximations, respectively *b1Bin*, *b1Tern* and *b1Quat*.

Alloy	C	Si	Mn	Al	S	P
<i>b1</i>	0.105	0.268	0.636	0.0067	0.009	0.0189
<i>b1Bin</i>	0.105	-	-	-	-	-
<i>b1Tern</i>	0.105	0.268	-	-	-	-
<i>b1Quat</i>	0.105	0.268	0.636	-	-	-

### Parametric study: final shape prediction

In this subsection, we focus on obtaining a comparable final shape of the droplet between the experiment and simulation. To do so, we study the variations of 2 main important parameters: first, the heat transfer coefficient of the metal-substrate contact surface that controls the heat extraction and hence the solidification rate. The second parameter is the magnitude of the gravitational field, which has a great influence on the fluid flow inside the molten droplet. The importance of this parametric study is two-fold:

1. in our model, the energy equation solved with the level set methodology considers only heat conduction and advection in the gas A, hence no account for the heat dissipated by radiation. Therefore a trial-and-error strategy is necessary.

sary to determine an optimal value of  $h_{\text{ext}}$  to ensure that the solidification rate is comparable to the experimental measurements,

2. from a hydrodynamics perspective, a containerless molten droplet levitated under reduced-gravity conditions is maintained nearly spherical under the action of surface tension forces. Other forces due to tangential surface tension gradients (Marangoni force) or Lorentz force may also exist. Although possible to implement by the CSF method, accounting numerically for surface tension adds complexity to the model by imposing a time step constraint. However, if we neglect this force, the droplet will tend to collapse if gravity acceleration is fast enough. Consequently, a parametric study helps us determine this gravity threshold, while neglecting surface tension and Lorentz forces.

A series of test simulations were launched in the aim of getting comparable results with the experiment. Several values of  $h_{\text{ext}}$  were tested in the interval  $[10^2; 10^6] \text{ W m}^{-2} \text{ K}^{-1}$ , while the gravity acceleration influence was tested for values lying in the interval  $[10^{-6}; 10^{-2}] \text{ m s}^{-2}$ . The best match for the final shape while preserving a front propagation speed close to  $0.7 \text{ mm s}^{-1}$ , was obtained by setting simultaneously  $h_{\text{ext}} = 6 \times 10^4 \text{ W m}^{-2} \text{ K}^{-1}$  and  $\|g\| = 5 \times 10^{-5} \text{ m s}^{-2}$ . To demonstrate the effect of varying these parameters, we present a parametric study in [table 5.7](#), where only the most relevant cases are studied with a binary alloy, Fe-0.105 wt.% C.

**Table 5.7** – Summary of the parametric study for the conductive heat transfer coefficient ( $H$ ) and the magnitude of the gravity vector ( $G$ , not to be confused with thermal gradient). The cases are defined by fixing each parameter to a reference value then varying the latter parameter. The reference values,  $H_0=6 \times 10^4 \text{ W m}^{-2} \text{ K}^{-1}$  and  $G_0=5 \times 10^{-5} \text{ m s}^{-2}$ , ensure a good compromise when compared to the experimental solidification rate and final droplet shape.

<b>Case</b>	$h_{\text{ext}} [\text{W m}^{-2} \text{ K}^{-1}]$	$\ g\  [\text{m s}^{-2}]$
H1G0	$10^3$	$5 \times 10^{-5}$
H2G0	$10^4$	$5 \times 10^{-5}$
H3G0	$10^5$	$5 \times 10^{-5}$
H4G0	$10^6$	$5 \times 10^{-5}$
H0G1	$6 \times 10^4$	$10^{-3}$
H0G2	$6 \times 10^4$	$10^{-4}$
H0G3	$6 \times 10^4$	$10^{-5}$
H0G4	$6 \times 10^4$	$10^{-6}$

We start the analysis by observing the results in [fig. 5.33](#), where the parameter  $h_{\text{ext}}$  increases from case H1G0 to H4G0, while maintaining a constant gravity acceleration at  $5 \times 10^{-5} \text{ m s}^{-2}$ . In the first case, H1G0, the heat coefficient is at its lowest between

## Chapter 5. Macrosegregation with solidification shrinkage

---

the droplet and the chill. As this contact is the only way to dissipate heat from the droplet, a low heat exchange coefficient means a slow cooling. Therefore, contact area of the droplet solidifies first. As we consider a fixed solid in our model, any solidified part can no longer move or deform. As time passes, solidification is slow, such that the droplet starts collapsing at about 10 sec, undergoing a significant shape change under the gravity's action. It is not clear if such microgravity conditions are sufficient to deform the droplet as simulated in case H1G0. In fact, surface tension forces might play a central role in stabilising the sample shape by minimising its surface energy. As we neglect it in our simulations, the droplet naturally deforms in the direction of the gravity vector. We can make the same conclusion for case H2G0, while taking note of a thicker solid shell base in the horizontal direction, featuring also necking around the droplet axis mid-height. It should be noted that in both cases H1G0 and H2G0, solidification is not complete at 15 s.

More interesting results are obtained in case H3G0 where the heat coefficient is two orders of magnitude higher than that in the first case. The high solidification rate allows the mushy front to propagate further before deformation occurs by gravity. We see a global deformation which is qualitatively comparable to the experimental results: an ellipsoidal form with a longer vertical axis (i.e. in the direction of the microgravity vector) with respect to the initial shape, while the horizontal axis decreases compared to the original sample diameter. Finally, we observe the same deformation tendency if we compare cases H3G0 and H4G0. The latter becomes closer to a situation of pure shrinkage flow. Consequently, its final shape corresponds to a global shrinkage of the initial one.

In order to have a clear idea on the effect of varying the cooling rate parameter on mass conservation, we plot in [fig. 5.32a](#) the mass variation versus time for all four cases. We can notice that mass variation for case H4G0 occurs between 2% and -1% near the solidification end, recording the least variations compared to other cases. On the other hand, cases H1G0 and H2G0 show an important mass loss before solidification comes to end, reaching -11%. We are particularly interested in case H3G0, which shows a good compromise between the deformation magnitude and mass loss, the latter being at -3% of mass metal.

Now, we study the effect of varying the gravity parameter and its influence on the final deformation. We observe first the results for case H0G1 where gravity magnitude is about four orders less than the Earth gravity at zero altitude. While the base solidifies, the remaining part falls down deforming severely by its weight and leading to a non-converging level set transport. The last recorded time is 1.75 s. For case H0G2, the droplet is less solicited by its weight, and therefore solidifies while having a ver-

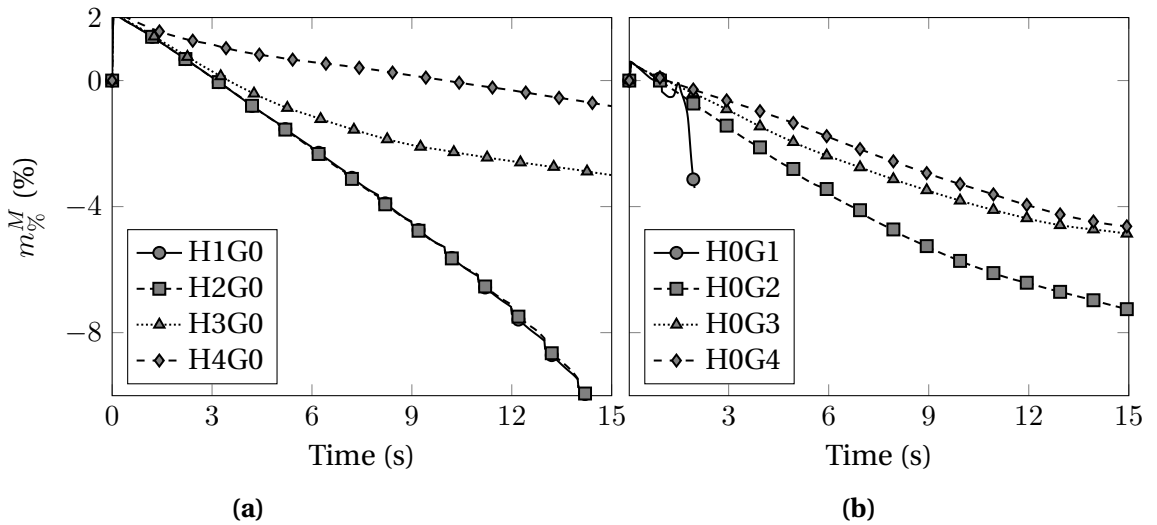


**Fig. 5.32** – Mass conservation analysis for (a) cases HxG0 ( $x=1,2,3,4$ ) and (b) cases H0Gx ( $x=1,2,3,4$ ).

tically elongated shape. It should be reminded that in the current global numerical model does not account for the metal's surface tension, which may clearly have a drastic influence on the final shape, especially at higher gravity magnitudes, such as for cases H0G1 and H0G2. Moving on to cases H0G3 and H0G4, the weight driving force becomes negligible compared to the shrinkage driving force. Therefore, the sample shows significant lateral deformation, while in the central vertical plane of the droplet, the droplet has shrunk when compared to the initial profile. This is more visible in case H0G4, where the final shape is overall smaller than the initial volume, which is not the same as found in cases H3G0 and H4G0. The mass conservation analysis corresponding to the gravity magnitude variation are plotted in [fig. 5.32b](#). The plots show, as expected, better mass conservation for decreasing gravity acceleration, i.e. from case H0G1 to H0G4. We think however that surface tension would change this analysis, and non-convergence obtained in case H0G1 may be prevented.

### 5.8.3 Texus binary alloy

The optimal computational configuration is now known, thus we proceed to simulate the solidification of the binary alloy given previously in [table 5.6](#), using the simulation parameters defined in [table 5.8](#).

The nominal composition for this alloy is Fe-0.105 wt.% C. In order to obtain accurate segregation results, a fine resolution mapping was performed from equilibrium calculations, using 20 values of composition between a minimum of 0.01 wt.% and 1 wt.%. This is equivalent for a composition step of 0.0495 wt.%, with a temperature step of

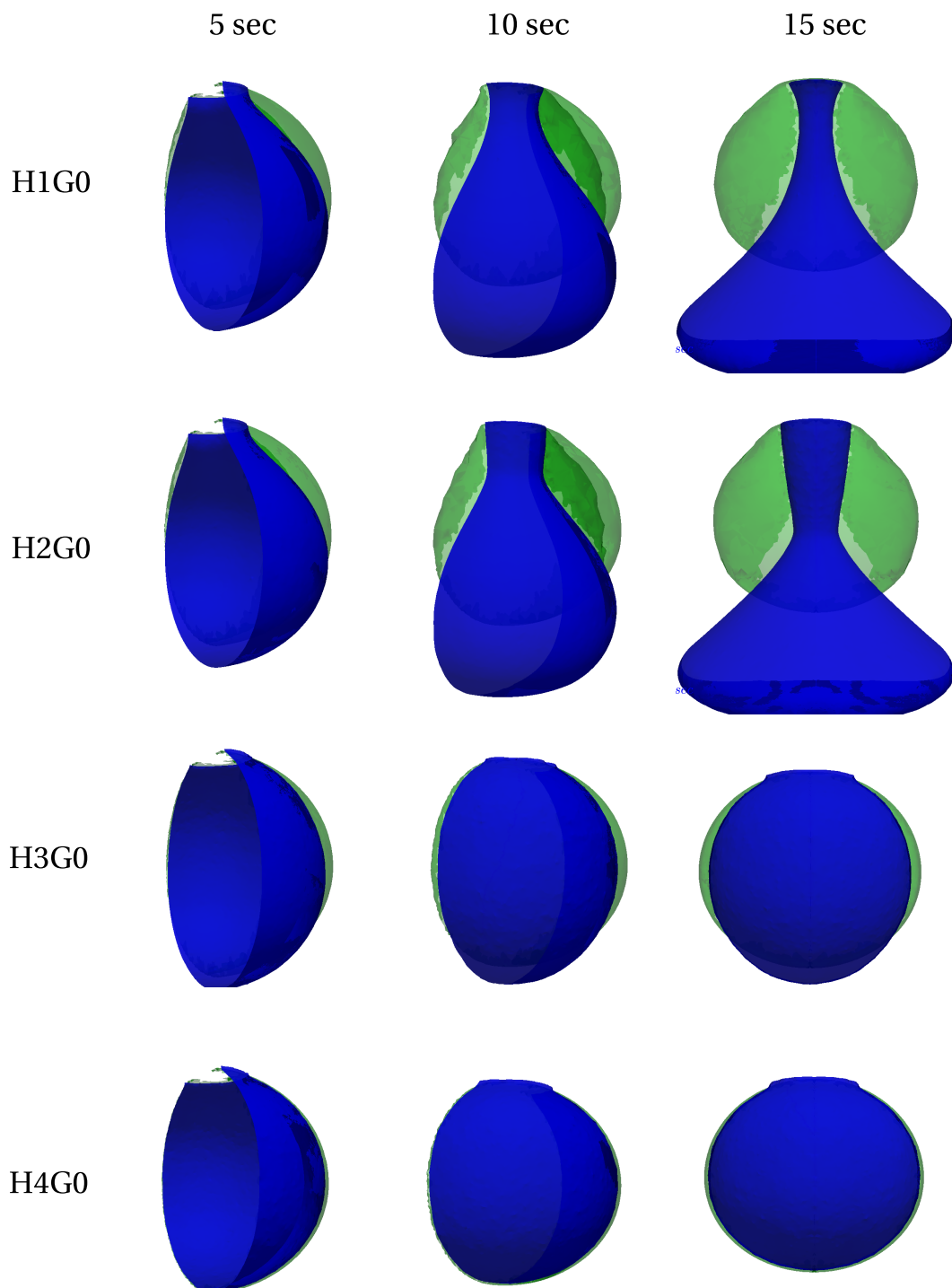


**Fig. 5.33** – 3D snapshots of a droplet (only half shown for symmetry) undergoing solidification shrinkage where the heat exchange coefficient increases from H1 to H4 according to [table 5.7](#). The green surface is the initial droplet profile while the blue surface is the deforming droplet profile. The camera rotation over time allows observing deformation from different angles. The gravity vector points downwards.

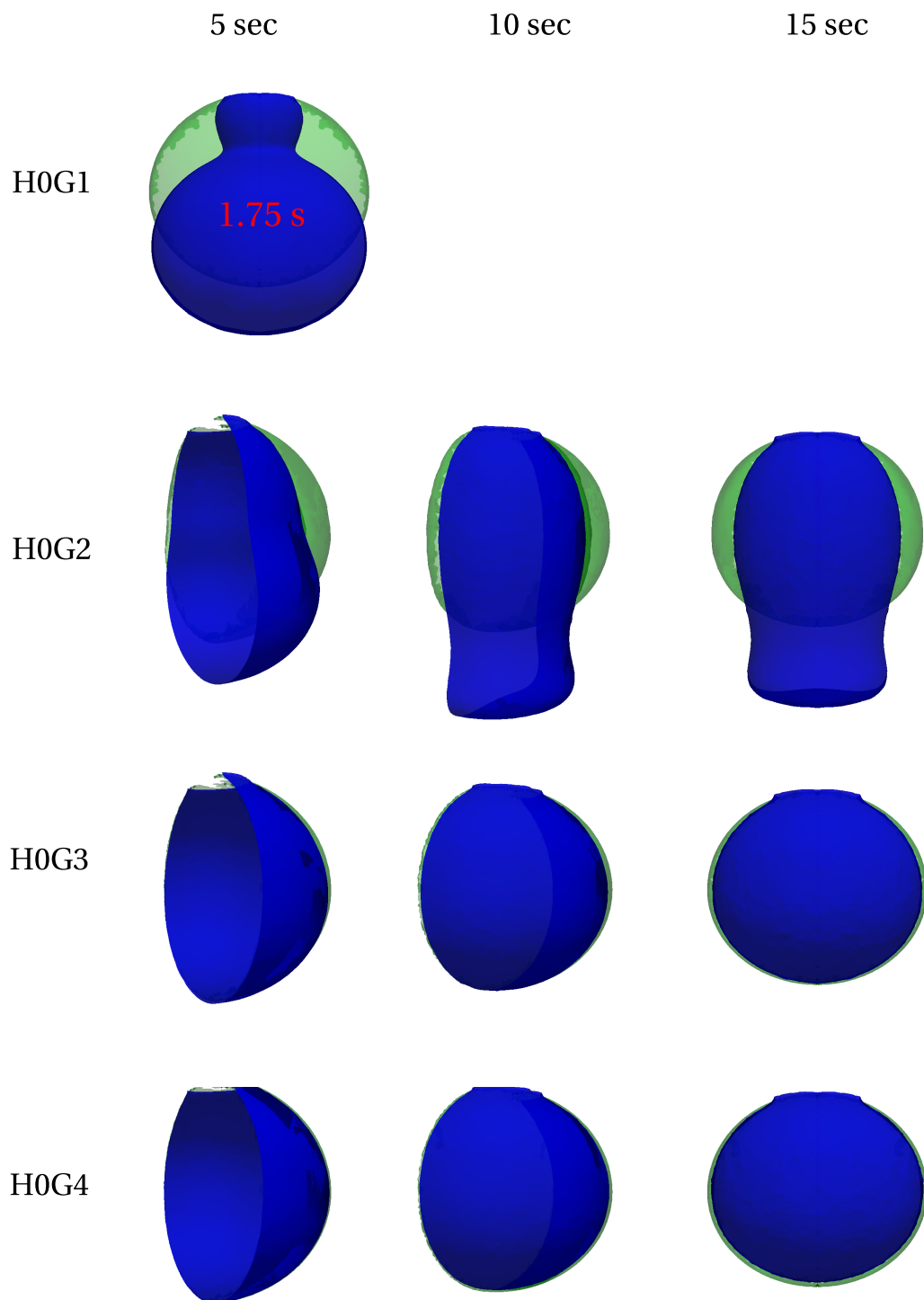


**Fig. 5.34** – 3D snapshots of a droplet (only half shown for symmetry) undergoing solidification shrinkage where the magnitude of the gravitational field decreases from G1 to G4 according to [table 5.7](#). The green surface is the initial droplet profile while the blue surface is the deforming droplet profile. The camera rotation over time allows observing deformation from different angles. The gravity vector points downwards.

## Chapter 5. Macrosegregation with solidification shrinkage

---

**Table 5.8** – Parameters for the 3D simulation of the TEXUS droplet solidification under microgravity conditions.

Parameter	Symbol	Value	Unit
Nominal composition	$w_0$	0.105	wt.%
Liquid density	$\langle \rho \rangle^l$	2600	$\text{kg m}^{-3}$
Solid density	$\langle \rho \rangle^s$	2800	$\text{kg m}^{-3}$
Air density	$\langle \rho \rangle^a$	1.3	$\text{kg m}^{-3}$
Liquid viscosity	$\mu^l$	$10^{-3}$	$\text{Pa s}$
Solid viscosity	$\mu^s$	(Darcy)	$\text{Pa s}$
Air viscosity	$\mu^a$	$10^{-4}$	$\text{Pa s}$
Air thermal conductivity	$\kappa^a$	0.01	$\text{W m}^{-1} \text{K}^{-1}$
Liquid thermal conductivity	$\kappa^l$	42	$\text{W m}^{-1} \text{K}^{-1}$
Solid thermal conductivity	$\kappa^s$	42	$\text{W m}^{-1} \text{K}^{-1}$
Solute diffusion in the liquid	$\langle D \rangle^l$	$1 \times 10^{-9}$	$\text{m}^2 \text{s}^{-1}$
Solute diffusion in the solid	$\langle D \rangle^s$	0	$\text{m}^2 \text{s}^{-1}$
Solute diffusion in the air (fictitious)	$\langle D \rangle^a$	(varies with case)	$\text{m}^2 \text{s}^{-1}$
Gravity acceleration	$h_{\text{ext}}$	$6 \times 10^4$	$\text{W m}^{-2} \text{K}^{-1}$
Heat transfer coefficient	$h_{\text{ext}}$	$6 \times 10^4$	$\text{W m}^{-2} \text{K}^{-1}$
External temperature	$T_{\text{ext}}$	25	$^{\circ}\text{C}$
Initial temperature	$T_0$	800	$^{\circ}\text{C}$
FE mesh size		$10^{-3}$	m
Time step	$\Delta t$	0.01	s
Convergence criterion (residual)	$\varepsilon_R$	$10^{-4}$	—
Convergence criterion (temperature)	$\varepsilon_T$	$10^{-1}$	K

$1^{\circ}\text{C}$  varying in the interval  $[20^{\circ}\text{C}; 1600^{\circ}\text{C}]$ . The importance of choosing small steps in composition and temperature is to predict accurate solidification paths during macrosegregation (relative to the droplet scale), which is the main input of solidification shrinkage. Therefore, less accurate mappings may result in false shrinkage profile prediction, as will be shown henceforth.

Using the initial and boundary conditions defined earlier, 15 seconds of simulation give the final shrinkage profile given in [fig. 5.35](#). We notice that the predicted overall deformation of the droplet is in a good agreement with the experimental shape after solidification. This agreement is still not perfect as some key input parameters are still missing in the model, namely the real gravity acceleration on-board the parabolic flight (which should be much greater than value used in the simulation), and the

correct heat flux between the sample and the substrate. It is emphasized that for higher gravity accelerations, surface tension is of central importance since it counters the gravitational force by stabilising the *M-A* boundary.

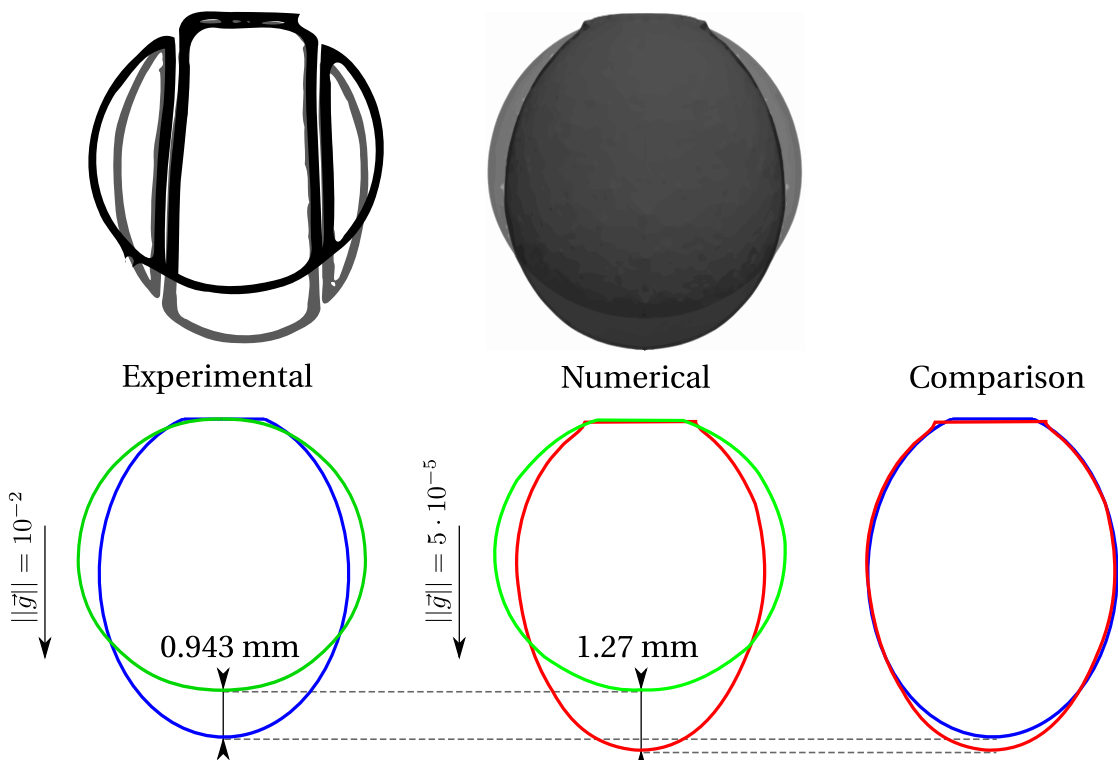


**Fig. 5.35** – Comparison of experimental (blue) and numerical (red) shrinkage profiles, compared to their respective initial shapes (green). A vector image processing algorithm is used to extract the droplet outlines from the experimental images. The experimental displacement at the top of the droplet was estimated by scaling the initial numerical profile to the experimental one, and then comparing the final profiles. The direction of the gravitational fields points downwards, depicted by the arrow (note that the vector length is not scaled to its magnitude).

Three solid phases are considered for the *b1Bin* alloy: a primary BCC phase, a peritectic FCC phase and a cementite phase. The latter can be obtained by cooling the sample at low temperatures to achieve solid-state transformation. The next point to discuss is segregation and fluid flow. With the chosen gravity acceleration, the liquid metal moves in the downward direction when the ceramic substrate comes from above the droplet. As soon as solidification takes place right after the metal-substrate contact, a BCC-rich mushy zone forms near the contact surface. The abrupt phase change imposes a fast shrinkage rate, which tends to straighten the interface near the substrate, as we can observe in [fig. 5.35](#). A part of the flow thus deviates towards the solid front to compensate for the density increase, as shown in [fig. 5.36](#). This flow pattern in the sample shows distinct regions shown at 0.25 s and 1 s in the previous figure: upward

flow driven by solidification shrinkage contributes to a slight enrichment by inverse segregation, while a downward flow driven by gravity redistributes species in the containerless melt. Upon completely solidifying, the droplet forms a rigid and fixed solid, surrounded by natural argon flow.

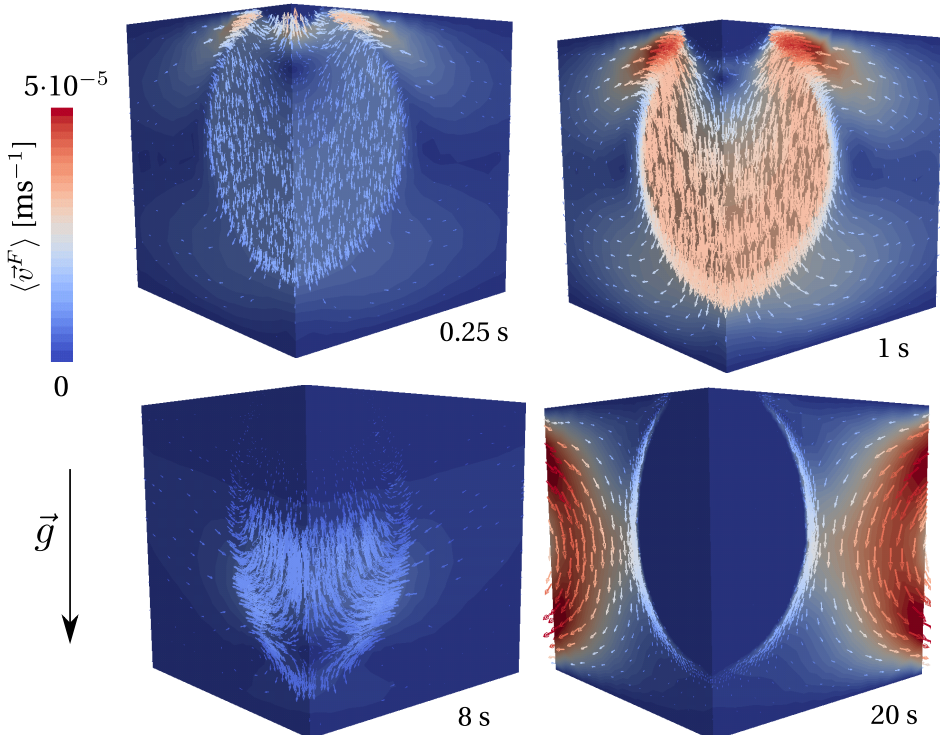


**Fig. 5.36** – Flow patterns in reduced-gravity solidification with shrinkage: deviation towards the solidification front at 0.25 s and 1 s, contributing to solute transport in gravity's opposite direction. At 8 sec, the mushy zone reaches the droplet vertex marking a flow pattern change. At 20 s, the argon flows freely in the domain around the completely solidified and rigid sample. Please note that the scale of latter snapshot has a maximum magnitude of  $10^{-6} \text{ m s}^{-1}$ , not shown for illustrative simplicity.

The fluid flow is behind the reduced-gravity segregation shown at different stages in [fig. 5.37](#). As earlier mentioned, a restricted region of positive segregation settles at the contact area with the substrate, from the first second after the contact. Later, between 2 s and 8 s, the solid front advances in the melt, creating a noticeable negatively segregated area, about 4% less than the nominal composition, just below the positive segregation zone. Normally, we would expect that the composition decreases gradually once the solid front advances in time, as confirm the 1D segregation profiles in [fig. 5.17](#). To interpret this unusual observation, we refer to the fluid flow shown earlier in [fig. 5.36](#). At 0.25 s, a velocity zero-level isovolume (i.e. depicting a volume with null velocity magnitude) forms between the two distinct regions of upward and downward flow. The strong negative divergence that settles in this area results in solute depletion

in the two directions and due to the various driving forces.

However, at 1 s, the zero isovolume clearly shrinks in a matter of only 0.75 s. That is because the initial temperature gradient is the highest during the process, then it decreases gradually. Since a higher temperature gradient produces a greater cooling flux according to the Fourier model, solidification is faster in the beginning and the volume shrinkage is fast, hence the shrinkage flow coexists with the gravity flow. As the transformation progresses, shrinkage flow becomes insignificant compared to the latter, therefore the negative segregation intensity decreases gradually from 2.2 mm to 4.3 mm from the chill, corresponding to the first seconds of contact ( $t < 8$  s). This result is also shown in [fig. 5.39](#) where we plot the relative segregation profile along the vertical rotation axis of the droplet. At 8 s, [fig. 5.36](#) shows the zero-velocity isovolume moved down the vertical revolution axis by following the solidification front, then vanishing at about 10 s. It means that from this point in time, the flow is so dissipated by the mushy zone's low permeability, hence the low-magnitude shrinkage flow dominates again. We may correlate this flow pattern once again to the segregation profile in [fig. 5.39](#): As of 4.3 mm and down to the tip of the deformed sample, we observe a steady rise in solute content caused by the shrinkage-dominated flow between dendrites compensating for density differences. This rise in solute content is however not strictly correct, says the species mass conservation study, shown in FIG.

In [fig. 5.39](#), the final phase distribution along the vertical revolution axis is plotted. The plots show that in the upper part of the droplet close to the chill, a eutectoid product (we may not speak of eutectoid microstructure as the current approach is only macroscopic, without information on the smaller scale) that results from the hypoeutectoid composition, consisting of 98% of  $\alpha$ -BCC phase together and 2% of CEM between 0 and 2.9 mm away from the substrate. Beyond this point, the austenitic  $\gamma$ -FCC phase is gradually replaced by  $\alpha$ -BCC, which represents the proeutectoid  $\alpha$  phase, taking place before temperature reaches the eutectoid isotherm at 727 °C.

A better global visualisation of the transformation is given in [fig. 5.38](#), at different time stages. Each column depicts a definite time with temperature and phase distribution.

### 5.8.4 Texus ternary and quaternary alloys

In this section, the aim is to predict macrosegregation in reduced-gravity solidification of the *b1* alloy, the latter being considered as a ternary and then as a quaternary alloy (cf. [table 5.6](#)). We want to show that, on the one hand our model handles multicomponent alloys (based on equilibrium conditions), while on the other hand, how transformation paths vary by adding additional components, thus changing the shrinkage kinetics, hence the final sample shape. The first visible sign of different paths during

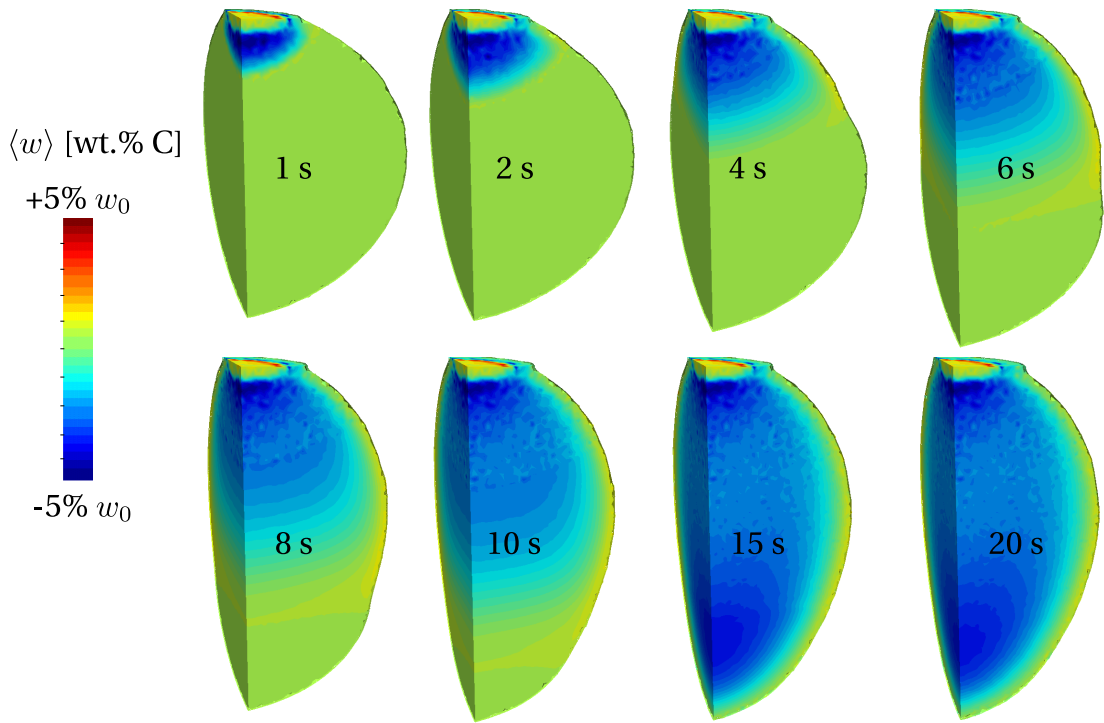


**Fig. 5.37** – Evolution of the average composition with solidification time, showing evidence of segregation and shape deformation between 0 s and 20 s. (check animation in the PDF file).

solidification is given in [fig. 5.40](#). We can see that upon adding additional chemical species while applying the same cooling conditions, a different liquid fraction remains after 15 s, showing evidence of slower solidification as we go from binary to quaternary. Also, with multicomponent alloys like *b1Tern* and *b1Quat*, an additional solid phase may appear, that is the  $M_7C_3$  carbide. Slower cooling rates result in more elongated droplet shapes due to weight force, whereas shrinkage forces tend to counter this effect. Therefore the final predicted shape is different, as shown earlier in the parametric study.

In [fig. 5.41](#), we focus on the final droplet profile caused by varying the number of solute elements. We clearly notice that the multicomponent solidification results in a slightly more elongated shape. All cases were obtained using the optimal simulation parameters determined previously by the parametric study, i.e. thermal exchange coefficient,  $h_{ext}$ , of  $6 \times 10^4 \text{ W m}^{-2} \text{ K}^{-1}$  and a gravitational acceleration,  $\|g\|$ , of  $5 \times 10^{-5} \text{ m s}^{-2}$ . The clear difference in solidification paths requires to do the same parametric study to get better simulation-vs-experiment prediction. However, as we have shown earlier the effect of varying these parameters on the final profile, we do not perform parametric studies for *b1Tern* and *b1Quat* alloys.

The vertical elongation obtained by the *b1Tern* sample is almost the double of the

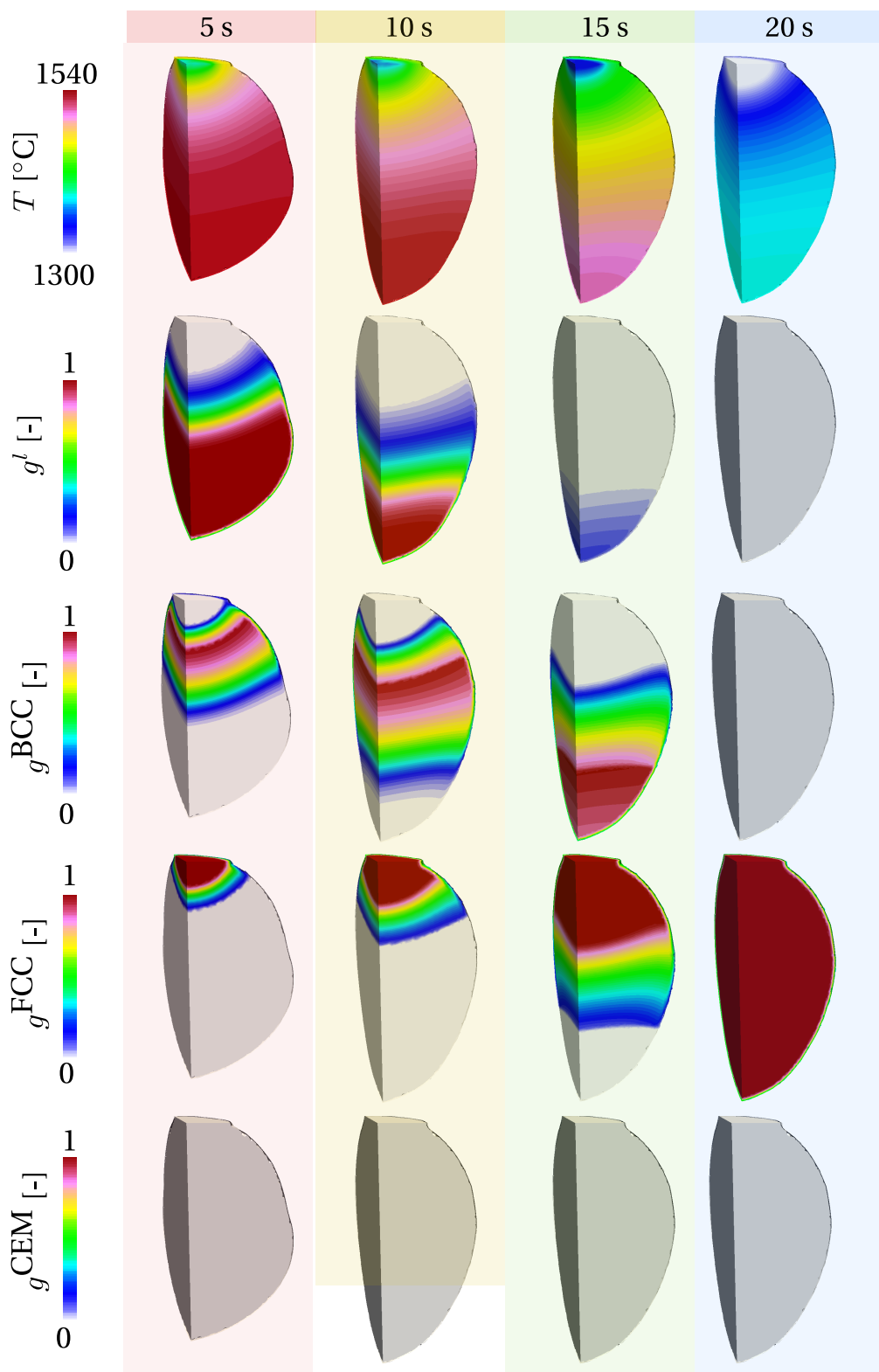


**Fig. 5.38** – Solidification progress at 5, 10, 15 and 20 s showing the effect of segregation on the transformation paths, from liquid to solid and solid-state.

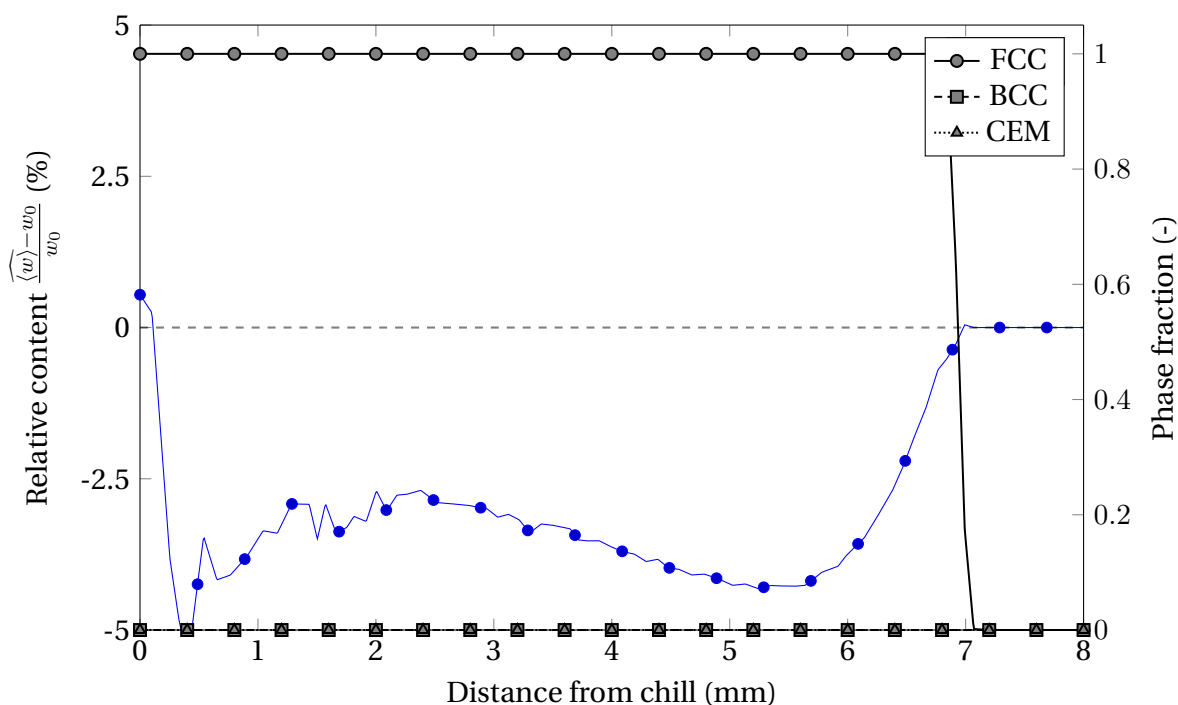


**Fig. 5.39** – Relative segregation profile in percent with respect to the nominal composition, along the vertical revolution axis of the solidified sample at a temperature lower than 1100 °C. Phase fractions are superimposed on the same graph and their values are read on the right y-axis.

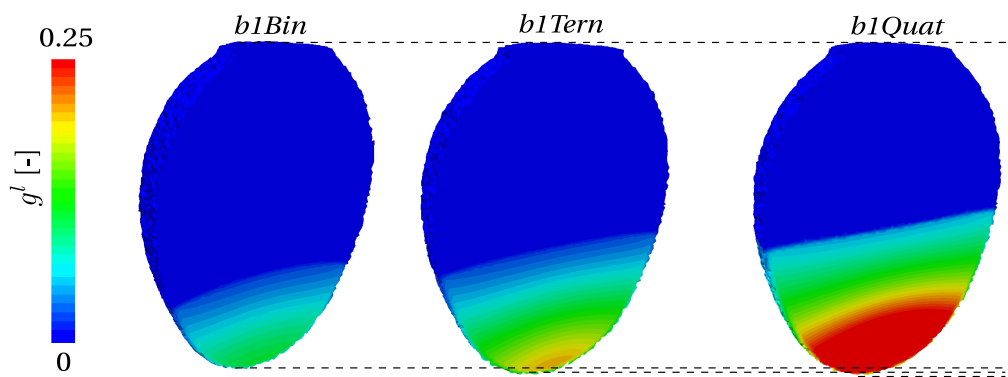


**Fig. 5.40** – Snapshots showing the remaining volume fraction of liquid at 15 s in each sample of the binary, ternary and quaternary *b1* alloy.

*b1Bin* result. Moreover, the final ternary and quaternary profiles are almost overlapping, indicating that the prediction accuracy is very close for these alloys. This reveals the importance of simulating solidification processes with real alloy compositions instead of binary simplifications where the transformation path is not complex as a result of the smaller number of phases forming at equilibrium.

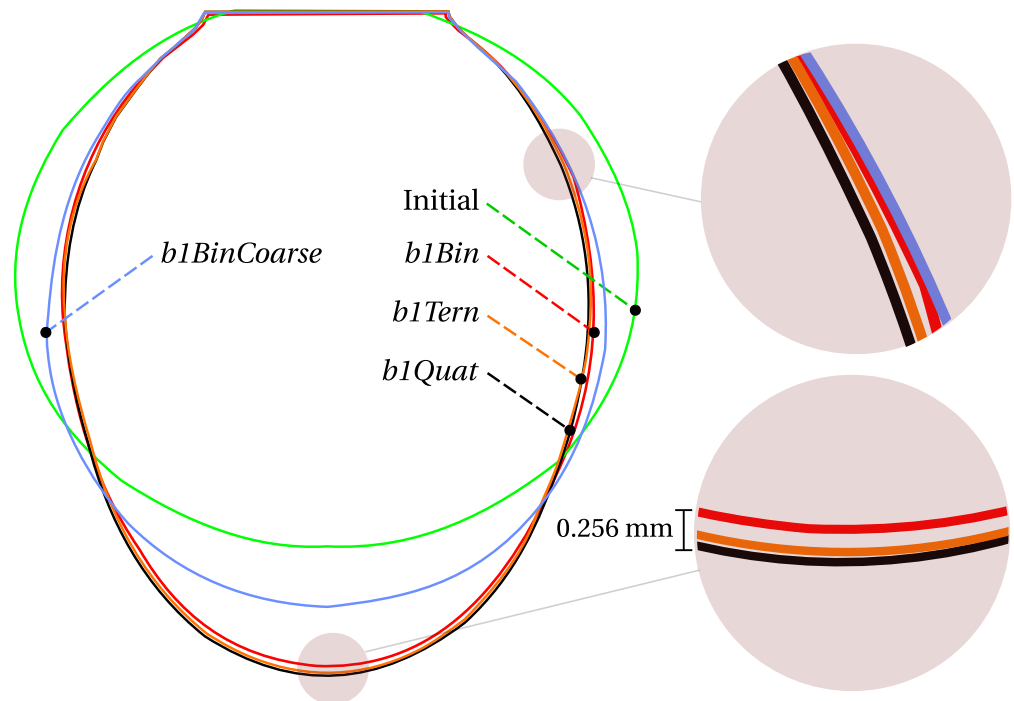


**Fig. 5.41** – Comparison of final droplet profiles obtained by solidifying *b1Bin*, *b1Tern* and *b1Quat* samples, with respect to the initial profile. The *b1BinCoarse* sample is obtained using coarser composition steps.

Nevertheless, it should be mentioned that the mapping resolution plays an important role in the accuracy of thermodynamic conversions. Therefore, tabulations size easily increases with the increasing number of solute elements, because of the greater number of temperature-composition combinations to scan while computing equilibrium. To test the effect of changing the mapping resolution, we repeated the binary sample solidification but with a composition step of 0.0495 wt.% instead of 0.0052 wt.% used for the *b1Bin* sample, i.e. about 10 times coarser. The corresponding profile in fig. 5.41, *b1BinCoarse*, shows less vertical elongation than predicted by the finer *b1Bin* tabulation. This is clearly due to inaccurate calculation of the solidification path, revealing the importance of mappings accuracy in predicting transformation-related physics. In order to test the effect of the tabulation file size on computation time, we simulate again the quaternary solidification case but this time with a lightweight tabulation where all successive line with similar phase fractions outside the solidification range

## Chapter 5. Macrosegregation with solidification shrinkage

---

are deleted, giving what we call *b1QuatLite*. The resulting file is three time smaller than the original tabulation file. Surprisingly, the computation time for *b1QuatLite* shows no significant acceleration compared to *b1Quat*. The file size, proportional to the number of tabulated lines, is important as it causes a search overhead each time the conversion module is called. However, [table 5.9](#) reveals that the multi-variable interpolation overhead is even more important, resulting in longer computation times. This may be considered as a limitation of the thermodynamic mapping approach.

**Table 5.9** – Information table showing the tabulations size for each alloy obtained by the same mapping resolution for temperature and composition, depending on the number of solute elements and phases. The temperature step is 1 °C and the range is the range is [20-1620]°C for all four cases . The computation time corresponds to the CPU time of a simulation running on 20 cores.

Alloy	Nb solutes	Composition range (wt.%)	Composition step (wt.%)	Nb phases	Tabulation lines	Size (MB)	Computation time (s)
<i>b1Bin</i>	1	C: [0.0945-0.1155]	0.00525	4	185 010	4.37	59 461.5
<i>b1Tern</i>	2	C: [0.0945-0.1155] Si: [0.2412-0.2948]	0.00525 0.0134	5	220 250	10.18	62 644.4
<i>b1Quat</i>	3	C: [0.0945-0.1155] Mn: [0.5724-0.6996] Si: [0.2412-0.2948]	0.00525 0.0318 0.0134	5	1 101 250	66.89	85 476.7
<i>b1QuatLite</i>	3	C: [0.0945-0.1155] Mn: [0.5724-0.6996] Si: [0.2412-0.2948]	0.00525 0.0318 0.0134	5	326 014	20.93	84 104.8

Finally we are interested in comparing the macrosegregation levels obtained in all three solidification cases. Segregation maps are presented in [fig. 5.42](#) on a symmetry plane section. First, we compare the carbon segregation as it is the common species among the presented alloys. The first difference is a remarkable positive macrosegregation of 3.5% at the chill contact of the *b1Tern* and *b1Quat* samples, while being less prominent for *b1Bin* which shows a relative segregation of 1.2%. As we explained earlier, this positive macrosegregation taking place at the beginning of solidification is related to the shrinkage flow (cf. [fig. 5.36](#)) created by the strong thermal gradient in the contact zone. As the thermal gradient in this zone is almost the same for all three cases at solidification onset, the higher velocity which is responsible for the noticeable positive macrosegregation in both multicomponent samples, is related to the solidification path varying with the number of species. Two regions of negative macrosegregation are observed across the samples, with various amplitudes. The first region lies just below the positive segregation contact surface. It corresponds to the solute depletion caused by an upward shrinkage flow and a downward gravity flow. With the advancement of the solidification front, the gravity flow dominates creating a radial outward negative segregation pattern where

## 5.8. 3D application: reduced-gravity solidification

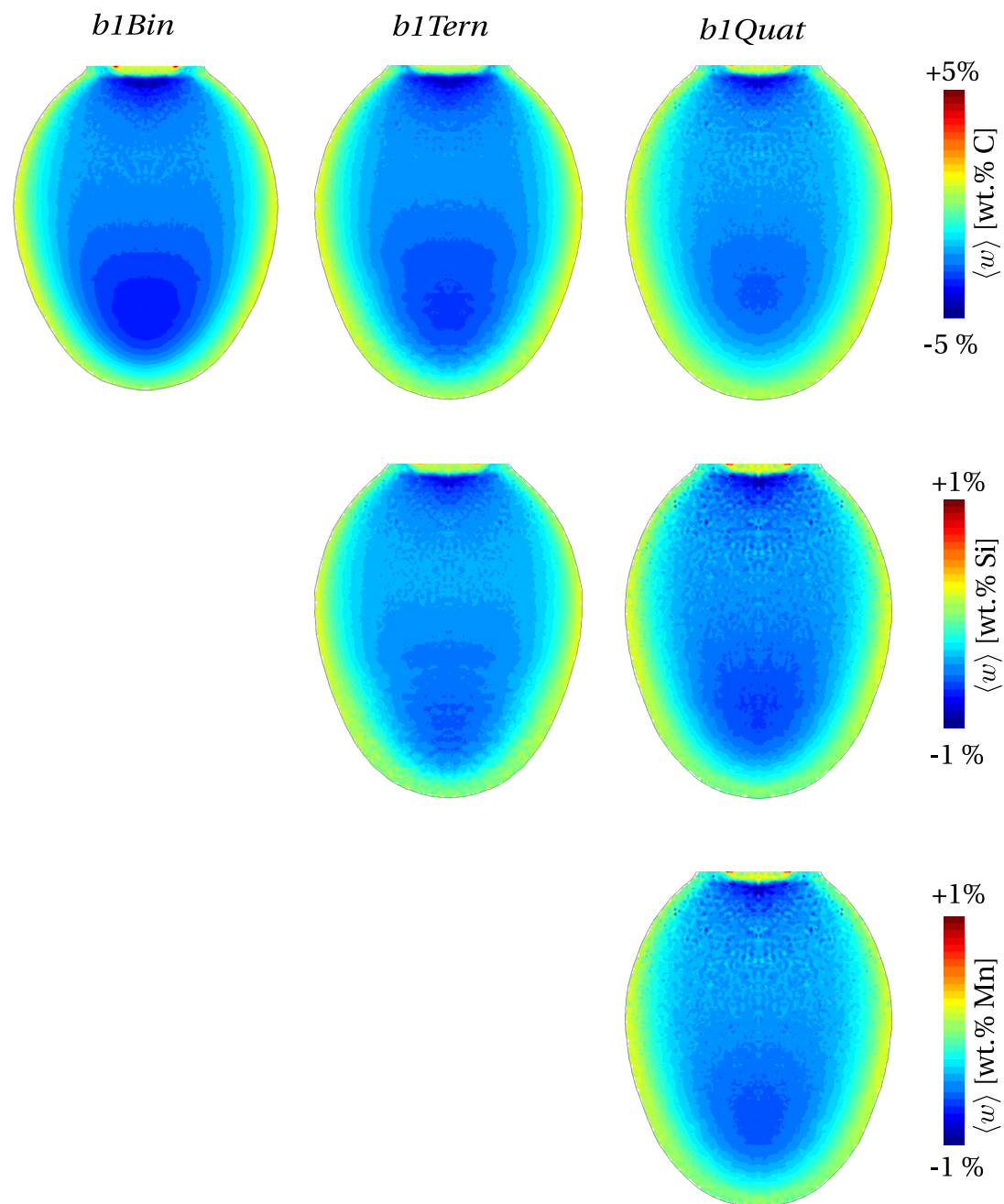


**Fig. 5.42** – Segregation maps relative to each alloy, showing positive and negative mesosegregations of each chemical species for *b1Bin*, *b1Tern* and *b1Quat* samples.

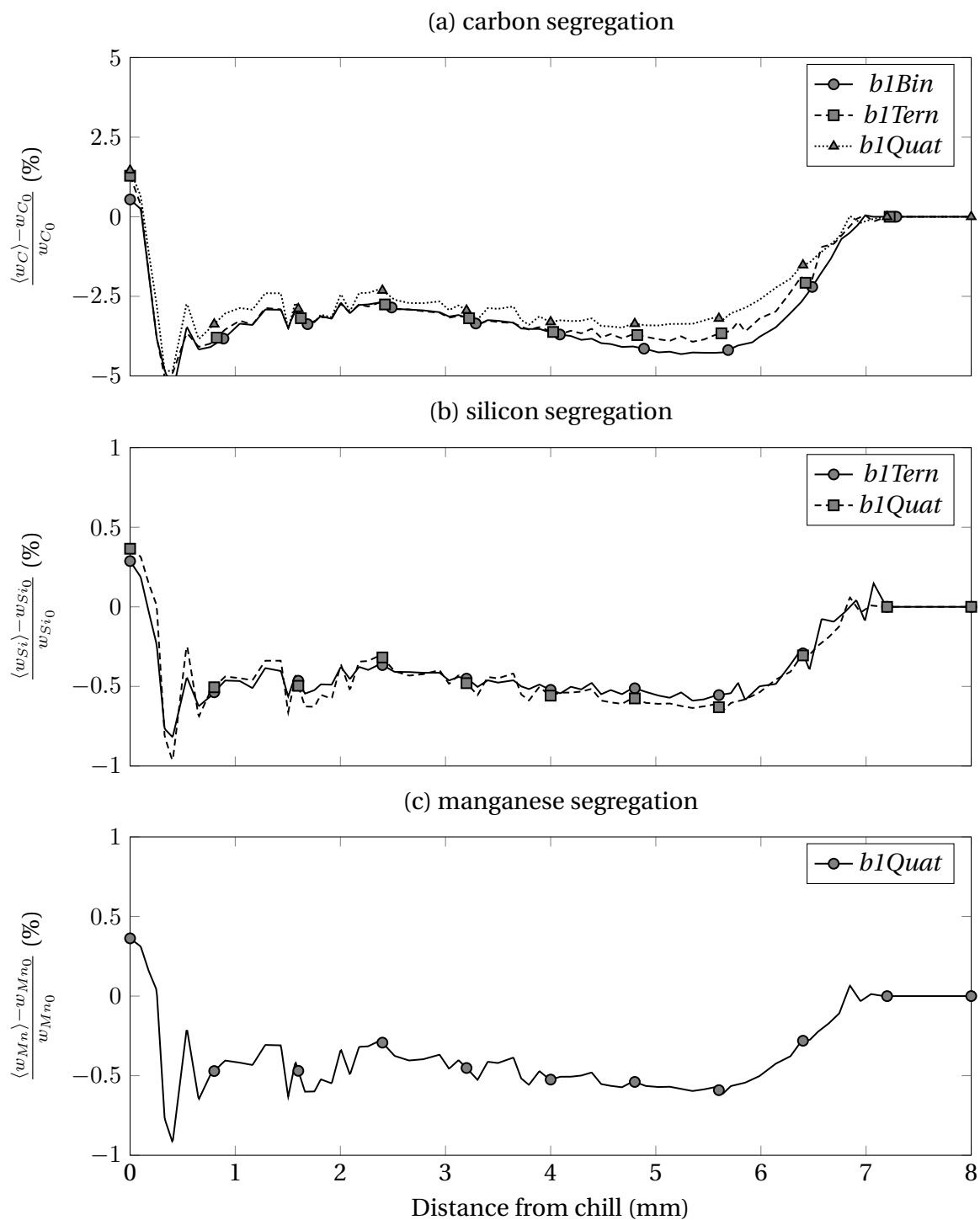


**Fig. 5.43** – Relative macrosegregation profiles as functions of the distance from the chill, plotted for (a) carbon (b) silicon and (c) manganese elements along the vertical revolution axis of the solidified sample.

### Résumé chapitre 5

Ce dernier chapitre est dédié à la prise en compte du retrait à la solidification à l'origine de la déformation de la surface libre métal-air, en présence des phénomènes de ségrégation. Pour ce faire, le modèle de solidification utilisé précédemment pour prédire la macroségrégation induite par convection thermosolutale en monodomaine, est enrichi par une méthode de suivi direct d'interface, la level set. Les équations du modèle sont alors reformulées dans un contexte eulérien multidomaine-multiphasé, i.e. où deux domaines multiphases sont séparés par une interface mobile, l'aspect multiphase dans chaque domaine étant géré par la méthode de prise de moyenne volumique.

Un premier cas d'application 1D est ensuite présenté. C'est un cas qui avait fait l'objet de validation du *Tsolver* dans le chapitre 3, et qui est refait avec des masses volumiques solide et liquide différentes. Cette application simple permet toutefois de comprendre le phénomène de ségrégation inverse résultant de l'écoulement du liquide vers le front de solidification pour compenser la différence des masses volumiques des phases, ce qui enrichit en solutés la partie du métal en contact avec le refroidisseur. Ce phénomène est souvent observé en surfaces des lingots en contact avec les moules. Des courbes de refroidissement ainsi qu'un bilan de conservation de masse de métal sont présentés pour permettre de comprendre l'effet de l'introduction de la méthode level set sur la physique de la solidification.

La seconde application est aussi un cas de validation utilisé dans un chapitre précédent, issu d'une simulation sans retrait présente dans la littérature [CAROZZANI et al. 2013]. Cependant, le but en est maintenant de tester la robustesse du modèle en présence de convection naturelle, d'origine thermique dans l'air et thermosolutale dans le métal, avec suivi de déformation de l'interface par retrait à la solidification. Nous utilisons une méthode de remaillage adaptatif basée sur la projection sur les arêtes [COUPEZ et HACHEM 2013], permettant d'avoir une résolution de maillage fine autour des zones d'intérêt, notamment l'interface décrite par level set, le vecteur vitesse et la concentration moyenne. Ce couplage de techniques numériques permet de déterminer à la fois la retassure en surface du lingot et la macroségrégation, présente également sous forme de canaux.

Dans le dernier cas, il s'agit de la solidification d'une goutte d'acier en microgravité. Des essais expérimentaux de solidification déclenchée par contact avec un substrat sont présentés avec la forme finale de la goutte. Pour pouvoir prédire la déformation de la goutte en présence de ségrégations, nous considérons trois nuances issues du même alliage : un binaire (*b1Bin*) Fe-C, un ternaire (*b1Tern*) Fe-C-Si et finalement un quaternaire (*b1Quat*) Fe-C-Mn-Si. D'abord, une étude paramétrique est faite en se servant de l'alliage binaire, dans le but de déterminer les paramètres optimaux de vitesse de refroidissement et d'accélération gravitationnelle, pour se rapprocher du profil expérimental de la goutte déformée en fin de solidification. Ensuite, nous simulons la solidification de chaque alliage en montrant la déformation finale ainsi que la distribution finale des espèces chimiques.



# **Conclusion and Perspectives**

## **Conclusions**

The summary of what we did in the previous chapters

## **Future Work**

What did we miss in our models that can be potentially important for the coming years



# Bibliography

## [Basset 2006]

Basset, O. (2006). "Simulation numérique d'écoulements multi-fluides sur grille de calcul". PhD Thesis. École Nationale Supérieure des Mines de Paris. URL: <https://tel.archives-ouvertes.fr/tel-00376484> (cited on page 171).

## [Carozzani et al. 2013]

Carozzani, T., Gandin, C.-A., Digonnet, H., Bellet, M., Zaidat, K., and Fautrelle, Y. (2013). "Direct Simulation of a Solidification Benchmark Experiment". *Metallurgical and Materials Transactions A*, 44 (2), pp. 873–887. URL: <http://link.springer.com/article/10.1007/s11661-012-1465-1> (cited on page 189).

## [Chen 2014]

Chen, S. (2014). "Three dimensional Cellular Automaton - Finite Element (CAFE) modeling for the grain structures development in Gas Tungsten / Metal Arc Welding processes". PhD thesis. Ecole Nationale Supérieure des Mines de Paris. URL: <https://pastel.archives-ouvertes.fr/pastel-01038028/document> (cited on page 135).

## [Coupez and Hachem 2013]

Coupez, T. and Hachem, E. (2013). "Solution of high-Reynolds incompressible flow with stabilized finite element and adaptive anisotropic meshing". *Computer Methods in Applied Mechanics and Engineering*, 267, pp. 65–85. URL: <http://www.sciencedirect.com/science/article/pii/S0045782513002077> (cited on page 189).

## [Dantzig and Rappaz 2009]

Dantzig, J. A. and Rappaz, M. (2009). *Solidification*. EPFL Press (cited on page 124).

## [Flemings and Nereo 1967]

Flemings, M. C. and Nereo, G. E. (1967). "Macrosegregation: Part I". *Transactions of the Metallurgical Society of AIME*, 239, pp. 1449–1461 (cited on page 137).

## [Gandin 2014]

Gandin, C.-A. (2014). *Project ESA-MAP CCEMLCC phase #2 – Final Report* (cited on pages 165, 170).

## [Hachani et al. 2012]

Hachani, L., Saadi, B., Wang, X. D., Nouri, A., Zaidat, K., Belgacem-Bouzida, A., Ayouni-Derouiche, L., Raimondi, G., and Fautrelle, Y. (2012). "Experimental analysis of the solidification of Sn–3 wt.%Pb alloy under natural convection". *International Journal of Heat and Mass Transfer*, 55 (7–8),

## Bibliography

---

pp. 1986–1996. URL: <http://www.sciencedirect.com/science/article/pii/S0017931011007009> (cited on pages 157, 159).

### [Hebditch and Hunt 1974]

Hebditch, D. J. and Hunt, J. D. (1974). “Observations of ingot macrosegregation on model systems”. *Metallurgical Transactions*, 5 (7), pp. 1557–1564. URL: <http://link.springer.com/article/10.1007/BF02646326> (cited on page 157).

### [Niane 2004]

Niane, N. T. (2004). “Étude des macroségrégations induites par le retrait et la déformation thermomécanique lors de la solidification de la peau des produits sidérurgiques”. PhD thesis. URL: <http://www.theses.fr/2004INPL088N> (cited on page 124).

### [Onodera and Arakida 1959]

Onodera, S. and Arakida, Y. (1959). “Effect of Gravity on the Macro-Segregation of Larger Steel Ingots”, pp. 358–368. URL: <http://eprints.nmlindia.org/3079/1/358-368.PDF> (cited on page 120).

### [Rappaz et al. 2003]

Rappaz, M., Bellet, M., and Deville, M. (2003). *Numerical Modeling in Materials Science and Engineering*. Springer Series in Computational Mathematics. Springer Berlin Heidelberg (cited on page 123).

### [Rivaux 2011]

Rivaux, B. (2011). “Simulation 3D éléments finis des macroségrégations en peau induites par déformations thermomécaniques lors de la solidification d’alliages métalliques”. PhD Thesis. École Nationale Supérieure des Mines de Paris. URL: <http://pastel.archives-ouvertes.fr/pastel-00637168> (cited on pages 166, 168, 170).

### [Saad et al. 2015]

Saad, A., Gandin, C.-A., and Bellet, M. (2015). “Temperature-based energy solver coupled with tabulated thermodynamic properties – Application to the prediction of macrosegregation in multicomponent alloys”. *Computational Materials Science*, 99, pp. 221–231. URL: <http://www.sciencedirect.com/science/article/pii/S0927025614008465>.

### [Sethian 1999]

Sethian, J. A. (1999). *Level Set Methods and Fast Marching Methods: Evolving Interfaces in Computational Geometry, Fluid Mechanics, Computer Vision, and Materials Science*. Cambridge University Press (cited on page 121).

### [Voller et al. 1989]

Voller, V. R., Brent, A. D., and Prakash, C. (1989). “The modelling of heat, mass and solute transport in solidification systems”. *International Journal of Heat and Mass Transfer*, 32 (9), pp. 1719–1731. URL: <http://www.sciencedirect.com/science/article/pii/0017931089900549> (cited on page 129).

# Modélisation par Level Set des macroségrégations induites par le retrait à la solidification

**RESUME :** La macroségrégation est un défaut connu dans les procédés de coulées industrielles. La genèse de ce défaut est la conséquence de l'interaction complexe entre la microségrégation ou la distribution des espèces chimiques à l'échelle de la microstructure et les mouvements des phases liquide et solides. Les hétérogénéités de concentration en solutés à l'échelle de la pièce peuvent être rédhibitoires vis-à-vis de la qualité du produit. Dans ce travail, on propose un modèle numérique pour simuler et prédire la formation des macroségrégations en cœur des pièces d'alliages multi-constitués, induites par des variations thermiques et solutales dans la phase liquide. Dans un premier temps, on considère que le métal solidifie à volume constant. Dans ce contexte, la convection thermosolutale est étudiée ainsi que son influence sur la formation des canaux ségrégés à différentes échelles de modélisation. Dans un deuxième temps, le modèle vise à prédire les macroségrégations en présence de changement de volume du métal, dont la cause principale est le retrait à la solidification, pouvant être à l'origine du phénomène de ségrégation inverse. La surface entre le métal et le gaz environnant au cours du retrait évolue pendant le retrait en fonction du chemin de solidification qui varie avec la macroségrégation. Cette évolution d'interface est suivie par la méthode Level set. Des prédictions de concentration moyenne, couplées aux bases de données thermodynamiques pour mieux prédire les chemins de solidification des alliages multi-constitués, sont analysées et comparées avec des résultats expérimentaux. Finalement, des calculs de solidification en microgravité sont présentées, simulant un essai expérimental dans le contexte du projet CCEMLCC lancé par l'Agence Spatiale Européenne. Les résultats en fin de solidification montrent un accord acceptable quant à la forme et l'elongation des échantillons solidifiés. Ces calculs sont faits avec des approximations binaire, ternaire et quaternaire d'une même nuance d'acier utilisée dans les essais en microgravité.

**Mots clés :** modélisation, solidification, ségrégation, Level Set, éléments finis, métallurgie

## Numerical modeling of macrosegregation formed during solidification with shrinkage using a Level Set Approach

**ABSTRACT :** Macrosegregation is key defect in industrial casting processes. During solidification, solute redistribution at the scale of microstructure, also known as microsegregation, take place with complex interactions, in order to form one or more solid phases. These interactions between microsegregation and movements of liquid and solid phases may lead to macrosegregations. These solute heterogeneities spanning on a larger scale, may result in a bad casting quality. In this thesis, we propose a numerical model to simulate and predict macrosegregations occurring in the centre of multicomponent alloys, caused by thermal and solutal variations in the liquid phase. First, we assume that the metallic alloy solidifies with a constant volume. In this context, we study the influence of thermosolutal convection on the formation of channel segregations, at different modelling scales. The second part of this modelling work consider solidification while the metallic alloy's volume is decreasing, mainly due to overall density variation, also known as solidification shrinkage, possibly leading to the so-called inverse segregation phenomenon, appearing on the alloy's skin. In the context of solidification shrinkage, the shape of the metal's boundary with surrounding gases varies according to a constantly changing solidification path due to macrosegregation. The Level Set method is therefore used to track its evolution with time. Composition predictions, coupled with thermodynamic database mappings for more accurate multicomponent solidification paths, are analysed and compared to existing experimental setups. Finally, simulations of a reduced-gravity solidification cases are performed, mocking an experimental benchmark from the CCEMLCC project launched by the European Space Agency. The results show acceptable agreement for the final shape, compared to experimental results. These computations were performed with binary, ternary and quaternary approximations of the same steel grade which was used in reduced-gravity experiments.

**Keywords :** modélisation, solidification, segregation, Level Set, finite elements, metallurgy

